

Magnetotunneling through a quantum well in a tilted field I: Periodic orbit theory

E. E. Narimanov and A. Douglas Stone

Applied Physics, Yale University, P.O. Box 208284, New Haven CT06520-8284

(Preprint: February 1, 2008)

A semiclassical theory is developed and compared to experiments on the tunneling resonance spectrum for a quantum well in magnetic field tilted by an angle θ with respect to the tunneling direction. As the tilt angle is increased from zero the classical mechanics of an electron trapped within the well undergoes a smooth transition from integrable to chaotic dynamics. Perturbation theory is invalid for most of the regime of experimental interest, motivating a semiclassical treatment based on short periodic orbits within the well. In this paper we present a unified theory of all the periodic orbits within the well which are of relevance to experiments and show that they are all related to bifurcations of the period-one traversing orbits. An analytic theory is derived for the period and stability of these traversing orbits. An unusual feature of the classical mechanics of this system is the existence of certain important periodic orbits only in finite energy bands. We calculate the widths of these bands and relate them to experimental data. In the following paper the results for these short periodic orbits are used in conjunction with a novel semiclassical tunneling formula to calculate the magnetotunneling current, which is then compared with experiments.

PACS numbers: 05.45.+b, 72.15.Gd, 73.20.Dx

I. INTRODUCTION

Most of our intuition about the properties of quantum systems comes from the consideration of hamiltonians with high symmetry, for which the classical motion is integrable and hence the Schrödinger equation is separable. Symmetry-breaking terms are typically treated by perturbation theory and the physics is described in terms of transitions induced between stationary states of the symmetric problem. This approach fails when the symmetry-breaking terms become too large and many levels of the unperturbed system are strongly mixed. In this situation one approach is direct numerical solution of the non-separable Schrödinger equation using a large basis set and calculation of the expectation values of interest from the numerically-determined eigenstates. For most problems of interest the computational effort involved is substantial, particularly if one wishes to explore a large parameter space of hamiltonians and not just a single fixed set of parameters. Moreover, an exclusively numerical approach makes it very difficult to understand qualitatively the dependence of physical properties on the parameters of the problem and thus to generalize the results to other related systems.

An alternative approach which can give greater physical insight is to use the semiclassical methods developed for non-integrable systems during the past two decades by researchers studying “quantum chaos”, i.e. the quantum manifestations of chaotic classical dynamics. This approach has been used successfully in atomic physics during the past decade. Of particular note is the theory of the spectra of Rydberg states in a high magnetic field (diamagnetic Kepler problem),^{1,2} where a qualitative *and* quantitative understanding has been obtained semiclassically in excellent agreement with experiments. In that case the essential idea behind the theory is a relationship between the quantum density of states (DOS) and a sum over isolated unstable periodic classical orbits first derived by Gutzwiller (the “Gutzwiller Trace Formula”)³. However this formula had to be extended to account for experimental spectra which depend on other factors in addition to the density of states⁴.

Until recently there were no comparable applications of semi-classical theory to condensed matter systems. Within the past few years however several such systems have been identified: ballistic microcavities^{5,6}, two-dimensional antidot arrays^{7,8}, and the system which is the subject of this paper, resonant tunneling diodes (RTD) in a magnetic field tilted by an angle θ with respect to the tunneling direction. It has become clear that of the three, this system allows the most detailed comparison between theory and experiment, because the microscopic hamiltonian is known so accurately and because several continuous experimental control parameters may be tuned *in situ* to map out a large parameter space.

This system was first identified and studied by Fromhold et al.⁹, who immediately understood the close analogy to the Garton-Tomkins¹ spectral oscillations in the diamagnetic Kepler problem. When the tilt angle θ is zero the experiment corresponds to a conventional resonant magnetotunneling geometry; there is resonant structure in the I-V characteristic (causing peaks in d^2I/dV^2) with each peak corresponding to the sub-band thresholds in the quantum well. The experiments were done at fixed magnetic field $B = 11\text{T}$, for which the emitter state of the resonant tunneling

device is primarily the $n = 0$ Landau level, so that the observed peaks were only due to quantum well states with sub-band quantum number p and Landau index $n = 0$, as selection rules prohibit tunneling to other Landau levels. Typically of order twenty such resonance peaks (sub-bands) were observed over the interval zero to one volt. However, when the magnetic field was tilted by a substantial amount ($\theta > 20^\circ$), Fromhold et al.⁹ found that in certain voltage intervals the number of tunneling resonances would abruptly increase indicating the presence of tunneling processes which could not be explained by the sub-band structure of the well at $\theta = 0$. They interpreted these new peaks in terms of density of states oscillations associated semiclassically with the short periodic orbits of the well which collide with both the emitter and collector barriers. Numerical integration of the classical equations of motion revealed a number of relevant periodic orbits (we will discuss the different orbit types in detail below), and that in most of the voltage range at $B = 11\text{T}$ these orbits were unstable fixed points in an almost completely chaotic phase space. It was found that the spacing of the new resonances in voltage were consistent with the period of the orbits identified, as was their appearance at particular values of the magnetic field. In more recent work those authors¹⁰ have emphasized that in many cases these oscillations should be interpreted as arising from individual electron eigenstates in the well which concentrate on the relevant classical periodic orbit (the “scarred” wavefunctions), and not by the level-clustering normally associated with the DOS oscillations given by Gutzwiller’s trace formula. All of this work was done at high magnetic field and large tilt angles such that the classical dynamics is almost completely chaotic.

Another important series of experiments¹¹ looked at the I-V peaks in the entire (plane) parameter space of magnetic field and voltage, varying the tilt from $\theta = 0$ to $\theta = 45^\circ$ in small increments so that the resonance structure could be carefully analyzed in the transition regime between chaos and integrability. They found a complicated pattern of peak-doubling and peak-tripling in various regions of the $B - V$ plane, which extended to much lower magnetic field than previously reported. Such experiments are particularly interesting from the theoretical point of view because, as discussed below, classically the system is undergoing a transition to chaos as a function of continuous parameters (θ, B, V). In our view no quantum system of comparable controllability existed previously for the study of the quantum manifestations of the *transition* to chaos with its associated KAM (Kolmogorov-Arnold-Moser) behavior in phase space¹². It is these experiments which we shall analyze in detail in this paper and its companion work¹³. As will be shown in the companion work, the non-linear conductance of the well is related to a weighted local density of states in the well, which takes into account the coupling of well states to the emitter wavefunction. Electrons tunnelling from the emitter into the well at high voltages gain kinetic energy as they accelerate in the field and collide with the collector barrier. Over several collisions in the well the electron loses this energy by optic phonon emission. Therefore the tunneling resonances are substantially broadened and only are sensitive to structure in the DOS on energy scales $> \hbar/T_{\text{opt}} \sim 5\text{meV}$. The semiclassical tunneling theory we will develop in the following paper¹³ relates the tunneling oscillations in the spirit of Gutzwiller’s trace formula³ to a sum of contributions from each periodic orbit (PO) :

$$w_{\text{osc}} = \sum_{\alpha,n} A_{\alpha,n} \exp(-nT_{\alpha}/\tau_{\text{opt}}) \cos\left(\frac{nS_{\alpha}}{\hbar} + \phi_{\alpha}\right) \quad (1)$$

where w_{osc} is the oscillatory part of the tunneling rate from the emitter to the well per unit time, the summation is carried out over various primitive periodic orbits in the well reaching the emitter wall (α) and their repetitions (n). S_{α} is the action of a primitive orbit, the amplitude

$$A_{\alpha,n} = \sum_{m=1}^M a_m^{(\alpha,n)} \quad (2)$$

where the integer M is number of collisions of a particular periodic orbit with the emitter wall. The general expressions for the “coupling coefficients” a_m are quite complicated¹³ and include both the stability properties of the periodic orbits and the velocity distribution of the tunneling electrons (which is related to the Wigner transform of the wavefunction of the *isolated* emitter state).

The broadening of the energy levels in the well due to inevitable emission of optical phonons, which accounts for the $\exp(-nT_{\alpha}/\tau_{\text{opt}})$ in the tunneling formula (1), implies that only the shortest PO’s (period one to four orbits) will give resolvable structure in the experiments we analyze. In this paper we focus on the the classical mechanics of these short periodic orbits relevant to experiment.

Although the work of Fromhold et al. had identified several important periodic orbits in the classical mechanics, they had not provided a model of the global phase-space structure as the system undergoes the transition to chaos. Shepelyansky and Stone¹⁴ developed such a model by reducing the dynamics to a two-dimensional effective map which, in the limit where the emitter state energy is negligible, is equivalent to the Chirikov standard map. This limit amounts to replacing the double-barrier system with a single-barrier model since the injected electron does not have enough energy to climb the potential hill and collide with the emitter barrier. In this limit the dynamics is controlled

by a single chaos parameter $\beta = 2v_0 B/E$ where B, E are the magnetic, electric fields and $\epsilon_0 = m^* v_0^2/2$ is the total injection energy of the electron. Since for much of the experimental parameter range $eV \approx \epsilon_0$, Shepelyansky and Stone argued that the classical mechanics should be approximately constant along parabolas $V = 8ed^2 m^{*-1} \beta^{-2} B^2$ (d is the distance between the barriers) and estimated the value of β at which global chaos occurs using the Chirikov resonance overlap criterion¹⁶. They pointed out that the first appearance of additional resonance peaks at $B \approx 5T, \theta = 11^\circ$ appeared to be due to the bifurcation of the main period-one orbit however they did not analyze these bifurcations further at the time.

In this paper we provide a detailed analysis of the classical mechanics of these bifurcations both within the single-barrier model (SBM) and the more accurate double-barrier model (DBM). The experimental data¹¹ shows that at tilt angles less than 24° the peak-doubling is “re-entrant” as the magnetic field is increased. This effect is related to non-linear resonances between the longitudinal and cyclotron frequencies and is correctly described by the SBM. These resonances lead to bifurcations of the main period-one orbit, which we shall refer to as the “traversing orbit” (TO), since near resonance this orbit is not isolated and new orbits can be born without violating the Poincaré index conservation theorem¹⁵. Therefore it is qualitatively correct, as conjectured by Shepelyansky and Stone¹⁴ and Muller et al.¹¹, to associated peak-doubling and tripling with bifurcations of the traversing orbit. Below we derive an exact analytic expression for the period and stability of the traversing orbit in both the SBM and DBM which allows us to locate precisely the bifurcation points for all values of B, V, θ . The existence of such exact analytic formulas for non-trivial periodic orbits of a hamiltonian in the KAM regime is to our knowledge unique to this system and suggests its value as a textbook example of bifurcation theory and the approach to hamiltonian chaos.

Using our analytic formulas, supplemented with numerical results for the double-barrier model we find a more complicated and interesting periodic orbit structure than in the SBM. We define a period- N orbit to be a periodic orbits which collides with the collector barrier N times before retracing itself. In the DBM it is possible to classify period- N orbits further by the number of times they collide with the emitter barrier M , so that an (M, N) orbit is a period- N orbit which collides with the emitter M times during one period. In general, for the DBM, orbits with $M = 0, 1, \dots, N$ can and do occur, although $M > N$ is forbidden by energy conservation. Bifurcations of the traversing orbit must, by continuity, produce (N, N) orbits, since the TO collides with both barriers by definition. A major finding of this work is that all relevant (M, N) orbits are related to the (N, N) orbits (and hence to the bifurcations of the traversing orbit) by subsequent sequences of tangent bifurcations which occur (for the experimental parameters) quite near the bifurcations of the TO. Thus we should consider the set of (M, N) orbits as a “family” spawned by bifurcations of the TO. However we also find, in agreement with other work^{18, 17}, that often the (N, N) orbits born at the N -fold bifurcation of the TO are not most important for the experimentally observed tunneling resonances. This will be discussed in great detail in the companion paper to this one¹³. In this paper we will develop the classical theory of these families of short periodic orbits.

First, we briefly discuss qualitatively the origin of classical chaos in this system, which we shall refer to as the “tilted well”. At zero tilt angle ($\theta = 0$) the acceleration along the electric field $\mathbf{E} = E\hat{z}$ normal to the barriers and the transverse cyclotron motion decouple and are integrable. Collisions with the barriers reverse the longitudinal component of momentum ($v_z \rightarrow -v_z$) and do not transfer energy between the cyclotron and longitudinal motion. Once the B field is tilted, so that $\mathbf{B} = B \cos \theta \hat{z} + \sin \theta \hat{y}$, between collisions the electron executes cyclotron motion around the $\hat{\mathbf{B}}$ direction, with a superimposed drift velocity $\mathbf{v}_d = (E/B) \sin \theta \hat{\mathbf{x}}$, and accelerates *along* $\hat{\mathbf{B}}$ due to the component $\mathbf{E} \cdot \hat{\mathbf{B}} = E \cos(\theta)$. This motion is still integrable. However now collisions with the barriers in general *do* mix the cyclotron and longitudinal energies ϵ_c, ϵ_L and make the total dynamics non-integrable. (When $\theta \neq 0$ longitudinal will mean parallel to the magnetic field direction $\hat{\mathbf{B}}$, and transverse will refer to the plane perpendicular to $\hat{\mathbf{B}}$). The amount of energy exchange $\Delta\epsilon = \epsilon_L - \epsilon_c$ depends sensitively on the *phase* of the cyclotron rotation at impact. For example, we shall see below that when the phase is such that the velocity falls precisely in the $x - z$ plane there is no energy-exchange ($\Delta\epsilon = 0$), and periodic orbits with this property will be of great importance. When degrees of freedom are non-linearly coupled so that the amount of energy exchange is determined by a rapidly varying phase, chaos is the inevitable result¹⁴. Since the rate of variation of the phase between collisions is $\omega_c = eB/m^*$, we expect the degree of chaos to increase with increasing B . Similarly, since the time between collisions decreases with increasing voltage, the rate of phase variation is a decreasing function of V and we expect chaos to diminish as V increases. This explains qualitatively the dependence of the chaos parameter $\beta \sim B/\sqrt{V}$ found by Shepelyansky and Stone¹⁴. To go beyond these qualitative considerations we need to perform a scaling analysis of the classical double-barrier hamiltonian, which we will describe in the next section.

This paper is organized as follows. In section II we introduce the scaled hamiltonian which is effectively two-dimensional and discuss the non-linear Poincaré map it generates, recovering the limiting behavior discussed by Shepelyansky and Stone, which is equivalent to the single-barrier model. We introduce the crucial notion of non-mixing periodic orbits. In Section III we discuss the periodic orbit structure of the SBM, deriving analytic expressions for the period and stability of all period-one orbits. We consider the bifurcations of the traversing orbits in the SBM,

enumerating the relevant period-two and period-three orbits. In section IV we turn to the double-barrier model (DBM) and derive analytic formulas for the period-one orbits there. The bifurcations of the TO in the DBM are discussed and the families of (M, N) orbits are identified. Finally, we summarize the properties of the short periodic orbits and set the stage for their use to calculate the tunneling spectra semiclassically in the companion work¹³.

II. SCALED DYNAMICS AND POINCARÉ MAP

A. Scaled Hamiltonian

We now define the Hamiltonian we will use for analyzing the classical mechanics. We neglect the coupling of the electrons to optic phonons within the well; we will take it into account in the semiclassical theory by introducing an appropriate level-broadening. The semiclassical tunneling theory expresses the tunneling current in terms of the emitter wavefunction, the tunneling rate through each barrier, and the periodic orbits of electrons trapped within the well. Therefore we are only concerned with the classical mechanics within the well and can represent the barriers by infinite hard walls separated by a distance d . The z -axis will be chosen normal to the barriers (parallel to the electric field \mathbf{E}) and with an origin such that the collector barrier is at $z = 0$ and the emitter barrier is at $z = d$. The magnetic field is tilted in the (y, z) plane, $\mathbf{B} = \cos\theta\hat{\mathbf{z}} + \sin\theta\hat{\mathbf{y}}$. We choose a gauge where the vector potential $\mathbf{A} = (-By\cos(\theta) + Bz\sin(\theta))\hat{\mathbf{x}}$. The Hamiltonian is

$$\begin{aligned} H &= \frac{(p_x - eBy\cos(\theta) + eBz\sin(\theta))^2}{2m} + \frac{p_y^2}{2m} + \frac{p_z^2}{2m} - eEz \\ &\quad + U(-z) + U(z - d) \\ &= \varepsilon \end{aligned} \tag{3}$$

where the function U ($U(z < 0) = 0$, $U(z > 0) = \infty$) represents the infinite hard walls at $z = 0, -d$.

The Hamiltonian (3) involves four variable experimental parameters: B, E, θ and d . It is of great convenience to rescale the variables in Eq. (3) so as to express the dynamics generated by this Hamiltonian in terms of the minimum number of independent parameters. This will simplify the analysis of the periodic orbits and also predict scaling relations relevant to the experimental data. We present a rescaling below which is most useful for a periodic orbit theory of both the single-barrier and double-barrier models. It is a natural extension of the simpler scaling introduced by Shepelyansky and Stone¹⁴. An alternative scaling which applies to the DBM has been introduced by Monteiro *et al*^{19,20}.

The natural unit of time for the problem is ω_c^{-1} where $\omega_c = eB/m$ is the cyclotron frequency. The barrier spacing d gives one length scale, and the only other energy independent length scale in the problem is $l_D = v_D\omega_c^{-1}$, where $v_D = E/B$ is the drift velocity for perpendicular electric and magnetic fields (the actual drift velocity when the fields cross at angle θ is $v_d \equiv v_D \sin\theta$). For electron total energies $\varepsilon < eV = eEd$ the emitter barrier is energetically inaccessible so the length scale d is irrelevant. Since we wish to introduce a dimensionless hamiltonian related to Eq. (3) by a canonical transformation, the scaling must be independent of energy and applicable to both the case $\varepsilon < eEd$ and $\varepsilon > eEd$. Hence we must scale all lengths by l_D .

In addition we want to exploit all symmetries of the Hamiltonian. The Hamiltonian (3) is independent of the coordinate x and therefore p_x is conserved, so we can see immediately that the dynamics is two-dimensional for each value of p_x . However, there is an additional symmetry related to gauge invariance: the invariance of H under all transformations of p_x and y , which keep the value of the difference $p_x - eBy\cos\theta$ unchanged. This implies that if a periodic orbit exists for one value of p_x , then an exact copy of this orbit exists for all p_x translated by the distance $\Delta y = \Delta p_x \cos\theta / eB$. Combined with the translational invariance in the x -direction this means that any periodic orbits can be arbitrarily translated in the $x - y$ plane. This is the classical analogue of the Landau-level degeneracy which is preserved in the Hamiltonian (3). We want to rescale our Hamiltonian to eliminate this classical degeneracy in p_x as well, so as to define a unique dynamics for each value of the total energy. This can be achieved by the following canonical transformation:

$$\begin{aligned} \xi &= \frac{x}{l_D} - \frac{\omega_c^{-1}p_y}{ml_D\cos\theta}, & \eta &= \frac{y}{l_D} - \frac{\omega_c^{-1}p_x}{ml_D\cos\theta}, & \zeta &= z/l_D \\ p_\xi &= \frac{\omega_c^{-1}}{ml_D}p_x & p_\eta &= \frac{\omega_c^{-1}}{ml_D}p_y & p_\zeta &= \frac{\omega_c^{-1}}{ml_D}p_z \\ \tau &= \frac{t}{\omega_c} \end{aligned} \tag{4}$$

which leads to the dimensionless Hamiltonian with two degrees of freedom :

$$H_{\text{eff}} = \frac{p_\eta^2 + p_\zeta^2}{2} + \frac{1}{2} (\eta \cos \theta - \zeta \sin \theta)^2 + \zeta + U(-\zeta) + U\left(\zeta - \frac{d}{l_D}\right) \quad (5)$$

$$= \frac{\varepsilon}{\varepsilon_D} \quad (6)$$

where rescaled energy is measured in units of the “drift energy” $\varepsilon_D = mv_D^2/2$ and may be rewritten as

$$\varepsilon/\varepsilon_D = \frac{v_0^2 B^2}{E^2} \equiv \beta^2/4.$$

Note that both the coordinate ξ and the momentum p_ξ are absent in the scaled hamiltonian which is hence truly two-dimensional.

1. DBM vs. SBM : γ parameter

The only dependence on the barrier-spacing d in the scaled hamiltonian is through the term $U(\zeta - d/l_D)$ representing the emitter barrier. As noted, when the total energy of the electron is less than the potential drop eEd across the well, the electron can not reach the emitter barrier, and the term $U(\zeta - d/l_D)$ can be removed from the equation (5). In this case, for fixed θ , the dynamics is uniquely defined by the value of the scaled energy, $\varepsilon/\varepsilon_D \equiv \beta^2/8$. This case corresponds to the single-barrier model studied by Shepelyansky and Stone¹⁴, who first showed that the dynamics of the SBM depends only on the parameter $\beta \equiv 2v_0 B/E$.

When $\varepsilon > eEd$, the electron can collide with the emitter barrier and the classical motion of the electron in such a case depends essentially on *both* d/l_D and β , leading to a more complicated and interesting dynamics. Since the crossover between these two regimes is determined by the condition $\gamma \equiv \varepsilon/eEd = 1$, we re-express the parameter d/l_D in Eq. (5) in terms of the dimensionless parameters β, γ : $d/l_D = \beta^2/(8\gamma)$, so that the dynamics in the DBM is determined by the values of β, γ . This is particularly convenient because in experiments the ratio of the emitter state energy to the applied voltage is approximately unchanged, so γ is approximately constant over the $B - V$ parameter space. Therefore both the dynamics of the SBM and the DBM can be analyzed fully by varying a single dimensionless parameter, β . This is how we will proceed in the remainder of this work.

Before making any further analysis of the dynamics we note that there is one completely general prediction which follows from the scaled hamiltonian of Eq. (5) if γ is constant. We can write

$$\beta^2 = \frac{4\gamma eV}{\varepsilon_D} = \frac{8\gamma e d^2}{m} \frac{B^2}{V}, \quad (7)$$

which implies that for a given θ the classical mechanics is constant along parabolic boundaries in the $B - V$ plane: $V = (8\gamma e d^2/m\beta^2)B^2$. This is true of the exact dynamics of the double-barrier model as long as γ is constant and the variation of effective mass with injection energy is negligible.

B. Poincaré Map

In order to analyze the two-dimensional hamiltonian dynamics of the canonical coordinates $(\eta, p_\eta; \zeta, p_\zeta)$ we use the Poincaré surface of section (SOS) method which is standard in non-linear dynamics^{21,22,3}. For fixed values of β and γ the classical trajectories in this four-dimensional phase space lie on a 3-dimensional surface determined by energy conservation. When $\theta \neq 0$ the system is non-integrable, there is no additional constant of motion other than the energy, and there exist chaotic trajectories which cover a finite fraction of this three-dimensional surface. To define the stability matrix for the periodic orbits and also to better visualize the phase-space structure we plot the behavior of a set of trajectories on a two-dimensional cross-section of this surface. The motion of an electron in the tilted well is bounded and all trajectories collide eventually with the collector barrier at $\zeta = 0$. Therefore it is convenient to choose the cross section to be the plane (p_η, η) when $\zeta = 0$ (p_ζ being then fixed by energy conservation). If an initial condition is chosen on this plane then Hamilton's equations of motion can be used to obtain the values of (η, p_η) , when the trajectory again passes through the plane $\zeta = 0$. This procedure defines a Poincaré map for the tilted well (other choices are possible, e.g. the emitter barrier map at $\zeta = d/l_D$ and may be used below).

$$\begin{aligned}\eta_{n+1} &= \Phi_q(\eta_n, (p_\eta)_n) \\ (p_\eta)_{n+1} &= \Phi_p(\eta_n, (p_\eta)_n)\end{aligned}\tag{8}$$

Since every orbit reaches the collector barrier, *every* periodic orbit of the hamiltonian (5) corresponds to either a fixed point of the Poincaré map (period-1 orbits) or to a fixed point of the N -th iteration of the Poincaré map (period- N orbits).

Note that the coordinates η and momentum p_η are proportional to the x - and y - components of the *velocity* of the electron in the original coordinate system :

$$\begin{aligned}v_x &= -\frac{l_D \cos \theta}{T_c} \eta \\ v_y &= \frac{l_D}{T_c} p_\eta\end{aligned}\tag{9}$$

This property allows us to relate the Poincaré map (8) in the coordinates (η, p_η) to an equivalent Poincaré map in more familiar coordinates $(v_x/v_0, v_y/v_0) \equiv (\tilde{v}_x, \tilde{v}_y)$, which describes the evolution of the velocity components of the electron in the plane perpendicular to the collector barrier:

$$\begin{aligned}(\tilde{v}_x)_{n+1} &= \Phi_x((\tilde{v}_x)_n, (\tilde{v}_y)_n) \\ (\tilde{v}_y)_{n+1} &= \Phi_y((\tilde{v}_x)_n, (\tilde{v}_y)_n)\end{aligned}\tag{10}$$

$$(11)$$

where the relations between Φ_x, Φ_y and Φ_q, Φ_p follow from Eqs. (9) and (8).

Note that we have scaled the velocities by the maximum allowed velocity v_0 so that the values of this Poincaré map will be contained within the unit circle, independent of the energy (this would not be true of the variables (η, p_η) as the size of the energetically allowed region of the plane varies with the scaled energy $\beta^2/4$). Although the variables (η, p_η) were most convenient for discussions of scaling, we will use the energy-scaled velocity map (10) henceforth since it is easiest to interpret and compare for varying β values.

A plot of the Poincaré map (10), which is called *Surface of Section* (SOS) is generated by choosing a grid of initial conditions in the plane $(v_x/v_0, v_y/v_0)$ corresponding to a particular value of β and iterating the map many times for each initial condition. Period- N stable orbits appear as “chains” of N “islands”; whereas period- N unstable orbits will be imbedded in the chaotic layers between the islands²² and are not evident to the (untrained) eye. In Fig. 1 we show several examples of the collector barrier SOS as β is increased for fixed $\gamma = 1.15$ (which corresponds to the approximate value in the relevant experiments¹¹).

When $\theta = 0$ the squared distance of a point in the SOS from the origin is proportional to the cyclotron energy, which is conserved, so each trajectory must lie on a circle (see Fig. 1a). When $\theta \neq 0$ (Fig. 1b) we immediately see the appearance of stable islands and chaotic layers, coexisting with slightly distorted circular curves which represent the unbroken tori according to the standard KAM scenario²¹. For larger β (Fig. 1c) no KAM curves survive and the entire SOS is chaotic except for a few surviving stable islands, which however typically represent the features of most importance for the experimental tunneling oscillations.

We now undertake a more explicit determination of the properties of the Poincaré map for the tilted well. To calculate the functions Φ_p and Φ_q of the Poincaré map, one has first to analyze the motion of the electron between collisions. This motion is integrable and is most easily represented in a frame of reference (denoted by (x', y', z')), rotated by the tilt angle θ around the x axis, so that z' is parallel to the direction of the magnetic field :

$$\begin{aligned}x' &= x \\ y' &= y \cos \theta - z \sin \theta \\ z' &= y \sin \theta + z \cos \theta\end{aligned}$$

In this frame of reference the motion of the electron in the (x', y') plane between collisions is a superposition of the cyclotron rotation with the frequency $\omega_c \equiv 2\pi/T_c$ and a uniform drift along x' with the velocity $v_d = E \sin \theta / B \equiv v_D \sin \theta$, while the longitudinal motion is a uniform acceleration :

$$\begin{aligned}v_{x'}(\tau) &= v_c \cos(\phi^0 + \tau) - v_d \\ v_{y'}(\tau) &= v_c \sin(\phi^0 + \tau) \\ v_{z'} &= v_{z'}^0 - \frac{E \cos \theta}{m} t = v_{z'}^0 - \frac{l_D \cos \theta}{T_c} \tau\end{aligned}\tag{12}$$

where v_c is the cyclotron velocity (which remains constant between collisions) and ϕ^0 is the initial phase of the cyclotron rotation.

The energies associated with the transverse (cyclotron) and longitudinal motion are separately conserved between collisions. For $\theta \neq 0$ the cyclotron and longitudinal motions get mixed by the collisions with the barriers¹⁴:

$$\begin{aligned}\bar{v}_{z'} &= -\cos(2\theta)v_{z'} + \sin(2\theta)v_{y'} \\ \bar{v}_{y'} &= \sin(2\theta)v_{z'} + \cos(2\theta)v_{y'} \\ \bar{v}_{x'} &= v_{x'}\end{aligned}\tag{13}$$

where \mathbf{v} and $\bar{\mathbf{v}}$ are the velocities immediately before and after collision respectively. This transformation is equivalent to a clockwise rotation of the velocity vector by 2θ in the $(y' - z')$ plane, followed by a reflection $v_{z'} \rightarrow -v_{z'}$; hence it leaves no vector in this plane invariant (for $\theta \neq 0$). Therefore generically there *is* exchange of kinetic energy between the longitudinal and cyclotron motion at each collision

$$\delta\varepsilon_{L \leftrightarrow c} = \frac{m}{2} (v_{z'} \cos \theta - v_{y'} \sin \theta)^2 \equiv \frac{m}{2} v_y^2\tag{14}$$

and the dynamics is non-integrable.

Note that it is *possible* to have zero energy exchange upon collision for $\theta \neq 0$. The condition for this is simply that $v_y = 0$ at collision, i.e. the cyclotron phase is such that the instantaneous motion is in the $x - z$ plane. The reason that no energy is exchanged in this case is that the impulse at collision is purely in the z -direction and reverses this component of velocity leaving v_x and v_y unchanged. If $v_y = 0$ at the time of collision then $v_{z'} = v_z \cos \theta \rightarrow \bar{v}_{z'} = -v_z \cos \theta = -v_{z'}$ and the longitudinal kinetic energy is conserved. Stable period-one orbits with $v_y = 0$ ($p_\eta = 0$) are visible in both Figs. 1b,1c. We refer to these as *non-mixing* orbits since they involve no energy exchange; they will play a fundamental role in the periodic orbit theory developed below.

The transformation equations for \mathbf{v}' due to collisions at the emitter barrier are identical to (13). As we shall see below, it is useful to consider the dynamics in yet a third frame of reference which is parallel to the primed frame, but moving with the drift velocity v_d in the x' direction. In this moving frame the transverse motion is pure cyclotron rotation and each iteration of the Poincaré map is just a pair of non-commuting orthogonal transformations of the velocity: first the continuous cyclotron rotation around the z' axis, followed by the instantaneous rotation/reflection around the x' axis. Since the latter is known explicitly (Eq. (13)), to get an explicit formula for the Poincaré map what is needed is an expression for the increment in the cyclotron phase between collisions. However, there is no simple general formula for this phase increment for $\gamma > 1$ because after a collision with the collector barrier an orbit may or may not have enough longitudinal energy to collide with the emitter barrier before its next collision with the collector. Since $v_{y'}$ changes discontinuously in a collision, the cyclotron phase increment will change discontinuously due to the emitter collision. If one varies the initial conditions of a trajectory so that it ceases colliding with emitter barrier in the next iteration of the map, one can show that the phase jump goes to zero as the impulse at the emitter goes to zero (i.e. as v_z at collision goes to zero), but its derivative is discontinuous. Hence, in general the Poincaré map for $\gamma > 1$ does not have continuous derivatives everywhere on the surface of section. As a consequence the stability matrix of periodic orbits for the exact map for $\gamma > 1$ is not always defined. This has significant and novel consequences for the behavior of periodic orbits in the DBM: these can vanish without reaching marginal stability in a new kind of bifurcation we will refer to as a *cusplike bifurcation*. We shall return to this in detail below.

As a result of this discontinuous behavior we can only present a simple explicit form of the Poincaré map in certain limiting cases. The simplest of these, previously analyzed by Shepelyansky and Stone¹⁴, is when $\gamma < 1$ ($\varepsilon < eV$), in which case no orbit reaches the emitter barrier and classically the problem is equivalent to the motion of an electron in an infinite triangular well in a tilted B field. We now briefly review this limit.

C. The Single-Barrier Model (SBM)

When $\gamma \leq 1$, the cyclotron phase increment between collisions with the collector barrier is $\omega_c t_0$, where t_0 is the time it takes the electron launched “upwards” after the collision in the effective electric field, $\mathbf{E} \cos \theta$, to fall back down and hit the collector. The resulting Poincaré map takes the form :

$$\begin{aligned}\Phi_x(\tilde{v}_x, \tilde{v}_y) &= \mathcal{V}_x(\tilde{v}_x, \tilde{v}_y, \tilde{v}_z; \omega_c t_0) \\ \Phi_y(\tilde{v}_x, \tilde{v}_y) &= \mathcal{V}_y(\tilde{v}_x, \tilde{v}_y, \tilde{v}_z; \omega_c t_0)\end{aligned}\tag{15}$$

where

$$\begin{aligned}
\mathcal{V}_x(\tilde{v}_x, \tilde{v}_y, \tilde{v}_z; \tau) &= \tilde{v}_x \cos(\tau) - \tilde{v}_y \cos \theta \sin(\tau) \\
&\quad + \tilde{v}_z \sin \theta \sin(\tau) - (2/\beta) \sin \theta (1 - \cos(\tau)) \\
\mathcal{V}_y(\tilde{v}_x, \tilde{v}_y, \tilde{v}_z; \tau) &= \tilde{v}_x \cos \theta \sin(\tau) + \tilde{v}_y (\cos^2 \theta \cos(\tau) + \sin^2 \theta) \\
&\quad + \tilde{v}_z \sin \theta \cos \theta (1 - \cos(\tau)) \\
&\quad + (2/\beta) \sin \theta \cos \theta (\sin(\tau) - \tau),
\end{aligned} \tag{16}$$

the scaled velocity $\tilde{\mathbf{v}} \equiv \mathbf{v}/v_0$ (with $\tilde{v}_z(\tilde{v}_x, \tilde{v}_y) \equiv \sqrt{1 - \tilde{v}_x^2 - \tilde{v}_y^2} > 0$) and the time interval $t_0(\tilde{v}_x, \tilde{v}_y)$ between successive collisions of the electron with the collector barrier is the first positive root of the equation :

$$0 = z(t_0) \equiv \frac{v_0 \mathcal{Z}(\tilde{v}_x, \tilde{v}_y, \tilde{v}_z; \omega_c t_0)}{\omega_c} \tag{17}$$

where the function $\mathcal{Z}(\tilde{v}_x, \tilde{v}_y, \tilde{v}_z; \tau)$ is defined as

$$\begin{aligned}
\mathcal{Z}(\tilde{v}_x, \tilde{v}_y, \tilde{v}_z; \tau) &= -\tilde{v}_x \sin \theta (1 - \cos(\tau)) + \tilde{v}_y \sin \theta \cos \theta (\tau - \sin(\tau)) \\
&\quad + \tilde{v}_z (\tau \cos^2 \theta + \sin^2 \theta \sin(\tau)) \\
&\quad - (2/\beta) \left(\sin^2 \theta (1 - \cos(\tau)) + \cos^2 \theta \frac{\tau^2}{2} \right)
\end{aligned} \tag{18}$$

If $\omega_c T \gg 1$, an approximate root is found easily,

$$T = \frac{\beta \tilde{v}_{z'}}{\cos \theta}. \tag{19}$$

In this approximation the map when transformed to the (x', y', z') coordinates becomes identical¹⁴ to the kicked-top map introduced by Haake^{23, 24}.

As is indicated by the numerical analysis of both the kicked-top map and of the exact mapping (15), the KAM transition to chaos takes place when $\theta\beta \sim 1$. We therefore take the limit $\beta \gg 1$ and $\theta \ll 1$. In this case both the kicked-top map and the exact map (15) in the vicinity of a particular value of $\tilde{v}_{z'} = \tilde{v}'$ can be expressed precisely in the form of a local standard map (kicked rotor)^{16, 21}

$$\begin{aligned}
I_{n+1} &= I_n + K \sin \phi_{n+1} \\
\phi_{n+1} &= \phi_n + I_n
\end{aligned} \tag{20}$$

where

$$\begin{aligned}
I_n &= \beta \tilde{v}_{z'} \\
K &= 2\theta\beta \sqrt{1 - (\tilde{v}')^2}
\end{aligned} \tag{21}$$

and ϕ is the phase of the cyclotron rotation.

The map is called local because the kick strength varies with $v_{z'}$, so that the chaos boundary, given by the condition¹⁶ $K \approx 1$ varies with $v_{z'}$. The resulting condition for chaos as an explicit function of all system parameters is¹⁴:

$$B^2 > \frac{mE\varepsilon}{32e\theta^2\varepsilon_c} \tag{22}$$

where $\varepsilon_c \equiv \varepsilon(1 - (\tilde{v}')^2)$ is the instantaneous energy of the cyclotron motion.

Although the estimate (22) was obtained only in the limiting case $\theta \ll 1$ and $\beta \gg 1$, it does predict the correct behavior of the exact mapping (15) for the SBM. Qualitatively it predicts that chaos increases with increasing magnetic field and energy and with decreasing electric field and quantitatively the condition given by Eq. (22) is in good agreement with the onset of complete energy exchange between the cyclotron and longitudinal motion as determined from simulations of the exact map¹⁴.

D. The Double-Barrier Model (DBM)

When $\gamma = \varepsilon/eV > 1$, the electron can retain enough longitudinal energy on collision with the collector barrier to reach the emitter wall, although it need not do so. If we regards the coordinates $(\tilde{v}_x, \tilde{v}_y)$ in the SOS as initial

conditions for the next segment of the trajectory, we may partition the SOS into inner and outer regions. Initial conditions $(\tilde{v}_x, \tilde{v}_y)$ in the inner region will define all trajectories which collide with the emitter before their next collision with the collector. For such initial conditions the equation

$$z(t) \equiv \frac{v_0 \mathcal{Z}(\tilde{v}_x, \tilde{v}_y, \tilde{v}_z; \omega_c t)}{\omega_c} = d \equiv \frac{v_0}{\omega_c} \frac{\beta}{4\gamma} \quad (23)$$

where the function \mathcal{Z} was defined in (18), must have a positive root $t = t^\uparrow$, which corresponds to the time interval to the next collision with the emitter barrier.

For initial conditions in the outer region Eq. (23) has no positive roots, the electron does not reach the emitter barrier before the next collision with the collector barrier, and its trajectory is exactly the same as in the SBM for this iteration of the map. Hence the Poincaré map is still given by the expression (15).

The “critical boundary” between the two regions is the curve $(\tilde{v}_x^{(c)}, \tilde{v}_y^{(c)})$, such that the electron launched from the collector barrier with the velocity $\mathbf{v} = v_0(\tilde{v}_x^c, \tilde{v}_y^c, \tilde{v}_z^c)$, will reach the emitter wall with component of the total velocity perpendicular to the plane of the barrier equal to zero. For $\theta = 0$ the critical boundary is a circle given by the equation :

$$\tilde{v}_x^2 + \tilde{v}_y^2 = 1 - 1/\gamma \equiv \frac{\varepsilon - eV}{\varepsilon} \quad (24)$$

In Fig. 2 we show a few examples of the “critical boundary” for different values of β and γ . It is important to realize that in general trajectories can cross the critical boundary and indeed for large chaos parameter almost all trajectories do. However knowledge of the critical boundary is useful for formulating the Poincaré map of the DBM.

For $(\tilde{v}_x, \tilde{v}_y)$ outside the critical boundary, the next iteration of the Poincaré map does not involve the collision with the emitter barrier, and the Poincaré map is therefore still given by (15), as in the single barrier model.

When $(\tilde{v}_x, \tilde{v}_y)$ is inside the critical boundary, then the Poincaré map is given by :

$$\begin{aligned} \Phi_x(\tilde{v}_x, \tilde{v}_y) &= \mathcal{V}_x(\tilde{v}_x^e, \tilde{v}_y^e, \tilde{v}_z^e; \omega_c t^\downarrow) \\ \Phi_y(\tilde{v}_x, \tilde{v}_y) &= \mathcal{V}_y(\tilde{v}_x^e, \tilde{v}_y^e, \tilde{v}_z^e; \omega_c t^\downarrow) \end{aligned} \quad (25)$$

where $\tilde{\mathbf{v}}_e$ is the scaled velocity immediately after collision with the emitter barrier and can be obtained as

$$\begin{aligned} \tilde{v}_x^e &= \mathcal{V}_x(\tilde{v}_x, \tilde{v}_y, \tilde{v}_z; \omega_c t^\uparrow) \\ \tilde{v}_y^e &= \mathcal{V}_y(\tilde{v}_x, \tilde{v}_y, \tilde{v}_z; \omega_c t^\uparrow) \\ \tilde{v}_z^e &= -\sqrt{1 - \tilde{v}_x^2 - \tilde{v}_y^2} \end{aligned} \quad (26)$$

t^\uparrow is defined as the time interval until the next collision with the emitter barrier and is given by the first positive root of the equation (23), and the parameter t^\downarrow represents the time interval between the collision with the emitter barrier and the next collision with the collector map. The value of t^\downarrow can be obtained from the equation

$$d + \frac{v_0}{\omega_c} \mathcal{Z}(\tilde{v}_x^e, \tilde{v}_y^e, \tilde{v}_z^e; \omega_c t^\downarrow) = 0 \quad (27)$$

As noted above, an important property of the Poincaré map (25) is that it has a discontinuous derivative as the initial conditions $(\tilde{v}_x, \tilde{v}_y)$ are varied across the critical boundary. Therefore the conditions for the global validity of the KAM theorem are not satisfied by this map and the transition to chaos can be discontinuous here as in the stadium billiard²⁶. However unlike the stadium billiard not all trajectories are affected by the discontinuity of the map for arbitrarily small chaos parameter. Away from the critical boundary the map satisfies all the conditions for the existence of KAM tori and, for small chaos parameter, in the inner and outer regions there will exist an outermost and innermost KAM torus. These two tori will define a set of trajectories which either always hit the emitter barrier (lie within the outermost KAM curve of the inner region) or always miss the barrier (lie outside the innermost KAM curve of the outer region). Between these two tori the non-analyticity of the map is felt by the trajectories and the numerics demonstrates clearly that there are no remaining KAM curves in an annular region bounded approximately by the maximum and minimum cyclotron energies of points on the critical boundary. In this region the chaos does not appear to be associated with the separatrices corresponding to the hyperbolic fixed points as it would be for small chaos parameter in a KAM system. The practical consequence is that one observes an anomalously large “chaotic halo” around the critical boundary (see Fig. 3). In this region the effective map description fails badly and only analysis of the exact map can be used. In fact, as we shall see below, many of the important short periodic orbits

first appear *at* the critical boundary at a finite value of β and emerge from the chaotic halo region with increasing β . We will be able to develop an analytic theory of the simplest such orbits from the exact map.

Although the effective map based on the SBM fails in the “halo” region, for small chaos parameter and small θ it should work just as well in the outer region of the SOS as it does in the SBM, since here the trajectories are prevented by the innermost KAM curve from reaching the emitter and the DBM Poincaré map is *identical* to the SBM. Since the local chaos parameter in the effective map description of the SBM is $K = 2\beta\theta\sqrt{1 - (\tilde{v}')^2}$ the chaos is weakest at the innermost KAM curve of the outer region (since the cyclotron energy is the smallest there) and this curve is the last in the outer region to break. The quantitative prediction for the breaking of this curve from the local standard map approximation (Eq. (20)) is in a good agreement with the exact behavior.

One may try to extend similar reasoning to the inner region of trajectories which always reach the emitter barrier. Here the effective map is clearly somewhat different because of the additional energy exchange (“kick”) at the emitter barrier. It *is* possible to obtain an effective area-preserving map for small tilt angles which is similar to a standard map with two unequal kicks per period. However the SOS generated by this approximation has little similarity to the exact map. This is because when the energy is almost completely longitudinal (as it is in this region of phase space) the kick strength goes to zero at leading order in the tilt angle and the effective map description fails. Note that it is precisely the periodic orbits in the inner region (which reach the emitter) which are measured in the tunneling spectrum. Thus we are particularly interested in obtaining a good description of this region of phase space and must work with the exact map described by Eqs. (25).

Fortunately, as we show below, it is possible to obtain a good theoretical understanding of the short periodic orbits in the entire phase space, including the crucial central region of the SOS, based on analysis of the exact map. In fact we are able to obtain analytic expressions for the period and stability of an infinite class of important periodic orbits for arbitrarily large values of the chaos parameter.

III. PERIODIC ORBIT THEORY (SINGLE-BARRIER MODEL)

A. Integrable Behavior

Eq. (1) of Section I gives a quantitative semiclassical formula for the tunneling current through the tilted well in terms of the contributions of different periodic orbits which connect emitter and collector barriers. Clearly these orbits can be fully described only within the framework of the double barrier model. Nevertheless, the behavior of the periodic orbits in the DBM as a function of tilt angle and β is exceedingly complex and has not been understood systematically up to this point. In order to develop such a systematic understanding it is very helpful to consider the SBM, which has a similar but simpler periodic orbit structure. The similarity between the two models is easily seen by considering the limit of zero tilt angle.

When $\theta = 0$, both systems are integrable and all of the periodic orbits can be divided into two groups. A *single* traversing orbit (TO) bouncing perpendicular to the barrier(s) with zero cyclotron energy and infinite families of helical orbits (HO) with periods equal to an integer multiple of the cyclotron period, $2\pi/\omega_c$. The traversing orbit corresponds to the fixed point of the Poincaré map in the centre (0,0) of the surface of section - see Fig. 1; its period is given by

$$T_{\text{TO}} = \frac{\beta}{\omega_c} \quad (\text{SBM}) \quad (28)$$

$$T_{\text{TO}} = \frac{\beta}{\omega_c} \left(1 - \sqrt{1 - \frac{1}{\gamma}} \right) \quad (\text{DBM}) \quad (29)$$

Unlike all other one-bounce orbits, the TO exists for arbitrarily small energy, since its frequency need not be in resonance with the cyclotron frequency. Since it has zero cyclotron energy its semiclassical quantization yields the states of the well with Landau index equal to zero, and hence the TO determines the sub-band energy spacings of the triangular (SBM) or trapezoidal (DBM) well by the semiclassical rule for integrable systems: $\Delta\varepsilon = \hbar/T_{\text{TO}}$.

Due to the rotational invariance of the system at zero tilt angle all other periodic orbits in the well (in both the SBM and DBM) exist in degenerate families related by rotation around the z-axis. The union of all trajectories in a family defines a torus in phase-space, known as a “resonant” torus in the nonlinear dynamics literature²² because the periodic motion of the two degrees of freedom are commensurate:

$$n\omega_c = k\omega_L \quad (30)$$

where n and k are integers (which do not have a common divisor) and ω_L is the frequency of the periodic motion in the longitudinal direction). Since longitudinal and transverse motion decouple, ω_L is the frequency of the periodic motion of the uniformly accelerated electron bouncing normal to the barriers, and its value is :

$$\omega_L = \frac{2\pi\omega_c}{\beta\sqrt{\tilde{\varepsilon}_L}} \quad (\text{SBM}) \quad (31)$$

$$\omega_L = \frac{2\pi\omega_c}{\beta\sqrt{\tilde{\varepsilon}_L}} \times \begin{cases} 1 & \gamma\tilde{\varepsilon}_L < 1 \\ \left(1 - \sqrt{1 - \frac{1}{\gamma\tilde{\varepsilon}_L}}\right)^{-1} & \gamma\tilde{\varepsilon}_L \geq 1 \end{cases} \quad (\text{DBM}) \quad (32)$$

where $\tilde{\varepsilon}_L \equiv \tilde{v}_z^2$ is the scaled longitudinal energy.

The resonance condition (30) means that any periodic orbit of a family labelled by the integers n and k collides with the collector barrier n times while making k full cyclotron rotations before retracing itself. Therefore all such orbits in real-space trace out rational fractions of a helix (hence the term helical orbits) between successive collisions and have periods given by

$$T_{\text{HO}} = \frac{2\pi k}{\omega_c} \quad (33)$$

for both the SBM and DBM.

A simplifying feature of these systems is that one of the oscillation periods, the cyclotron period, is independent of energy and voltage. The longitudinal period varies with both energy and voltage, going to zero as longitudinal energy tends to zero. If a family of helical orbits (n, k) exists at a given energy, a family of the same type can be generated at a lower energy by simply removing cyclotron energy (hence reducing the cyclotron radius) until the radius of the helix shrinks to zero, at which point this “family” has become degenerate with the TO and ceases to exist. These degeneracy points occur then, whenever the period of the traversing orbit T_{TO} passes through the value kT_c/n , for both the SBM and DBM.

When the magnetic field is tilted the rotational symmetry around the field direction which was the origin of continuous families of helical orbits in the well is broken and *all* the resonant tori are destroyed. According to the Poincaré - Birkhoff theorem²¹ each of them is replaced by an integer number of pairs of stable and unstable orbits (normally just a single pair). The degeneracy points of the untilted system, at which an (n, k) resonant torus collapsed, evolve into n -fold bifurcations of the TO.

The reason that the periodic orbit theory of the DBM is more complicated than that of the SBM stems from two facts. 1) In the unperturbed DBM there are two distinct families of orbits for each pair (n, k) (one which reaches the emitter and one which doesn't), whereas there is only one such family in the SBM. 2) These families can collapse at the critical boundary and not just by reaching degeneracy with the TO. However in all the other respects mentioned above the two models are similar, and in particular, the bifurcations near the TO, which are crucial for explaining the experimental data of Muller et al.¹¹, are very similar in the two models. We thus begin with the simpler case of the SBM²⁵.

B. Periodic Orbits at $\theta = 0$

As just noted, the periodic orbits at $\theta = 0$ are of two types: the (usually) isolated traversing orbit and the families of helical orbits. The TO, with no cyclotron energy has a period which is independent of magnetic field and monotonically increasing from zero with increasing energy:

$$T_{\text{TO}} = \frac{2\sqrt{2m^*\varepsilon}}{eE} \equiv \frac{\beta}{\omega_c} \quad (34)$$

For all HO's the period is finite and an integer multiple of $T_c = 2\pi/\omega_c$. Thus a given family of HO's labelled by (n, k) can only exist above the energy at which $nT_{\text{TO}} = kT_c/n$. These thresholds are the degeneracy points discussed above. At the threshold all energy longitudinal ($\text{varepsilon}_{\text{long}} = 1$); together with (30),(31) this yields :

$$\beta_{(n,k)} = \frac{2\pi k}{n}. \quad (35)$$

Since $0 \leq \text{varepsilon}_{\text{long}} \leq 1$, for values of $\beta > \beta_{(n,k)}$ there always exists exactly one root of the equation

$$\tilde{\varepsilon}_L(n, k) = \left(\frac{2\pi k}{\beta n} \right)^2 \quad (36)$$

where $\tilde{\varepsilon}_L = \tilde{v}_z^2$ is the *scaled* longitudinal energy. The scaled cyclotron energy for this family (resonant torus) is just $\tilde{v}_c^2 = 1 - \tilde{\varepsilon}_L$. As the value of β is increased, the existing helical orbits gain more cyclotron energy and move away from the traversing orbit, allowing for the creation of new families of HO near the TO. We will now analyze what happens to the shorter periodic orbits as the magnetic field is tilted, beginning with the one-bounce orbits.

C. One-bounce orbits

1. Continuity argument

One-bounce orbits are periodic orbits which have retraced themselves between each bounce off the single barrier, i.e. they are fixed points of the first iteration of the Poincaré map. Note that different one-bounce orbits may have widely differing periods, and may for instance have periods longer than two or three bounce orbits. For $\theta = 0$ the existing one-bounce orbits consist of the TO and all HO families with $n = 1$ which are above threshold, i.e. with $k < \beta/2\pi$. The behavior of the periods of these orbits is indicated by the dashed lines in Fig. 4. Since the periods T of the HO families are fixed to be integer multiples of T_c they are independent of β when we plot $\omega_c T$.

When the magnetic field is infinitesimally tilted, all helical families (resonant tori) are immediately destroyed and replaced by pairs of stable and unstable periodic orbits. These surviving one-bounce orbits are only infinitesimally distorted from their analogs at $\theta = 0$ and by continuity the periods of these orbits are also only infinitesimally altered. For our system it is clear which orbits from each infinite family survive. For each helical family there are exactly two orbits which collide with the barrier with $v_y = 0$, the condition for zero energy exchange according to Eq. (14). It is these two orbits from each family which survive. This is easily seen by recalling that longitudinal and transverse energy are separately conserved between collisions even in the tilted system, so any *one-bounce* periodic orbit for arbitrary tilt angle must also conserve these quantities during the collision. But the condition for this is just $v_y = 0$, which is satisfied for the two one-bounce helical orbits from each family which hit with $v_x = \pm v_c$. By continuity these two orbits must evolve into the two surviving isolated fixed points of the map under tilting of the field. However this tilt spoils the $y \rightarrow -y$ symmetry of the system, so these two orbits are no longer symmetry-related and their periods differ, one becoming longer than kT_c and the other becoming shorter. As a result each of the horizontal lines in Fig. 4a, which there represent the one-bounce HO families, splits into an upper and lower branch representing these two orbits. Moreover for infinitesimal tilt angle one of these branches must be stable and one unstable (the lower branch is the stable one as we shall see below). Finally, there is no longer a qualitative difference between the TO and the HO's once the field is tilted. For $\theta \neq 0$ the TO is required to have non-zero transverse energy in order to satisfy the $v_y = 0$ condition and since it was degenerate with the $(1, k)$ family of HOs at $\beta = 2\pi k$ it must be continuously deformable into one of the HOs near these points.

To label the single-bounce orbits, it is convenient to introduce the following notation :

$$(1)^{\pm(k)}$$

which means, that it is a single - bounce periodic orbit (“1”) with the period T such that $kT_c < T < (k+1)T_c$. To distinguish the two orbits, which for $k \geq 1$ can satisfy this inequality, we introduce an additional index \pm , such that the sign “-” corresponds to the periodic orbit with a smaller period (we use this notation in fig. 4)

The qualitative behavior of the complete set of one-bounce orbits of the SBM follows from these continuity arguments and is shown in Fig. 4, where for definiteness we have plotted the exact analytical results of the next subsection. Note that for $\beta \neq 2\pi k$ there is always one orbit with a nearly linear variation of its period with β . This is the $(1)^{+k}$ orbit and it is the analog of the TO of the untilted system. However near $\beta = 2\pi k$ the period of each of the $(1)^{+k}$ orbit saturates to kT_c as it becomes primarily helical, while a new pair of orbits is born at a tangent bifurcation near $\beta = 2\pi k$. One of these, the $(1)^{+(k+1)}$ takes over the role of the TO while the other, the $(1)^{-(k+1)}$ becomes the unstable partner of the helical orbit generated by the $(1)^{+k}$ orbit. Thus, qualitatively speaking, the system repeats itself every time β is increased by 2π . Quantitative scaling relations between the behavior in each interval are discussed in Appendix B. Note finally that the continuity argument suggests that in the tilted system the period kT_c is forbidden for one-bounce orbits since the two surviving HO's from each resonant torus are shifted away from this value and the period of the “TO” can no longer cross that of the HOs as β varies; we shall prove this statement rigorously shortly.

2. Quantitative theory

We now derive exactly the periods of all one-bounce orbits for arbitrary tilt angle. We also prove that there can exist no one-bounce orbit not identified by the continuity argument given above. As just noted, it is trivial to see that all one-bounce orbits must be non-mixing (i.e. bounce with $v_y = 0$) for any tilt angle. Therefore we can impose this condition in order to find all one-bounce orbits and their periods. The derivation is most easily performed in the coordinate system (x'', y'', z'') , which *moves* in the direction perpendicular to B and E with the drift velocity $v_d = E \sin(\theta)/B$:

$$\begin{aligned} x'' &= x' - v_d t \\ y'' &= y' \\ z'' &= z' \end{aligned} \tag{37}$$

Projected on the plane (x'', y'') , the trajectory of the electron between successive collisions is a portion of a circle of radius v_c/ω_c with an angular size $\omega_c T$, where v_c is the cyclotron velocity and T is the time interval between collisions (period of the 1-bounce orbit). For $T > 2\pi/\omega_c$ the trajectory retraces the circle several times (see Fig. 5). Any orbit which is periodic in the lab frame will not be so in the drift frame, instead the initial and the final points of the trajectory between successive collisions must be separated by the distance $\delta x'' = v_d T$ (where T is the period of the orbit) and have the same value of y'' . On the other hand, for one-bounce periodic orbits the distance $\delta x''$ can be expressed as (see Fig. 5)

$$\delta x'' = 2v_c/\omega_c \sin(\alpha) = 2v_c/\omega_c \sin(\omega_c T/2),$$

so that

$$v_c = v_d \frac{\omega_c T/2}{\sin(\omega_c T/2)}$$

and at the point of collision therefore

$$\begin{aligned} v_{x''}|_{z=0} &= v_d (\omega_c T/2) \cot(\omega_c T/2), \\ v_{y''}|_{z=0} &= v_d (\omega_c T/2) \end{aligned} \tag{38}$$

Since the motion along the direction of the magnetic field $\hat{z}'' = \hat{B}$ is a uniform acceleration under the force $eE \cos(\theta)/m$, at the point of collision

$$v_{z''} = \frac{eE \cos(\theta)}{m\omega_c} \frac{\omega_c T}{2} \tag{39}$$

Note, that at the point of collision $v_y = v_{y''} \cos(\theta) - v_{z''} \sin(\theta) = 0$, as expected.

Substituting v'' into the equation of energy conservation $\varepsilon = m(\mathbf{v}'' - \mathbf{v}_d)^2/2$ at the barrier, we finally obtain :

$$\frac{(\beta/2)^2 - (\omega_c T/2)^2}{[1 - (\omega_c T/2) \cot(\omega_c T/2)]^2} = \sin^2(\theta). \tag{40}$$

This is the basic equation determining the periods $T(\beta, \theta)$ for all one-bounce orbits. As $\beta \rightarrow 0$ the only solutions which exist require $T \rightarrow 0$ also, and it is easily seen by expanding the left-hand side that there is in fact only one solution for any value of θ , and this solution has $\beta = \omega_c T$ as for the TO in the unperturbed system. For any β there are no solutions with $\omega_c T = 2\pi k$ (as argued above) due to the divergence of the denominator in the left-hand side at these values. If there were solutions with this value of the period, then viewed in the drift frame the orbit would be an integer number of full circles, which is one can see intuitively is impossible due to the collision (see. Fig. 5).

For $\beta \gg 2\pi k$ there are many solutions as can be easily shown graphically by plotting the single-valued function

$$\beta = \mathcal{F} \left(\sin \theta, \frac{\omega_c T}{2} \right) \tag{41}$$

where

$$\mathcal{F}(x, y) = 2\sqrt{y^2 + x^2 (1 - y \cot y)^2} \tag{42}$$

as is done in Fig. 4.

The single solution at $\beta < 2\pi k$ corresponds to the $(1)^{+0}$ which is a slightly deformed version of the TO; it is visible as the central island in the SOS of Fig. 6a with $v_y = 0$ (as is required, cf. above discussion), but with now some small value of \tilde{v}_x . As β is increased, this orbit gains cyclotron energy, and the corresponding fixed point moves away from the center to the left side of the surface of section. As discussed above, for $\beta > 2\pi$ the period of the orbit $(1)^{+(0)}$ approaches asymptotically T_c as the majority of its energy is fed into transverse motion and it becomes a recognizable deformation of a $k = 1$ helical orbit of the untilted system (see Figs. 4, 6b).

The two new orbits $(1)^{\pm k}$ which must arise by continuity in each interval appear in tangent bifurcations at thresholds given by $\beta = \beta_k^{\text{tb}}$, where

$$\beta_k^{\text{tb}} = \mathcal{F}(\sin \theta, \varrho_k) \quad (43)$$

and ϱ_k is the k -th positive root of the equation

$$\frac{\varrho \tan \varrho}{(1 - \varrho \cot \varrho)(1 + 2\varrho \csc \varrho)} = \sin^2 \theta.$$

This is clearly seen in the SOS of Fig. 6b, the fixed point of the stable periodic orbit $(1)^{+(1)}$ is at the center of the stable island near the origin, whereas its unstable partner is (less obviously) visible as the elongated flow pattern at $v_y = 0$ and slightly larger values of v_x . The evolution of these orbits above threshold is precisely as predicted by the continuity argument above: the $(1)^{+k}$ initially has a period close to that of the TO before saturating to $T \approx (k+1)T_c$; whereas the $(1)^{-k}$ orbit immediately becomes helical with $T \approx kT_c$. We must emphasize that Eq. (40) uniquely identifies all one-bounce orbits for arbitrary θ . Thus there are no one-bounce orbits for any θ which cannot be related to one-bounce orbits of the untilted system (this is not the case for period-two and higher orbits). Hence we have a qualitative and quantitative understanding of the periods and topology of all one-bounce orbits. The next issue to address is their stability properties.

3. Stability

We define the stability of a periodic orbit in the standard manner^{22,21}. The non-linear Poincaré velocity map (Eq. (15)) is linearized for small deviations of the initial velocity from the values corresponding to the periodic orbit (fixed point of the map). This linear map is represented by a 2×2 *monodromy* matrix M_1 which has determinant one due to conservation of phase-space volume in the hamiltonian flow. The PO is unstable if one of the eigenvalues of M_1 has modulus larger than one (the other being necessarily less than one), so that an initial deviation along the associated eigenvector grows exponentially. The PO is stable if the eigenvalues are $e^{\pm i\phi}$, $\phi \neq \pi, 2\pi$, implying that any initial deviation will simply rotate around the fixed point. The points of marginal stability are when the eigenvalues are ± 1 ; and by the continuity of the map, M_1 must pass through marginal stability in order for the orbit to go unstable. Equivalently, if $|Tr[M_1]|$ is less than two the orbit is stable, if greater than two it is unstable, and when $|Tr[M_1]| = 2$ it is marginally stable. There are additional general constraints. As already noted, new orbits must appear in stable-unstable pairs in what are called *tangent bifurcations* (TB). Exactly at the point of TB the orbits are marginally stable with $Tr[M_1] = 2$, before the stable one moves to $Tr[M_1] < 2$ and the unstable one moves to $Tr[M_1] > 2$. Conversely, the other value for marginal stability, $Tr[M_1] = -2$ corresponds to forward or backwards period-doubling bifurcations of the PO. These will be of great interest below as they are closely-related to the peak-doubling transitions seen in the magnetotunneling experiments.

We can obtain the monodromy (stability) matrix for all one-bounce orbits analytically, but again will first extract its qualitative features by continuity arguments. As just noted, for infinitesimal tilt angle the TO is deformed into the $(1)^{+k}$ orbit in the interval $2\pi k < \beta < 2\pi(k+1)$. Therefore the stability properties of the $(1)^{+k}$ orbits must be continuous with those of the TO in these intervals. For the case of the TO of the untilted system the monodromy matrix is trivial. The TO has $v_x = v_y = 0$, therefore a small increment of velocity in the $x - y$ plane leaves the time interval between collisions unchanged to linear order in δv . Thus each iteration of the monodromy matrix is just rotation of this deviation vector by the angle $\omega_c T$, leading to $Tr[M_1] = 2\cos\omega_c T$. Therefore the TO is stable at all values of β except such that $\omega_c T = m\pi$; $m = 1, 2, 3, \dots$. It follows by continuity that the orbits $(1)^{+k}$ will be stable everywhere in the interval $2\pi k < \beta < 2\pi(k+1)$ except in infinitesimal intervals around these values.

The lowest value at which instability can occur is $\beta = 2\pi k$, but this is precisely the point of tangent bifurcation where the $(1)^{+k}$ and $(1)^{-k}$ orbits are born. Since $(1)^{+k}$ must evolve immediately into the analog of the (stable) TO above threshold, it must become the stable member of the pair immediately after the TB; whereas the $(1)^{-k}$ orbit must then be unstable. This is allowed by continuity since the $(1)^{-k}$ immediately evolves into the analog of the HO's, which are marginally stable for all β and can hence become unstable under infinitesimal perturbation.

Near the midway points of the relevant interval, $\beta = 2\pi(k + 1/2)$, the $(1)^{+k}$ orbit can again go unstable, but it must immediately restabilize by continuity for higher values of β in this interval. We find that in fact all $(1)^{+k}$ do go unstable by period-doubling bifurcation (PDB) near this value, and for sufficiently small tilt angles they all restabilize by inverse PDB at slightly higher β .

As β increases past the value $2\pi(k + 1)$ the $(1)^{+k}$ orbit ceases to play the role of the TO (which is taken over by the $(1)^{+(k+1)}$ orbit) and continuity alone does not determine its stability. However from the effective map arguments of subsection II.B we know that at $\beta \geq 1/\theta$ the system undergoes the KAM transition to global chaos, and we therefore expect all existing periodic orbits to finally go unstable for sufficiently high values of β . In other words, for any non-zero θ the continuity argument will fail for sufficiently high $\beta \sim 1/\theta$ and new orbits can appear which have no analog in the untilted system. In fact this second destabilization of the $(1)^{+k}$ orbit occurs by a PDB which creates a period-two orbit with no analog in the untilted system, as we shall see below.

As θ becomes of order unity, the β value as which global chaos sets in becomes also of order unity and we do not expect any of the $(1)^{+k}$ orbits to remain stable over a large interval. As already shown above, however, we can prove from Eq. (40) that a $(1)^{k\pm}$ pair is born by tangent bifurcation in each interval. Thus the $(1)^{+k}$ must be stable over some small interval for arbitrarily large β , but it need not restabilize after its first PDB. (Note that the effective map argument only predicts global chaos in the sense of no remaining KAM tori for large β ; it does not prove that no stable periodic orbits can exist, and indeed we have proved the converse: stable one-bounce orbits do exist above any finite value of β). To interpolate continuously between the limits of infinitesimal and large θ the second PDB moves continuously to lower β values until it eliminates the inverse PDB and hence eliminates the restabilization of the $(1)^{+k}$ PO.

To make all of these features explicit and quantitative we have derived the monodromy matrix for all single-bounce orbits. The straightforward but tedious calculation is sketched in Appendix A. We find:

$$\begin{aligned} \text{Tr}(M_1) &= 4 \cos^4(\theta) [\tan^2(\theta) + (\omega_c T/2) \cot(\omega_c T/2)] \\ &\quad \times \{ \tan^2(\theta) + \sin(\omega_c T)/(\omega_c T) \} - 2 \end{aligned} \quad (44)$$

This equation describes precisely the stability properties of the one-bounce orbits sketched above. First, every time a new pair of roots of Eq. (40) appear with increasing β , $\text{Tr}(M_1) = +2$ corresponding to a tangent bifurcation, as discussed. As β increases from this threshold one root (describing the $(1)^{-(k)}$ PO) becomes increasingly unstable with $\text{Tr}(M_1) \rightarrow +\infty$. In contrast, the other root corresponding to the $(1)^{+k}$ orbit initially becomes stable ($\text{Tr}(M_1) < 2$) and remains so for a finite interval before going unstable at $\text{Tr}(M_1) = -2$ by PDB. For sufficiently small θ , $\text{Tr}(M_1)$ will pass through the value -2 twice more before tending to $-\infty$, corresponding to the restabilization and subsequent destabilization of the $(1)^{+k}$ predicted by the continuity arguments above. As θ increases for any fixed interval k eventually a critical angle is reached at which this restabilization ceases, just as predicted. The behavior of the $\text{Tr}(M_1)$ for $(1)^{\pm k}$ orbits with $k = 0, 1, 2$ is shown in Fig. 7. Since increasing k corresponds to larger β , the critical angle becomes smaller as k increases. The intervals of restabilization of the $(1)^{+k}$ orbits are shown in Fig. 8 terminating at the critical angles θ_k^\dagger . The most experimentally relevant interval is $k = 0$, for which Eq. (44) predicts a critical angle of $\theta_0 \simeq 25^\circ$, very close to the value at which the peak-doubling regions merge in the data of ref.¹¹. We will later show how the occurrence of this critical angle relates to the size and evolution of the peak-doubling regions in the data.

Quantitative results for the β values at which the PDBs occur and for the critical angle are easily obtained from Eq. (44) for the monodromy matrix. Equation (44) can be written as

$$\begin{aligned} \text{Tr}(M_1) + 2 &= R(\theta, \omega_c T) \\ &= 4 \cos^4(\theta) R_1(\theta, \omega_c T) R_2(\theta, \omega_c T) \end{aligned} \quad (45)$$

where the zeros of the function $R(\theta, \omega_c T)$ (known as the *residue*) give the parameter values for all PDBs. It is easily seen from Eq. (44) that factor R_1 has exactly one root in each interval k , whereas the factor R_2 has either two or zero roots in each interval, corresponding to the presence or absence of the restabilization. The set of transcendental equations which determine the roots of R_1, R_2 and hence the bifurcations points and critical angles are summarized in Appendix B.

The existence and stability properties of the one-bounce orbits as predicted by Eqs. (40),(44) are confirmed by the numerically-generated SOS and indeed reveal the underlying pattern to the complex behavior seen in the SOS. The period-doubling bifurcations of the one-bounce orbits are of particular interest because they are closely-related to the peak-doubling phenomena observed experimentally. We will elucidate this behavior in the next section on period-two orbits.

D. Two-bounce orbits

1. Qualitative description, $\beta\theta \ll 1$

For $\theta = 0$ all two-bounce periodic orbits occur in helical families satisfying the resonance condition :

$$(2k+1)\omega_L = 2\omega_c \quad k = 0, 1, 2, \dots \quad (46)$$

Only odd integers appear in the resonance condition since even integers yield orbits equivalent to the period-one helical family. As follows from Eqs. (33) and (46), the periods of the two-bounce helical orbits are given by

$$T = (2k+1) \frac{2\pi}{\omega_c}. \quad (47)$$

Therefore, just as for the one-bounce helical orbits, the resonant tori corresponding to the two-bounce orbits can only appear above a threshold value of β at which the longitudinal period becomes long enough to satisfy Eq. (47). At this threshold the two-bounce orbits are indistinguishable from the second repetition of the traversing orbit. Thus the thresholds $\beta_c^{(2)}$ are given by the condition $2T_{\text{TO}} = (2k+1)T_c$, which gives

$$\beta_c^{(2)} = \pi(2k+1). \quad (48)$$

Once emerged, the period-2 resonant tori remain in the phase space of the system for arbitrary large value of β , simply moving towards the periphery of the surface of section as β increases.

Again, as for the helical one-bounce periodic orbits, when the magnetic field is tilted, the resonant tori of the two-bounce orbits are destroyed and replaced by an integer number of pairs of stable and unstable two-bounce periodic orbits. By continuity, these orbits must appear in the vicinity of the $(1)^{+k}$ traversing orbits (which are now playing the role of the TO) and near the values $\beta \approx \pi(2k+1)$ at which the two-bounce tori appear. Our previous analysis for small tilt angles has already identified one direct and one inverse period-doubling bifurcation of the $(1)^{+k}$ near these values of β (see Fig. 7). In a direct PDB a stable one-bounce PO becomes unstable while generating a stable two-bounce PO in its neighborhood; in an inverse PDB an unstable one-bounce PO becomes stable while creating an unstable two-bounce PO in its neighborhood. Hence for consistency we conclude that exactly one pair of two-bounce PO's is created from each two-bounce family for infinitesimal tilt angle. Furthermore, one of these arises from the direct PDB and is therefore stable, whereas the other arises from the inverse PDB and is unstable. (For infinitesimal tilt angle the interval $\Delta\beta$ between these two PDBs is also infinitesimal and they are created at the same "time" in agreement with the Poincaré-Birkhoff theorem; for any finite angle they are separated by some finite interval in β).

It follows that there must be exactly two orbits from each helical family which are continuously deformed into the stable and unstable two-bounce POs created at these two PDBs. It is easy to identify one of the two in analogy to our earlier reasoning. There is only one two-bounce PO in each helical family for which both of its two collisions with the barrier occur with $v_y = 0$ (see Fig. 9). This orbit can be continuously deformed into a non-mixing two-bounce orbit which will become degenerate with the non-mixing $(1)^{+k}$ at the PDB - see Fig. 10a. However, unlike the case for one-bounce HOs, there is no second orbit with fixed points at $v_y = 0$ which can evolve into the second two-bounce orbit which we know must be created. Hence this second orbit at $\theta \neq 0$ must be mixing; i.e. it must generate fixed points with non-zero v_y . Thus it must be obtained by a deformation of one of the two-bounce orbits in the helical torus with finite values of v_y at collision.

To identify which orbit this is we must consider the general properties of mixing two-bounce orbits in this system. We have noted above that due to time-reversal symmetry the SOS has to be symmetric under the transformation $v_y \rightarrow -v_y$. It is obvious that a two-bounce orbit with the same value of v_x at each collision will generate two fixed points in the SOS which satisfy this reflection symmetry. Note that since $v_x \propto y$, such a mixing period-two orbit strikes the barrier at the same value of y in each collision. We will refer to such orbits as self-retracing since they retrace themselves in $y-z$ projection. All self-retracing two-bounce orbits are mixing. However there exist non-self-retracing two-bounce mixing orbits. These must collide with different values of v_x at each collision, but still satisfy the required reflection symmetry of the SOS in a more subtle manner. In such an orbit the values of v_x at collision differ *for any one sense of traversal*, but traversing the orbit in the opposite sense generates two additional fixed points which restore the $v_y \rightarrow -v_y$ symmetry of the SOS which has four fixed points for such orbits. Such an orbit is shown in Fig. 10c, and analogous orbits exist for higher-bounce POs as well. We will discuss their origin later.

However, these non-self-retracing two-bounce orbits cannot be created at a PDB of a one-bounce orbit (period-one fixed point) since such a PDB cannot create more than two new fixed points^{27,28}. Therefore the second, mixing orbit we seek for $\theta \neq 0$ must be a self-retracing orbit, i.e. it must have the same value of v_x at each of its two collisions with

non-zero v_y - see Fig. 10b. The only orbit in the $\theta = 0$ helical family with this property is the one which collides with the barrier with $v_x = 0$ at each collision (see Fig. 9). Hence by continuity it is this orbit which must be continuously deformed to give the mixing orbit which must, by the Poincaré-Birkhoff theorem, exist for infinitesimal tilt angle. Intuitively, the PDB of the $(1)^{+k}$ orbit to the non-mixing two-bounce orbit corresponds to splitting the $(1)^{+k}$ at the point of collision, whereas the PDB corresponding to the mixing one corresponds to splitting the $(1)^{+k}$ at the point furthest away from the collision (see Table I).

Since lack of mixing at collision should enhance the stability of an orbit for given β, θ , we may expect that the non-mixing two-bounce orbit is born stable in the direct PDB and the mixing one is born unstable at the inverse PDB which occurs at a slightly higher value of β . This conjecture is confirmed by our analytic calculations below. In accord with our earlier notation we will label this pair of two-bounce orbits, which must exist in each interval by continuity, as:

$$(2)^{\pm k} \tag{49}$$

where the sign “+” corresponds to the orbit with the longer period as before. Note that the stable non-mixing orbit then will be the $(2)^{-k}$ and the unstable mixing orbit will be the $(2)^{+k}$ (one should not then interpret +, - as stable, unstable). For simplicity we drop the interval index k below. The same scenario occurs in each interval, just at smaller θ as k is increased.

2. Qualitative description, $\beta\theta \sim 1$

Up to now we have focused on the limit of small $\beta\theta$ where each orbit must by continuity have an analog for $\theta = 0$. Unlike single-bounce orbits in the tilted well, there will exist orbits with two or more bounces which have no analogs in the integrable case. In fact we have already shown above (see Fig. Figs. 7, 8) that after restabilizing by inverse PDB the $(1)^+$ orbit must eventually go unstable by a third PDB which must give rise to a stable two-bounce orbit with no analog in the untilted system. We denote these new orbits as $(2)^*$; one such orbit must exist for each $(1)^+$ orbit although for small tilt angle they will not appear until values of $\beta \sim 1/\theta$.

Will the $(2)^*$ orbits be mixing or non-mixing? One can also decide this by reference to our stability analysis of the $(1)^+$ orbit (see Fig. 7 above). As we showed, for each $(1)^+$ orbit, as θ is increased to a critical value, the second and third PDBs move closer together and finally merge, after which no restabilization of the $(1)^+$ orbit occurs. But the second PDB is associated with the mixing $(2)^+$ orbit; if it merges with the $(2)^*$ orbit when the second and third PDB coincide, then $(2)^*$ orbits must also be of the same symmetry, i.e. mixing.

What happens to the $(2)^+, (2)^*$ orbits for tilt angles above θ_k ? On the one hand above θ_k they cannot be created by PDBs of the $(1)^+$ orbit, since we have shown that it never restabilizes. On the other hand, these two periodic orbits cannot cease to exist suddenly, since they exist for an infinite interval above the threshold for PDB and the orbit far from threshold is negligibly perturbed by a small increase in tilt angle. The resolution of this apparent paradox is that above θ_k the two orbits are created by a tangent bifurcation in a region of the SOS and at a value of β very close to that at which the PDBs occur below θ_k . The detailed description of the transition from the PDB scenario to the TB scenario is sketched in Fig. 11 and described in the caption. In contrast, nothing qualitatively new happens to the behavior of the initially stable $(2)^-$ as θ is increased beyond θ_k ; its interval of stability just shrinks continuously.

So for *all* θ we are able to locate all two-bounce orbits which are related originally to the one-bounce $(1)^{+k}$ orbit, and to describe their evolution qualitatively. There are exactly three such orbits associated with each $(1)^+$ orbit: the $(2)^-$ which is initially stable and non-mixing, the $(2)^+$ which is initially unstable and mixing, and the $(2)^*$ which is initially stable and mixing.

The last point to understand is the evolution of these orbits with increasing β once they are created. Since these orbits exist for all β above threshold at $\theta = 0$, we expect the same behavior for nonzero θ . However, as both the $(2)^-$ and $(2)^*$ orbits are initially stable, we expect them both to become unstable as $\beta \rightarrow \infty$. It turns out that the $(2)^-$ orbit goes unstable as the second stage of an infinite period-doubling transition to chaos. The $(2)^*$ on the other hand follows a more complex route to its final unstable form. As the parameter β is increased, the orbit $(2)^*$ goes unstable via a period-doubling bifurcation, but soon restabilizes and finally goes unstable via a *pitchfork* bifurcation. In such bifurcation a new stable (mixing) orbit is created with a period identical to that of the orbit which has gone unstable. In this case the new orbit is precisely of the non-self-retracing type shown in Fig. (10c) and described above. Thus this one new two-bounce orbit creates four fixed points in the SOS and satisfies the required conservation of the Poincaré index. From the generic properties of 2D conservative maps it can be shown that such orbits can *only* be created in these pitchfork bifurcations. Although it is interesting to note the origin of the non-self-retracing two-bounce orbits, they are of a little importance for the description of the experimental tunneling spectra, since generally the pitchfork

bifurcations appear at relatively high values of β , as we will show in the quantitative description of the two-bounce orbits in the next subsection.

In principle completely new two-bounce orbits can also arise by tangent bifurcations at sufficiently large tilt angles and values of β , in fact no visible islands due to such orbits are seen in the SOS for any tilt angles of interest in the range of β values which are accessible experimentally. Thus for understanding the experimentally observed peak-doubling regions only the three two-bounce orbits $(2)^-, (2)^+, (2)^*$ for the intervals $k = 0, 1$ are most relevant. Their properties are summarized in table I. These orbits, once their generalization to the double-barrier model is understood, will be sufficient to explain the peak-doubling data of references^{9,11}.

We now give an analytical description of the periods and stability of the two-bounce orbits identified above.

3. Quantitative theory : Non-mixing two-bounce orbits

The derivation of the periods of the non-mixing two-bounce orbits can be performed using the same technique developed in the analysis of the single-bounce orbits. In the drift frame introduced in section III.B.2 the orbit consists of two identical and overlapping arcs of a circle of angular size $\omega_c T > \pi$ with their endpoints displaced by $v_D T/2$. Imposing the non-mixing condition at the two collisions determines T . Conservation of energy is not required to fix the period and this leads to the striking result that the period is independent of energy (this is the only relevant orbit with this property). This calculation, the details of which are given in the Appendix D, yields :

$$\frac{\omega_c T}{4} \cot \frac{\omega_c T}{4} = -\tan^2 \theta \quad (50)$$

The k -th positive root of this equation gives the value of the period of the $(2)^{+(k)}$ orbit. Note that the solutions T do not depend on β . This is the only orbit with this property.

We have also calculated the stability properties of these orbits by evaluating the trace of the corresponding monodromy matrix using the general expressions developed in the Appendix C. This straightforward but tedious derivation is given in Appendix E. In fig. 12 we plot $\text{Tr}(M)$. In agreement with our qualitative analysis, $\text{Tr}(M)$ is a monotonically decreasing function of β , so that the initially stable two-bounce non-mixing orbit destabilizes by a period-doubling bifurcation and then remains unstable for all β . The 4-bounce periodic orbit, which is born in this bifurcation, will in turn bifurcate, producing an infinite series of period-doubling bifurcations of the same type as the period-doubling sequence in the quadratic DeVogelaere map^{29,22}. However, since the periodic orbits of this sequence have long periods and relatively large cyclotron energy, they are of a little importance for the description of the tunneling spectra in the tilted well, and will not be discussed in the present paper.

4. Mixing period-2 orbits

Due to nonzero energy exchange at the points of collision the analytical description of a general mixing two-bounce periodic orbit will be very complicated. However, as we pointed out before, the most important two-bounce mixing orbits are self-retracing (in $y-z$ projection) leading to the symmetry property that v_x is the same at both collisions. Imposing this condition simplifies the analytical treatment. For each of these orbits, the electron collides with the barrier twice at the same point with exactly the same *absolute values* of the velocity components v_x, v_y, v_z . Using this property, one can show (see Appendix F), that the periods T of the two-bounce self-retracing orbits must satisfy the following system of coupled transcendental equations :

$$\begin{cases} \frac{\sin\left(\frac{\omega_c T}{2}\right)}{\frac{\omega_c T}{2}} = -\tan^2 \theta \frac{\sin\left(\frac{\omega_c \delta T}{2}\right)}{\frac{\omega_c \delta T}{2}} & (51a) \\ \left(\frac{\beta}{2}\right)^2 = \sin^2 \theta \left(1 - \frac{\frac{\omega_c T}{2} (\cos(\frac{\omega_c T}{2}) + \cos(\frac{\omega_c \delta T}{2}))}{2 \sin(\frac{\omega_c T}{2})}\right)^2 + \left(\frac{\omega_c T}{4}\right)^2 + \cot^2 \theta \left(\frac{\omega_c \delta T}{4}\right)^2 & (51b) \end{cases}$$

where $\delta T < T$ is the difference of the time intervals between successive collisions t_1 and t_2 (see Appendix F). This system of two equations determines the periods of all of the self-retracing two-bounce orbits as functions of β and the tilt angle.

Although the equations (51a), (51b) look quite complicated, they allow a further analysis. Assume at least one solution exists for some fixed value of T and find the corresponding value(s) of the time difference δT from equation

(51a) which depend explicitly only on T, θ (but only implicitly on β). As an equation for δT at fixed T and θ , this relation can have multiple solutions $\delta T = \delta T_n$:

$$\delta T_n = 2\wp_n \left(-\cot^2 \theta \frac{\sin \left(\frac{\omega_c T}{2} \right)}{\frac{\omega_c T}{2}} \right), \quad \delta T_n < T \quad (51)$$

where the function $\wp_n(x)$ was defined in Appendix B (see Eq. (B5)) and the maximal value n depends on the value of T, θ . If T is not a solution of the system for any β , Eq. (8) will have no roots with $\delta T < T$. One knows (from the calculation of the stability matrix for the single-bounce orbits) the exact values of T at which the $(2)^{+k}, (2)^{*k}$ orbit are born by PDB and inverse PDB of the $(1)^{+k}$. Hence we can find the starting value of T for each $(2)^{+}, (2)^{*k}$ orbit and follow it continuously as β increases. Each root δT_n when inserted into Eq. (51b) yields a solution “branch” $\beta_n(T)$ for a two-bounce orbit.

There does not however need to be exactly one self-retracing two-bounce orbit for each solution branch $\beta_n(T)$. If the period of such an orbit is a non-monotonic function of β then the same orbit will give rise to multiple solution branches which must merge at the extrema of $T(\beta)$. One can show that there can be no more than one extremum at finite β for $T(\beta)$, thus each orbit will be described by either one or two such branches. Conversely, one solution $\beta_n(T)$ can be non-monotonic in T , hence it must describe two different two-bounce orbits with different periods at the same value of β . With care, *any* two-bounce self-retracing orbit can be obtained by this approach. This procedure yields the plots of the periods for the $(2)^{+0}, (2)^{*0}$ orbits shown in Fig. 13. Note that unlike the non-mixing $(2)^{-k}$ orbits, the periods of the mixing orbits depend on β .

In fact for small tilt angles the period of the $(2)^{+k}$ orbit is a monotonically decreasing function of β and there is only the $n = 1$ solution branch to consider. In this case we can expand Equations (7),(8) for $\beta\theta \ll 1$ and obtain an explicit formula for the periods of these orbits:

$$\omega_c T = \pi (1 + 2k) \left(1 + \theta^2 + \frac{10 + \pi^2 - 6\beta^2}{6} \theta^2 \right) + O(\theta^6). \quad (52)$$

Although the $(2)^{*}$ orbits have the same topology as the $(2)^{+}$ (and at large θ they are born together in a tangent bifurcation), they have no analogs in the untilted system so their periods cannot be obtained from such an expansion. The quantitative analysis of Eqs. (51a), (51b) confirms the transition scenario between PDB and TB for the $(2)^{+}, (2)^{*}$ for large tilt angles described in Fig. 11.

Once the values of T and δT are known from the Eqs. (51a),(51b), the components of the velocity at the points of collisions can be obtained from (F4), and one can calculate the monodromy matrix for each such orbit using (C4) and (C3). In Fig. 14 we show the behavior of the trace of the monodromy matrix for $(2)^{+}$ and $(2)^{*}$ orbits. As argued above, one finds that the $(2)^{+}$ orbits are unstable for all β , whereas the $(2)^{*}$ orbits which are born stable (since they arise from a direct PDB of the $(1)^{+}$ orbit), and go unstable in the complicated sequence ending with a pitchfork bifurcation which we have described above and in the caption to Fig. 14.

In Table I we summarize the relevant period-1 and period-2 orbits.

E. Three-bounce periodic orbits

The scenario for the three-bounce periodic orbits is similar in many ways to that for the two-bounce orbits just described. When the magnetic field is not tilted all three-bounce periodic orbits belong to resonant tori and correspond to the resonances

$$k\omega_L = 3\omega_c \quad (53)$$

where the integer k is not a multiple of 3. Thus as β increases from zero in the first interval there are two thresholds for the birth of resonant tori. When $\beta = 2\pi/3$ the family of helical orbits which perform 1/3 of a cyclotron rotation per collision with the barrier appears, and at $\beta = 4\pi/3$ the family which makes 2/3 of a rotation per collision appears. As for the two-bounce orbits, the analogous orbits in the higher intervals behave in exactly the same manner qualitatively, and so we focus here on those in the first interval.

When the magnetic field is tilted, the period-3 resonant tori are destroyed and replaced by pairs of stable and unstable three-bounce orbits. Here some important differences from the two-bounce orbits enter. First, we cannot have a *single* three-bounce orbit created at some value of β since there is no analog of a period-doubling bifurcation for creating three-bounce orbits. At the threshold for creation of the three-bounce helical families, when they are degenerate with the third repetition of the traversing orbit, the $TrM_1 = -1$ and its stability cannot change. Therefore

period-three orbits must always be created in stable-unstable pairs by tangent bifurcation. Moreover there is generically no constraint that such a tangent bifurcation occur at the fixed point corresponding to a period-one orbit²⁷. In this sense there are no trifurcations in a generic system. When $\theta = 0$ the rotational symmetry of the system does constrain the entire family of three-bounce orbits to appear degenerate with the third repetition of the traversing orbit, but as soon as $\theta \neq 0$ the pair of three-bounce orbits which survive are created away from the period-one fixed point. However, by continuity the tangent bifurcation (TB) which creates this pair must occur near this fixed point and at approximately the same value of β . We infer that for small tilt angles there are at least two TB's in the first interval, each of which creates a stable-unstable pair of three-bounce orbits, at $\beta_1 \approx 2\pi/3, \beta_2 \approx 4\pi/3$. Extending our earlier notation, we will denote these four orbits by $(3)_1^\pm, (3)_2^\pm$.

Which orbits of the resonant tori survive? In this case there is no orbit in the helical family which has all of its collisions with $v_y = 0$; therefore by continuity there can be no three-bounce non-mixing orbits for small tilt angles (and one can easily show that this result holds for any θ). However there are two orbits in each torus which collide with $(v_y)_1 = 0, (v_y)_2 = -(v_y)_3$ corresponding to two possible orientations of the appropriate equilateral triangle along the v_x axis. These two orbits satisfy the required symmetry of the SOS upon tilting, while no others in the torus do. Therefore it is these orbits which survive (slightly distorted due to the tilt, of course).

This conclusion, while correct, must be reconciled with our earlier statement that the two orbits must appear at a tangent bifurcation. At a TB the two orbits are identical, yet the two orbits we have identified correspond to opposite orientations of the equilateral triangle and would not coincide for any finite size of the triangle defining the three fixed points (see Fig. 15). In order to coincide at the TB the unstable member of the pair must actually pass through the single-bounce fixed point at the center of the triangle in what is known as a “touch-and-go” bifurcation²⁷. At this point the unstable three-bounce orbit coincides with the third repetition of the $(1)^+$ orbit, which is no longer isolated and $TrM_1^3 = 2$ (or equivalently $TrM_1 = -1$). So as β is reduced to the threshold for the TB, first the unstable three-bounce orbit shrinks to a point coinciding with the period-one fixed point, and then at even lower β reappears on the other side with the appropriate symmetry to disappear by TB with the stable member of the pair. In fig. 15 we show the surfaces of section just before (a) and soon after (b) the “touch-and-go” bifurcation of the orbits $(3)_1^-$ and $(1)^{+(0)}$. This “touch-and-go” (TAG) bifurcation of the three-bounce orbits occurs over such a small β interval for small tilt angles that it is hard to distinguish from a trifurcation of the $(1)^+$ orbit without careful magnification of the transition, but it is required by continuity and the generic principles of 2D conservative maps. In Fig. 16 we plot the periods of these four three-bounce orbits, $(3)_1^\pm, (3)_2^\pm$, which are related to the resonant tori of the untilted system.

As in the case of the two-bounce orbits, our knowledge of the behavior of the $(1)^+$ orbit allows us to predict that in the first interval there must exist a further (pair) of three-bounce orbits which have no analog in the untilted system. The reason is the following. From Fig. 7, for small tilt angle, we know that the TrM_1 for the $(1)^+$ orbit passes through -1 three times before the $(1)^+$ orbit becomes permanently unstable. Each time $TrM_1 = -1$ there must be a TAG bifurcation, so there must be three such bifurcations. Two of them are associated with the $(3)_1^-, (3)_2^-$ orbits we have already identified and occur near $\beta = 2\pi/3, 4\pi/3$; the third TAG bifurcation must be associated with a third pair of orbits born by TB at large $\beta \sim 1/\theta$. This pair plays a similar role for the three-bounce orbits as does the $(2)^*$ orbit for the two-bounce orbits in each interval, hence we denote them by $(3)_*$.

As θ is increased to order unity, the TAG bifurcation of the $(3)_*$ orbits moves to lower β till it eventually coincides with the TAG bifurcation of the $(3)_2^-$ orbit and the two bifurcations “annihilate”. We know this must occur since TrM_1 ceases passing through -1 the second and third times (see Fig. 7). The TAG resonances relating the orbits to the resonances of the $(1)^+$ orbit no longer exist for higher θ (just as the PDBs of the $2^+, 2^*$ no longer exist above some critical angle), but the orbits do not disappear. Instead, they demonstrate an “exchange of partners” bifurcation, which for higher tilt angles allows them to exist without ever evolving into TAG resonances of the $(1)^+$ - see Fig. 17. Again, just like for the two-bounce orbits, the transformation from the small tilt angle to large tilt angle behavior requires the appearance of auxiliary three-bounce orbits in additional tangent bifurcations to provide a smooth evolution. This scenario is illustrated by the bifurcation diagrams in Fig. 17.

In principle an analytic theory of the periods and stability of these three-bounce orbits is possible, but the system of three coupled transcendental equations which define the period are not easily analyzed. Since we already know the qualitative scenario, we have simply used the symmetry properties of these three-bounce orbits to locate numerically the fixed points and hence find the period and time interval between collisions. These quantities are all we need to use the general formalism for the monodromy matrix developed in Appendix C.

In fig. 18 we show the behavior of the trace of the monodromy matrix for three-bounce orbits $(3)_1^{0\pm}, (3)_2^{0\pm}$ and $(3)_*^{0\pm}$. The stability properties of the three-bounce orbits show a clear analogy with the behavior of two-bounce orbits. The $(3)_1^\pm, (3)_2^\pm$ orbits related to the resonant tori, are either always unstable, or go unstable via period-doubling bifurcations and never regain stability. Whereas the behavior of the new $(3)_*$ is different. As follows from Fig. 18, the initially unstable $(3)_*$ restabilizes via pitchfork bifurcation after its TAG bifurcation with the $(1)^+$ orbit,

before eventually going unstable in a period-doubling bifurcation at higher value of β . The initially stable $(3)_*$ orbit has a monotonically decreasing monodromy and goes unstable via a period-doubling bifurcation. All of these orbits are self-retracing in the sense defined above. At the pitchfork bifurcation of the $(3)_*$ orbit just described, a new three-bounce orbit appears which is non-self-retracing. Thus, as for the two-bounce orbits, orbits of this type only appear after the creation of the self-retracing orbits and hence arise at relatively high β values. Hence they have little effect on the experimental observations and will be disregarded below.

F. Many-bounce orbits

The analysis of period- n ($n > 3$) orbits can be conducted in a similar framework. First, one can identify the periodic orbits, which survived from the resonant tori of the untilted system, and then relate these orbits to the $1:n$ resonances of the single-bounce orbits $(1)^+$. Since for small tilt angles TrM_1 is non-monotonic with β and crosses the stability region three times, the third crossing will always give rise to new orbits which are born at $\beta \sim 1/\theta$ and which have no analogs in the untilted system. As θ is increased these resonances will move to lower β and annihilate with earlier resonances leading to new tangent bifurcations and the “exchange of partners” already understood and observed for the two-bounce and three-bounce orbits. Additional new orbits can be formed both by pitchfork bifurcations of self-retracing orbits and by completely new tangent bifurcations, however such orbits appear to play no role in the first and second interval for experimentally relevant values of β . Moreover, even the n -bounce orbits which *are* related to the resonant tori of the unperturbed system generally have too long periods and/or too much cyclotron energy to be observed in the tunneling spectra. As they introduce no essentially new physics we will not present any detailed treatment of these orbits.

IV. PERIODIC ORBITS IN THE DBM

We now analyze the periodic orbit structure of the double-barrier model (DBM). This model will provide a description of periodic orbits relevant to the experiments of refs.^{9,11}. A crucial point discussed in section IIA above is that in general for a fixed tilt angle the classical dynamics of the DBM depends on two dimensionless parameters: the parameter $\beta = 2v_0B/E$ already used in analyzing the SBM, and the parameter $\gamma = \epsilon_0/eV$ measuring the ratio of the injection energy to the voltage drop. Fortunately, in the experiments this second parameter is roughly constant^{11,20}, $\gamma \approx 1.15 - 1.17$. Therefore the periodic orbit theory (and ultimately the semiclassical tunneling theory) need only be done varying β with γ fixed to the experimental value. We will focus on this case henceforth. In interpreting the results of this section however, it must be borne in mind that β no longer is the product of three independent variables; v_0 and E are related by the condition of constant γ . The magnetic field however is still an independent variable and thus it is easiest to think of increasing β as increasing the magnetic field.

Many of the periodic orbits we will discuss below have been previously identified by Fromhold et al.⁹ or Monteiro and Dando¹⁹. What has not been done is to systematize all the experimentally-relevant orbits and find their intervals of existence and stability. This we attempt to do below.

As previously noted, the periodic orbit theory of the DBM is in many respects similar to that of the SBM, but there are three significant differences. First, orbits can be born or disappear in a manner which violates the generic bifurcation principles for conservative systems since the Poincaré map for the DBM is nonanalytic on the critical boundary of the SOS (the curve separating initial conditions which will reach the emitter barrier from those which will not, cf. section IIC). The novel bifurcations which result (which we call cusp bifurcations) play a crucial role in the behavior of the short periodic orbits in the system. Second, the unperturbed system has a more complicated structure as there can exist two distinct resonant tori corresponding to the same resonance condition $n\omega_c = k\omega_L$, one corresponding to helical orbits which do reach the emitter, and the other corresponding to helical orbits which do not. Third, once the field is tilted, orbits which are periodic after n bounces with the collector may collide with the emitter any number of times from zero to n . As a function of β such orbits can change their connectivity with the emitter. In fact it can be shown that any orbit which does reach the emitter can only exist for a finite interval of β . We will now explain these important points in detail.

A. Periodic orbits at $\theta = 0$

First let us assume there exists an (n, k) resonant torus of the unperturbed system which does not make any collisions with the emitter barrier for a given value of β . At $\theta = 0$ longitudinal and cyclotron energy decouple and, as

the emitter barrier plays no role, the frequency of the longitudinal motion must be given by Eq. (31) for the SBM. Using this formula for ω_L , the resonance condition $n\omega_c = k\omega_L$ leads to a condition on β :

$$\beta = 2\pi \frac{k}{n} \sqrt{\varepsilon_0/\varepsilon_L} \quad (54)$$

Exactly as for the SBM, if such an orbit exists for one value of the longitudinal energy ε_L , another such family will exist at the same total energy but with smaller longitudinal energy, since adding to the cyclotron energy does not change ω_c . From Eq. (54) the new family with smaller ε_L will exist at higher β as the magnetic field will have to be increased to keep it in resonance. As β increases for such families the orbits will just move further away from the emitter but will always exist above the threshold value defined by the maximum value of ε_L . Unlike the SBM however, the maximum allowed value is not ε_0 , since before all the energy is put into longitudinal motion the orbit begins to hit the emitter barrier; this happens of course when $\varepsilon_L = eV \equiv \varepsilon_0/\gamma$. We will call orbits which don't reach the emitter "collector" orbits and those which do "emitter" orbits. Our argument implies that there exist families of (n, k) helical collector orbits for all β above the threshold $\beta_c = 2\pi(k/n)\sqrt{\gamma}$. These orbits are identical to those in the SBM and the only change introduced by the emitter barrier is that the threshold for their creation has been raised by a factor $\sqrt{\gamma} = \sqrt{\varepsilon_0/eV}$.

Now assume there exists an (n, k) family for a given value of β which *does* reach the emitter barrier. The longitudinal frequency of any such orbit is easily calculated to be:

$$\omega_L = \frac{2\pi\omega_c}{\beta} \sqrt{\frac{\varepsilon_0}{\varepsilon_L}} \left(1 - \sqrt{1 - \frac{eV}{\varepsilon_L}}\right)^{-1}. \quad (55)$$

Note the crucial difference here from Eq. (31); for the emitter orbits ω_L is an *increasing* function of ε_L . Imposing the resonance condition then leads to the relation:

$$\beta = 2\pi \frac{k}{n} \sqrt{\frac{\varepsilon_0}{\varepsilon_L}} \left(1 - \sqrt{1 - \frac{\varepsilon_0}{\gamma\varepsilon_L}}\right)^{-1}, \quad (56)$$

which implies that β is also an increasing function of ε_L in the interval of interest. For emitter orbits the *smallest* value that ε_L can take is eV , otherwise they will cease to reach the emitter, and for this value $\beta = \beta_c$. Therefore, like the collector families, the emitter (n, k) families also do not exist below β_c . They are born when β increases through β_c at the critical boundary simultaneously with the collector family corresponding to the same values of (n, k) (see Fig. 19).

When created, the emitter families have non-zero cyclotron energy (see Fig. 19) and can be continuously deformed by transferring cyclotron energy to longitudinal energy, moving the family to higher values of β for fixed total energy. This can only continue until $\varepsilon_L = \varepsilon_0$ and all of the energy is longitudinal, yielding now a *maximum* allowed value of β ,

$$\beta_{TO} = \beta_c[\sqrt{\gamma} + \sqrt{\gamma - 1}]. \quad (57)$$

We denote this value by β_{TO} because at this value the (n, k) helical emitter family has collapsed to the traversing orbit (which exists and always reaches the emitter for $\gamma > 1$). Thus the scenario at $\theta = 0$ is that two (n, k) families are born at the critical boundary each time β increases through $\beta_c(n, k)$. The collector family moves outwards in the SOS and exists for all $\beta > \beta_c$, whereas the emitter family moves inwards in the SOS and annihilates with the TO at $\beta_{TO}(n, k)$ (see Fig. 19). The consequence is that each emitter family lives for only a finite interval, $\beta_c < \beta < \beta_{TO}$. By continuity all the emitter periodic orbits which evolve from these emitter tori (in a manner similar to the SBM) will also live in a finite interval given approximately by this inequality for small tilt angle. To our knowledge this property of the system has not been demonstrated in the previous literature. As only the emitter orbits will play a major role in the semiclassical theory of the tunneling spectrum (collector orbits make exponentially small contributions), the point is of some significance.

It follows from this argument that as β increases the collector families evolve by transferring longitudinal energy to cyclotron energy in the manner familiar from the SBM, whereas as β increases the new emitter orbits *give up* cyclotron energy to remain in resonance. To understand this less familiar behavior recall that increasing β may be regarded as increasing B with all other parameters fixed. As B increases the cyclotron frequency increases and the longitudinal frequency will need to increase to maintain the resonance condition. As noted already, unlike the collector orbits, for emitter orbits the longitudinal frequency increases with ε_L . The reason for this is that as ε_L increases the electron traverses the fixed distance to the emitter faster and is more rapidly returned to the collector. We will see below that the consequence of this reversal of the dependence on ε_L means that all bifurcations of emitter orbits in the DBM happen in the reverse direction (as a function of β) from the bifurcations of the corresponding orbits in the SBM.

B. Period-one orbits in the DBM

1. Continuity argument

We now analyze the period-one POs of the DBM for $\theta \neq 0$. Here we mean period-one orbits with respect to iteration of the Poincaré map defined at the collector of the DBM, i.e. the orbits must collide with the collector only once before retracing. For zero tilt angle these orbits will be of three types. 1) The collector orbits corresponding to the $n = 1, k = 1, 2, \dots$ resonances, which do not collide with the emitter. 2) The emitter orbits corresponding to the $n = 1, k = 1, 2, \dots$ resonances which do reach the emitter. 3) The traversing orbit, which has zero cyclotron energy and which hence must reach the emitter for $\gamma > 1$. The TO has the period:

$$T_{\text{TO}} = \frac{\beta}{\omega_c} \left(1 - \sqrt{1 - \frac{1}{\gamma}} \right). \quad (58)$$

As in the SBM, The helical families of orbits will generate pairs of POs when $\theta \neq 0$ and by continuity, for infinitesimal tilt angle, the orbits arising from emitter families will be emitter orbits and those arising from collector families will be collector orbits.

We must now classify periodic orbits not only by the number of bounces with the collector, but also by the number of bounces with the emitter. We introduce the generalization of our earlier notation

$$\begin{aligned} (1, 1)^{\pm k} & \quad \text{for the emitter orbits} \\ (0, 1)^{\pm k} & \quad \text{for the collector orbits} \end{aligned}$$

where the first number in the parentheses denotes the number of collisions with the emitter barrier and the second the number with the collector barrier per period. k is the integer defining the interval as in the SBM; the period of an order k single-bounce orbit is between kT_c and $(k+1)T_c$. This notation is used in Fig. 21.

For infinitesimal tilt angle and $\beta < \beta_c \simeq 2\pi$ there will exist only one single-bounce orbit, the analog of the TO, which we denote as $(1, 1)^{+0}$. This orbit differs only infinitesimally from a straight line when $\beta \rightarrow 0$, but gains more cyclotron energy as β is increased, just as in the SBM.

As β is increased to $\approx \beta_c$ four new single-bounce orbits arise in an infinitesimal interval; these are the two non-mixing orbits from each of the collector and emitter $n = 1, k = 1$ families. Due to the breaking of the symmetry between these two orbits in each family, they are created pairwise at slightly different β values and with slightly different periods. However the corresponding collector and emitter orbits are still born at the same β value in a cusp bifurcation. The two orbits which survive from the single-bounce collector orbit families are identical to those already discussed in the SBM, they are denoted by $(0, 1)^{0+}$ and $(0, 1)^{-1}$, because they are now born in different intervals (see Fig. 21) of the period (the period of the orbit $(0, 1)^{+0}$ is greater than T_c , while the period of $(0, 1)^{-1}$ is less than T_c). The single-bounce collector orbits must be non-mixing by the simple argument given in discussing the SBM. The single-bounce emitter orbits collide twice in each period and so it is less obvious that they must be non-mixing in their collision with the collector barrier; however it can be rigorously proved that this must be the case. Therefore, again our continuity arguments implies that only the two emitter orbits with $v_y = 0, v_x = \pm v_c$ will survive. The one with period shifted slightly down from T_c will be denoted $(1, 1)^{-0}$; the one with period shifted up will be denoted $(1, 1)^{+1}$.

Above β_c in the first interval there now exist three single bounce orbits, the $(0, 1)^{+0}$ orbit which doesn't reach the emitter, the $(1, 1)^{-0}$ "helical" emitter orbit and the $(1, 1)^{+0}$ "traversing orbit", which has the shortest period of the three. As in the SBM, for $\theta \neq 0$ there is no qualitative difference between traversing orbits and helical orbits, since both must have non-zero cyclotron energy. As β increases to $\approx \beta_{\text{TO}}$ (see Eq. (57), the helical $(1, 1)^{-0}$ orbits loses cyclotron energy (as would the corresponding orbits at $\theta = 0$ discussed above) whereas the $(1, 1)^{0+}$ orbit gains cyclotron energy. Eventually the two orbits become degenerate and annihilate in a backwards tangent bifurcation, the analog of the annihilation of the $n = 1, k = 1$ emitter family at $\theta = 0$ (see Fig. 21).

At β larger than the value for this TB the $(1, 1)^{+0}$ orbit does not exist, and this is apparently in contradiction with the behavior of the TO at $\theta = 0$ which survives unscathed through the annihilation of the helical family. Moreover, by continuity, for an infinitesimal tilt angle the analog of the (normally) isolated TO must survive at all but a discrete set of values of β . The resolution of this apparent paradox is that, just as in the SBM, an orbit in the next interval, the $(1, 1)^{+1}$, which is the partner of the $(1, 1)^{-1}$, takes over the role of the TO at this value of β , see Fig. 21. The same scenario repeats then in the $k = 1$ and higher intervals. Note that in this scenario all period-one emitter orbits only survive for a finite interval, being born at some threshold value of β by cusp bifurcation and disappearing at higher β by backwards tangent bifurcation.

The behavior of the single-bounce orbits for larger tilt angle differs in one important respect. It becomes more and more difficult for the $(1, 1)$ orbits to reach the emitter barrier and as a result their intervals of existence in β (which initially fill the entire β axis) shrink monotonically until they go to zero at a critical angle which differs for each interval (see Fig. 22b). The only exception is in the first interval where for sufficiently small β it is always possible to have a $(1, 1)^{+(0)}$ analogous to the TO of the untilted system. The reason the $(1, 1)^{+(0)}$ orbit always exists is that we may regard the limit $\beta \rightarrow 0$ as the limit of vanishing magnetic field, so its tilt can have no effect on the orbit, which does have enough energy to reach the emitter ($\gamma > 1$). However since all other single-bounce orbits require finite β , tilting the field sufficiently for fixed γ can prevent the electron from reaching the emitter. As these intervals shrink the scenario also changes. Instead of the $(1, 1)^{+(k)}$ orbit being created directly by a cusp bifurcation, it is created in a tangent bifurcation as a $(0, 1)^k$ orbit and then evolves at higher β into $(1, 1)^{+(k)}$ orbit. This is the first example of an orbit continuously changing its connectivity with the emitter as a function of β ; these events also play a role in the theory of the two-bounce or three-bounce orbits, as discussed below.

Now we discuss the stability of the single-bounce orbits. Clearly, the collector $(0, 1)^\pm$ orbits have identical stability properties as their SBM counterparts. As for the emitter orbits, their stability can also be understood using qualitative arguments similar to the ones we applied in our SBM analysis. Just as in the SBM, in the DBM for zero tilt angle the traversing orbit is stable for any β and γ except when it's period is either an integer or a half integer multiple of the cyclotron period T_c , when it is marginally stable. When the period takes the values $T = kT_c$ the corresponding value of β is $\beta = \beta_{\text{TO}}(1, k)$; when $T = (k + \frac{1}{2})T_c$ the corresponding β values are $\beta = \beta_{\text{ms}}(k) \equiv (1 + \frac{1}{2k})\beta_{\text{TO}}(1, k)$. Therefore, for a small tilt angle the single-bounce orbit which evolved from the TO of the untilted system, can become unstable only near β_{TO} and β_{ms} . In particular, the $(1, 1)^{+(0)}$ orbit is stable for small β , but goes unstable and soon restabilizes near $\beta_{\text{ms}}(0) \equiv \pi/(1 - \sqrt{1 - 1/\gamma})$. As in the SBM, this instability for period $\approx T_c/2$ locates the bifurcations involving the important period-two orbits.

Whereas in the SBM the $(1)^{0+}$ orbit simply evolves into a helical orbit when $\beta \gg 2\pi$, its analog, the $(1, 1)^{0+}$ annihilates with the $(1, 1)^{-(0)}$ orbit near β_{TO} . Due to the general properties of tangent bifurcations, one of these orbits must be stable, while the other must be unstable. Since the $(1, 1)^{+(0)}$ orbit is a deformation of the stable TO it is the stable one just before the TB, while the orbit $(1, 1)^{-(0)}$ is unstable. This is illustrated by the plot of the monodromy matrix for these orbits (Fig. 23).

This $(1, 1)^{-(0)}$ is worth further consideration because it appears at the critical boundary near $\beta = \beta_c$ in a cusp bifurcation together with the collector orbit $(0, 1)^{+(0)}$. A detailed analysis of cusp bifurcations is given in section IV.B.3 below. Here we simply note that due to the singularity in the Poincaré map at the critical boundary the monodromy matrices defining the stability of the new orbits cannot be uniquely defined. We will show that therefore the two orbits need not be born as unstable-stable pairs as in tangent bifurcations (this is why we have introduced the new term cusp bifurcation (CB)). Moreover, one can show that of the two orbits born in a CB, the one with the greater number of collisions with the emitter barrier is necessarily unstable. It follows that the orbit $(1, 1)^{-(0)}$ is unstable immediately after it is born, and turns out to be unstable over its entire interval of existence until it vanishes in the TB with $(1, 1)^{+(0)}$.

These principles allow us to understand the behavior in the next interval as well. The emitter orbit $(1, 1)^{+(1)}$ is also born in a cusp bifurcation with the $(0, 1)^{-(1)}$ collector orbit and hence is born unstable. Initially it plays the role of the “other” emitter helical orbit. However, near $\beta = \beta_{\text{TO}}$ the orbit $(1, 1)^{+(1)}$ loses almost all its cyclotron energy (see Fig. 21) and becomes a recognizable deformation of the TO of the untilted system. By continuity, since away from β_{TO} the TO was stable, the $(1, 1)^{+(1)}$ periodic orbit must restabilize near β_{TO} . Its further evolution is similar to that of the first interval orbit $(1, 1)^{+(0)}$ just discussed. It will bifurcate and then restabilize near $\beta_{\text{ms}}(1)$ and later annihilate with the unstable orbit $(1, 1)^{-(1)}$ in a tangent bifurcation - see Fig. 23. This scenario is repeated in higher intervals although the first interval of stability (below $\beta_{\text{ms}}(1)$) may disappear. We note however, that as long as a $(1, 1)^{+(k)}$ orbit exists in each interval, it must have a region of stability just before it annihilates with the $(1, 1)^{-(k)}$ orbit (which is always unstable), although these intervals will shrink with increasing tilt angle and k .

2. Exact analysis

The derivation of the periods of the period-one emitter orbits in the DBM can be performed using a technique similar to the one employed for the description of period-two non-mixing orbits in the SBM, since both the emitter and collector bounces are non-mixing. The calculation is given in Appendix G and yields the following equation :

$$\beta^2 = \left(\frac{\omega_c T}{2} \right)^2 \left(1 + \frac{\beta^2}{\gamma (\omega_c T)^2} \frac{1 - f(\omega_c T)}{1 - \cos^2 \theta f(\omega_c T)} \right)^2 + 4 \sin^2 \theta f^2(\omega_c T) \left(1 + \frac{\beta^2}{16\gamma f(\omega_c T) (1 - \cos^2 \theta f(\omega_c T))} \right)^2, \quad (59)$$

where \tilde{v}_e^- is the scaled velocity immediately *before* the collision of the electron with the emitter barrier and

$$f(x) = 1 - \frac{x}{4} \cot\left(\frac{x}{4}\right) \quad (60)$$

This is a quadratic equation for β for given T ; it should be solved along with condition (G11), that v_z just before the collision with the emitter is positive, to determine the physically meaningful roots. Solving Eq. (59) together with the condition (G11), one can obtain the dependence $\beta(T)$, which was plotted in Fig. 21 and used to obtain the corresponding bifurcation diagrams. The equation Eq. (23) and the condition (G11) imply that $\beta(T)$ is not monotonic in each interval $[(k-1)T_c < T < kT_c]$, but always has a single maximum. Therefore it describes *two* different $(1,1)$ orbits, which we already identified as the $(1,1)^\pm$ orbits.

Using Eqs. (59) and (G11), one can show, that, as for the period-one orbits in the SBM, for a nonzero tilt angle the period of the $(1,1)$ orbits cannot be equal to integer multiples of the cyclotron period kT_c . Moreover, the period also can not take values too close to kT_c . The width of each of these “forbidden” regions in each interval increases (from zero at $\theta = 0$) with the increase of tilt angle, so that at some critical angle (which depends on the interval number k) the “forbidden” regions originating from $T = (k-1)T_c$ and $T = kT_c$ merge and as already noted, it becomes impossible for the period-one orbits to reach the emitter in this interval of period. When period-one emitter orbits exist in an interval, we can calculate their interval of existence in β from Eqs. (59), (G11). The results for the $(1,1)^{+(0)}$ and $(1,1)^{+(1)}$ orbits are shown in Fig. 22.

One can also calculate the stability properties of the $(1,1)$ orbits as outlined in Appendix H. The results for the trace of the monodromy matrix for different $(1,1)$ orbits are shown in Fig. 23. The qualitative behavior is as discussed above. The key new feature that emerges is an analytic understanding of the cusp bifurcations at the birth of the $(1,1)^-$ and $(0,1)^+$ orbits.

3. Cusp Bifurcations and Connectivity Transitions

First, we note again that *all* relevant emitter orbits are born in cusp bifurcations at the low β side of their existence interval. As shown in Appendix H, the monodromy matrix for the emitter orbit born in a CB involves terms proportional to the inverse of the velocity at the emitter barrier. Since at the cusp bifurcation the emitter velocity goes to zero, the trace of the monodromy matrix of the corresponding orbit will diverge (see Fig. 23). Therefore *all* emitter orbits are extremely unstable just after their appearance in a CB (unless both orbits born in a cusp bifurcation are emitter orbits, in which case the one with greater number of collision with the emitter barrier will be extremely unstable). On the other hand, their companion collector orbits, for β just above the CB no longer “feel” the emitter barrier and must have stability properties as in the SBM, where there is no such divergence for any values of β . Therefore the monodromy matrix for this orbit as β is reduced to the CB value does not tend to infinity but tends toward a finite value (see Fig. 23). Whether this value is in the stable region or not depends on the value of the tilt angle and of γ . For large tilt angle the companion collector orbit is typically unstable just above the CB and *two* unstable orbits are born at the CB, in contrast to the generic behavior at tangent bifurcations.

There is an interesting and important variant on the concept of cusp bifurcation. It is possible that orbits may be born as collector orbits in a TB, and lose cyclotron energy with increasing β until at some higher β they reach the emitter and evolve into emitter orbits. We will refer to these events as *connectivity transitions* since the orbit changes its connectivity to the emitter. However in this case no new orbit is created at the value of β at which the emitter is reached, so this is not a bifurcation point in any sense. Nonetheless, the behavior of the monodromy matrix of this one orbit in the neighborhood of the connectivity transition is similar to that near a CB. The $Tr[M]$ tends to a finite value on the low β side, whereas it diverges at the high β side. For a not too small tilt angle this behavior occurs for the $(0,1)^{+(1)}$ and $(1,1)^{+(1)}$ orbits (see Fig. 23). Interestingly enough, the dynamics does not seem to favor these connectivity changes although they are allowed. For tilt angles larger than a few degrees they are typically replaced by a tangent bifurcation and a new cusp bifurcation which ultimately results in the appearance of an orbit with higher connectivity and the disappearance of one with lower connectivity.

C. Period-two orbits

As in the SBM, the most important set of period-two orbits, for small tilt angles, are those associated with the period-doubling bifurcations of the (deformed) traversing orbit $(1,1)^{+0}$ which occurs near $T \approx T_c/2$ (so that the relevant period-two orbits have $T \approx T_c$). The scenario for their creation and evolution is in many respects similar to the behavior of the helical period-one orbits just described. For $\theta = 0$ a pair of emitter and collector families are

created at the critical boundary at the threshold $\beta_c(n=2, k=1) = \pi\sqrt{\gamma}$. The emitter family loses cyclotron energy with increasing β , moves inward in the SOS and annihilates with the TO at $\beta_{TO}(2,1) = \pi(\gamma + \sqrt{\gamma^2 - \gamma})$. The collector family gains cyclotron energy with increasing β , moves outward, and exists for all β .

When $\theta \neq 0$ two orbits survive from each of the collector and emitter families. These four orbits are born pairwise in two cusp bifurcations involving degenerate collector and emitter orbits, which occur at slightly different values of β . The two collector orbits involved are identical to the mixing $(2)^+$ orbit of the SBM and the non-mixing $(2)^-$ orbit. According to our notation, these collector orbits are denoted as $(0,2)^\pm$. The emitter orbit created in a CB with the non-mixing orbit $(0,2)^-$, which will be referred to as the $(2,2)^-$ orbit (see Fig. 24), has the simplest qualitative behavior and we will discuss it first.

1. $(2,2)^-$ orbits

The period-2 emitter orbit, which appears together with the $(0,2)^-$ orbit, at the cusp bifurcation is degenerate with $(0,2)^-$ and has therefore the same shape. However, as the parameter β is increased, it begins striking the emitter wall with a nonzero velocity. Since at the point of this collision the angle in the (y,z) plane between the electron velocity and the normal to the barrier is *not* 90° , it is a *mixing collision*. In fact it can be shown that any orbit in either the SBM or DBM with more than two total collisions must be partially mixing.

As a result of the mixing collision with the emitter barrier this emitter orbit acquires a cusp at the emitter. Although this $(2,2)^-$ orbit is mixing in a strict sense, it remains non-mixing at the “collector” barrier. Since the magnitude of the velocity is very low at the emitter collision the mixing for this orbit remains very weak.

Whereas the $(0,2)^-$ orbit moves away from the emitter with increasing β in the usual manner, the $(2,2)^-$ orbit transfers more and more energy to longitudinal motion until its “two legs” come together and it becomes degenerate with the $(1,1)^+$ traversing orbit. It is then absorbed in a backwards period-doubling bifurcation, causing a change in the stability of the $(1,1)^+$ orbit.

We have already shown by continuity that the $(1,1)^+$ orbit must destabilize and restabilize in a short interval when its period is $\approx T_c/2$. And we have argued that all its bifurcations must be backwards, since in the DBM orbits are born at lower β in cusp bifurcations. Therefore this backwards PDB of the emitter $(2,2)^-$ orbit corresponds to one of these stability changes. To decide which one, we note that although the $(2,2)^-$ orbit must be born unstable because it is the more connected partner in a cusp bifurcation, it should typically be more stable than other period-two orbits which are mixing at the collector, when the velocity is large. Thus, we expect it to restabilize at higher β and therefore to restabilize the $(1,1)^+$ orbit when the $(2,2)^-$ orbit is absorbed as a stable period-two orbit in the backwards PDB (see Fig. 26). The exact calculation of the monodromy matrix (see Appendix H for the details) confirms this scenario - see Fig. 27. Furthermore, increasing the tilt angle does not change the scenario for the $(2,2)^-$ orbit, it only reduces its interval of existence. This orbit is relevant in the first peak-doubling region observed at small tilt angles in the data of Muller et al.¹¹.

2. $(1,2)$ and $(2,2)^+$ orbits

As just noted above, a collector orbit identical to the mixing $(2)^+$ orbit of the SBM (the $(0,2)^+$ orbit) is also created in a cusp bifurcation with an emitter orbit which must have similar morphology. The simplest scenario would have this emitter orbit evolving exactly as did the $(2,2)^-$ orbit, losing cyclotron energy until it is absorbed by the $(1,1)^+$ in the other backwards PDB. However we can immediately see that this simplest scenario is impossible. The mixing collector orbit $(0,2)^+$ with zero emitter collisions per period and an emitter orbit $(2,2)^+$ with *two* emitter collisions per period can never be created in a *single* cusp bifurcation.

If it were possible, than at the cusp bifurcation these two orbits would have zero z and y components of the velocity at two *different* points of collision with the emitter barrier³². Since the total kinetic energy of the electron must be the same at any collision with the emitter barrier, this means that the velocities at each of the collisions with the emitter wall will differ only by the sign of v_x . That is possible only for a zero tilt angle, when the system possesses reflection symmetry.

What must happen instead is that the $(0,2)^+$ is born in a cusp bifurcation with an orbit of the type $(1,2)^+$ (see Fig. 24), which infinitesimally above the CB is connected to the emitter at one point and not two. For small tilt angle the reflection symmetry is only weakly broken and the other leg of this orbit will be quite close to the emitter, but it may not touch. Eventually, the creation of this orbit leads to the creation of a $(2,2)^+$ orbit (see Fig. 24), which is absorbed by the $(1,1)^+$ in a backwards inverse PDB. However the qualitative scenario changes several times with increasing tilt angle and may be quite subtle, with no less than four regimes which are relevant to the recent experiments. Since

the orbits involved control much of the peak-doubling behavior at larger tilt angles, we will describe these scenarios in some detail here. In the next paper¹³ we will make specific connections to the data of Muller et al.¹¹

Regime One ($\theta < \hat{\theta}_1$): This regime is described completely by continuity arguments once it is understood that the mixing $(0, 2)^+$ collector orbit must pair with a $(1, 2)_1$ orbit. As β increases above the threshold $\beta_c \approx \pi\sqrt{\gamma}(1+2k)$ (where $k = 0, 1, \dots$ is the interval number) the $(0, 2)^+$ and $(1, 2)_1$ orbit are created in a CB. In a very small interval of β this $(1, 2)_1$ orbit attaches its other leg to the emitter and becomes a $(2, 2)^+$ orbit in a connectivity transition of the type described in section IV.B.3 above. The $(1, 2)_1$ orbit must have been born unstable at the CB and since the $(0, 2)^+$ orbit it creates is mixing at the collector we expect it to remain unstable as it loses cyclotron energy until it is absorbed in a backwards inverse PDB with the $(1, 1)^+$ orbit. The $(1, 1)^+$ then becomes unstable and is shortly after restabilized by its backwards PDB with the $(2, 2)^-$ orbit. All steps are consistent with the continuity argument from $\theta = 0$. The bifurcation diagram in Figs. 28 illustrates the behavior in this regime.

The $(1, 1)^+$ continues its evolution until it vanishes in the backwards tangent bifurcation described above and neither creates nor destroys any further period-two emitter orbits. However there is a new period-two orbit created by the $(0, 1)^+$ collector orbit. It behaves just as in the SBM and goes unstable creating a $(0, 2)^*$ orbit which is the exact analog of the $(2)^*$ orbit of the SBM. However this only occurs at large β values and the orbit never reaches the emitter once it is created, so it is not relevant to the experiments at small tilt angle. We mention it because it will become very relevant at large tilt angles.

Regime Two ($\hat{\theta}_1 < \theta < \hat{\theta}_2$): The behavior in this regime is as follows. As β increases, as before, the first event is the creation of the $(0, 2)^+$ collector orbit and the $(1, 2)_1$ orbit via CB. This $(1, 2)_1$ orbit evolves for some interval in β without becoming a $(2, 2)^+$ and in this interval a second CB occurs in which a distinct orbit $(1, 2)_2$ and a $(2, 2)^+$ are created - see Fig. 29a) (this can happen because their connectivity only differs by one). At slightly higher β still the two orbits $(1, 2)_1, (1, 2)_2$ annihilate in a backwards TB and a yet higher β the $(2, 2)^+$ orbit is absorbed by the traversing orbit in the now-familiar PDB. The net effect of the creation of this second orbit $(1, 2)_2$ is to eliminate the connectivity transition directly from $(1, 2)_1$ to $(2, 2)^+$. The dynamics seems to rapidly eliminate these transitions even though they are not strictly forbidden; preferring to replace one connectivity transition with a CB and TB which results in the same final state. The total number of $(1, 2)$ orbits is increased to two by this change.

Regime Three ($\hat{\theta}_2 < \theta < \hat{\theta}_3$): As already mentioned, a further period-two orbit, $(0, 2)^*$ is created by the PDB of the $(0, 1)^+$ collector orbit, exactly as the $(2)^*$ orbit is created in the SBM. As tilt angle is increased this PDB moves to lower and lower β until at the value $\hat{\theta}_2$, it coincides with the cusp bifurcation which creates the $(1, 1)^-$ and $(0, 1)^+$ orbits. For larger θ a period-two emitter orbit of type ν is created at this CB. Thus in a somewhat mysterious manner this CB is a “point of accumulation” for the creation of higher period orbits (a similar thing happens for period-three here as well). We may call this orbit $(1, 2)_1^*$ since it is similar in many ways to the $(2)^*$ orbit of the SBM. For example it has no analog in the untilted system. Just above the critical angle $\hat{\theta}_2$ this $(1, 2)_1^*$ orbit is barely reaching the emitter and it rapidly detaches for higher β and becomes a collector orbit. As θ is increased, very quickly this connectivity transition is again replaced by a combination of CB and TB, where in this case the CB involves the $(0, 2)^*$ collector orbit and a second $(1, 2)^*$ orbit, $(1, 2)_2^*$. The orbits $(1, 2)_1^*, (1, 2)_2^*$ then annihilate at higher β in tangent bifurcation (see Fig. 29b,c). So except for very near the critical angle $\hat{\theta}_2$, there are now a total of four ν orbits associated with the first interval. These are the two ν^* orbits just mentioned, which are connected with the cusp bifurcation of the $(0, 1)^+, (1, 1)^-$ orbits, and the two $(1, 2)^+$ orbits which can be associated with the destabilizing PDB of the $(1, 1)^+$ traversing orbit. Therefore, although the scenario is substantially more complicated than in the SBM, the bifurcations of the period-one orbits in the first interval determine all the relevant period-two orbits.

For most of this interval the two $(1, 2)^+$ orbits exist at lower β than the two $(1, 2)^*$ orbits. However as the next critical angle $\hat{\theta}_3$ is approached the intervals of existence of these pairs of orbits begin to overlap and their associated fixed point move together (see Fig. 29c). The final act is about to take place.

Regime Four ($\theta > \hat{\theta}_3$): Recall that in the SBM the different branches of the $(2)^*$ and $(2)^+$ orbits linked up above the critical angle θ^\dagger . In that case the link was established by the merging of the PDBs at which these orbits were created from the traversing orbit. In the DBM a similar connection now occurs for the $(1, 2)^*$ and $(1, 2)^+$ orbits via an “exchange of partners” bifurcation (note, that we already encountered this bifurcation in the SBM - see the description of three-bounce orbits). The $(1, 2)_1$ and $(1, 2)_2^*$ orbits are both created at cusp bifurcations with collector orbits (which are identical to the $(2)^+, (2)^*$ orbits of the SBM) and are annihilated at tangent bifurcations with their partners $(1, 2)_2, (1, 2)_1^*$. At a critical angle $\hat{\theta}_3$ the $(1, 2)_2$ and $(1, 2)_1^*$ orbits exchange partners. Above this angle, the $(1, 2)_1$ orbit born in CB with the $(0, 2)^+$ annihilates in a TB with the $(1, 2)_2^*$ orbit born in a CB with the $(0, 2)^*$; whereas the $(1, 2)_2$ orbit born in a CB with the (one and only) $(2, 2)^+$ orbit now annihilates with the $(1, 2)_1^*$ orbit born at the CB of the period-one orbits - see Fig. 29d.

After the “exchange of partners” transition the $(1, 2)_1$ orbits exists for a very large interval of β and has relatively low cyclotron energy. Thus it plays a dominant role in the tunneling spectrum in this interval of β . The importance

of this orbit has been emphasized in work of Fromhold⁹.

In contrast, the other pair of orbits, $(1, 2)_2^+$, $(1, 2)_1^*$, decrease their interval of existence because the PDB and CB to which they are connected move together.

In Fig. 27 we show the behavior of the trace of the monodromy matrix for different period-2 orbits. Note, that the orbit $(1, 2)^+$ does not become highly unstable in the whole interval of its existence and is therefore expected to produce strong scars in the quantum-mechanical wavefunctions^{34–36}.

To summarize the complicated story of the period-two orbits : For small tilt angles the important orbits are the $(2, 2)$ orbits we have denoted as $(2, 2)^-$ orbits. As tilt angle increases the importance of $(1, 2)$ orbits increases and eventually they become the dominant period-two orbits in the first interval. Since higher intervals correspond to greater chaoticity, they become important more quickly in the second interval. These $(1, 2)$ orbits are created in a complicated bifurcation tree which connects to a period-doubling bifurcation of the period-one traversing orbit, as well as cusp bifurcations with various period-one and period-two collector orbits. It is very difficult to discern these relationships from simple observations of the SOS as many of these orbits are born highly unstable in cusp bifurcations and certain of the transitions described occur over very small angular intervals.

D. Period-3 orbits

All of the qualitative differences between the periodic orbit theory of the SBM and that of the DBM already have entered into the description of the period-one and two orbits. However, peak-tripling regions have been clearly observed in experimental tunneling spectra, indicating that the behavior of period-three orbits is relevant to these experiments. Moreover there has been a recent Comment questioning the interpretation proposed for these peak-tripling regions^{17,33} in ref.¹¹, where they were attributed to trifurcations of the traversing orbit. Since we are able to reach a complete understanding of these orbits based on the principles used in discussing the period-one and two orbits, we will briefly summarize their properties.

As for the period-2 orbits, for small tilt angles the main period-3 orbits are those related to the resonances of the traversing orbit. When the tilt angle is exactly zero, the traversing orbit has *two* 1 : 3 resonances in each interval, when its period is equal to $2\pi(k+1)T_c/3$ and $4\pi(k+1)T_c/3$ respectively. The behavior near each of these resonances is essentially the same for small tilt angles, so we just consider the first one. First, an emitter and collector family is created at the critical boundary at $\beta_{c1} < \beta_1$. The emitter family moves inwards in the SOS and collapses to the TO at resonance. When the field is tilted only two period-three orbits survive from each emitter family and they are now created in cusp bifurcations with the corresponding collector families at slightly different values of β .

As with the period-two orbits in the DBM, these emitter orbits will move inwards in the SOS until they annihilate. The one difference in their behavior has already been noted in the discussion of the SBM (see section III.D). Because period-three orbits generically are not born or absorbed in bifurcations with a period-one orbit, these two orbits cannot disappear precisely on resonance with the TO. Instead one of them (the unstable one) passes through the fixed point associated with the $(1, 1)^{k+}$ traversing orbit in a touch-and-go bifurcation and then annihilates with the other in a backward tangent bifurcation. For all tilt angles the interval between the TAG bifurcation and the TB is negligibly small, and so practically speaking it is as if these two orbits vanish in a “backwards trifurcation”.

Again, as with the period-two orbits, for finite tilt angle the emitter orbits cannot be created as $(3, 3)$ orbits at the initial cusp bifurcation. Therefore the two emitter orbits just described are created in the form of a $(1, 3)$ and a $(2, 3)$ orbit. These orbits are the analogs of the period-two $(1, 2)$ orbits, but now there are two different types of orbits with less than the maximum $(3, 3)$ connectivity to the emitter. In $y - z$ projection the $(3, 3)$ orbits each have a mixing collision point (where two collisions occur) and a non-mixing collision point (where only one collision occurs, see Fig. 30.). The $(1, 3)$ orbits correspond to detaching the orbit at the mixing collision point, the $(2, 3)$ orbits correspond to detaching it at the non-mixing collision point. As noted, both occur for each resonance.

For small tilt angles the $(1, 3)$ and $(2, 3)$ orbits created at these cusp bifurcations evolve by connectivity transitions into the stable and unstable $(3, 3)$ orbits which participate in the TAG/TB behavior already described. At higher tilt angles, as for the period-two orbits, the connectivity transitions are replaced by the appearance of a new $(1, 3)$ and $(2, 3)$ orbit which through a combination of CB and TB leads to the same final state. In the regime of small tilt angle there are six period-three orbits created in the neighborhood of each resonance: two collector orbits, a $(1, 3)$, a $(2, 3)$ and two $(3, 3)$ orbits. For large tilt angles there are *eight* period-three orbits due to the new $(1, 3)$ and $(2, 3)$ orbits which arise to replace the connectivity transitions (see Fig. 31). The bifurcation diagrams of Fig. 31 summarize the behavior of the family of period-three orbits related to the first resonance; qualitatively the same behavior is observed at the second resonance as well. In Fig. 32 we show the behavior of the trace of the monodromy matrix for these orbits. Note, that as for the period-2 orbits, there is one orbit which, although exists in a substantial interval, does not become too unstable (the orbit $(1, 3)^-$) and is therefore expected to produce strong scars.

The (1, 3) and (2, 3) orbits in each family appear at lower magnetic field than the resonance value, and evolve either directly or indirectly into the (3, 3) orbits. One of these orbits has been identified previously by Fromhold et al.^{18,17} in connection with peak-tripling. We will analyze the relation of the entire family to the experimental observations in the following paper. We simply point out here that each family of eight period-three orbits is connected to a period-three resonance through bifurcation processes, and in the scheme presented in this paper they arise as a natural consequence of that resonance.

As noted, for small tilt angles both resonances between the period-three and period-one orbits in the first interval are similar, with the creation of six or eight period-three orbits, four of which are related by continuity to tori of the unperturbed system. As with the period-two orbits, there is another resonance corresponding to $T = 3T_c$ which occurs in the first interval, but initially for very high β . This resonances will give rise to (1, 3) and (2, 3) orbits analogous to the $(1, 2)^*$ period-two orbits. For small tilt angles they are created near the (0, 1) collector orbit and do not reach the emitter, as happened also for the $(1, 2)^*$. Just as for that case, as tilt angle is increased the resonance moves “down” to the period-one cusp bifurcation and now gives rise to emitter orbits. These emitter orbits then evolve similarly to the $(1, 2)^*$ orbits with exchange of partner bifurcations, etcetera. However, the periods of these orbits ($T > 2T_c$) apparently are too long for them to be resolved as resonance peaks in the experimental data of ref.¹¹.

Higher period orbits also appear in families in connected bifurcation sequences which begin with collector orbits and end with fully connected emitter orbits which are annihilated at resonances with the TO. The principles and analytic relations we have derived can be used to develop a quantitative theory of such orbits, but we have focused here on those which are experimentally-relevant and will defer any such analysis to other work. The relevant orbits at the DBM are summarized in Table II.

V. SUMMARY AND CONCLUSIONS

We have developed a complete qualitative and quantitative theory of the periodic orbits relevant to the magneto-tunneling spectra of quantum wells in tilted magnetic field.

First we introduced two model hamiltonians and showed how to scale the variables so that the only one or two dimensionless parameters β, γ describe the classical dynamics at fixed θ . As $\gamma = eV/\epsilon_0$ is approximately constant in experiments, the dependences on magnetic field, voltage and injection energy are all summarized by the behavior of the Poincaré velocity map as a function of the variables β, θ .

The periodic orbit theory was first developed for the single-barrier model which elucidates many of the qualitative features of the system. In particular, the SBM describes a standard KAM transition to chaos as a function of tilt angle. The period-one orbit with the smallest cyclotron energy (the traversing orbit) plays a fundamental role in the transition, with the relevant periodic orbits appearing through the bifurcations of this orbit. These bifurcations follow the known bifurcation rules for generic (2D) conservative maps. However the detailed scenario for the bifurcations evolves with tilt angle in a complicated manner, which nonetheless can be understood using continuity arguments. Exact analytic expressions for the period and stability of most of the relevant orbits were obtained for all parameter values, something which has not been possible for other experimentally-studied chaotic quantum systems. We note again that the SBM could be realized in a practical double-barrier structure in which the band profiles were chosen to reduce the emitter energy appropriately.

In generalizing the theory to the double-barrier model which is relevant to the present generation of experiments we uncovered several new features of the dynamics. Perhaps most interesting was the discovery that *all* relevant orbits (except the traversing orbit) are created in a new kind of bifurcation, called a cusp bifurcation, which can violate generic bifurcation rules due to the discontinuity in the Poincaré map on the curve separating initial conditions which reach the emitter from those which do not. These orbits are created in families near, but below, the value of β at which resonances with the traversing orbit occur. They only exist for a finite interval of β (or magnetic field) and then annihilate in backwards bifurcations with the traversing orbit or in tangent bifurcations. In a given family of period- n orbits (n collisions with the collector per period) there will exist orbits with $0, 1, \dots, n$ emitter collisions, connected together by one or more bifurcation “trees”. Typically, several orbits in a given family will be relevant for understanding the magnetotunneling spectra, with their relative importance changing as a function of tilt angle.

Having determined the periods and stability of all the orbits which are short enough to resolve in the experimental tunneling spectra, we can now calculate the tunnel current semiclassically using Equation (1) quoted above. In the companion paper to this work we will derive this equation and compare its predictions qualitatively and quantitatively to the data of Muller et al.¹¹. The complicated evolution of the observed spectra with increasing tilt angle finds a natural explanation in this approach. The ability to develop a semiclassical theory in essentially analytic form makes this system unique among the few quantum systems which have been studied experimentally in the transition regime to chaos.

VI. ACKNOWLEDGEMENTS

The authors wish to thank G. Boebinger, M. Fromhold, H. Mathur, T. Monteiro and D. Shepelyansky for helpful discussions. We particularly thank Monteiro for pointing out to us the importance of the (1,2) orbits even at tilt angles as small as 11° , and for explaining that the period-three bifurcations follow the touch-and-go scenario. The work was partially supported by NSF grant no. DMR-9215065. We also acknowledge the hospitality of the Aspen Center for Physics where some of this work was done.

APPENDIX A: THE MONODROMY MATRIX FOR THE SINGLE-BOUNCE PERIODIC ORBITS

In this Appendix we derive the expressions for the components and the trace of the monodromy matrix for the period - one orbits in the single barrier model.

By definition, the monodromy matrix $M^* = (m_{ij}^*)$ of a period-one orbit is the matrix, which represents the linearized Poincaré map, calculated at the position of the single-bounce periodic orbit $(\tilde{v}_x^*, \tilde{v}_y^*)$ in the Poincaré surface of section :

$$\begin{aligned}\Phi_x(\tilde{v}_x^* + \delta\tilde{v}_x, \tilde{v}_y^* + \delta\tilde{v}_y) &= \tilde{v}_x^* + m_{11}^* \tilde{v}_x^* + m_{12}^* \tilde{v}_y^* + O\left((\delta\tilde{v}_x)_0^2, (\delta\tilde{v}_y)_0^2, (\delta\tilde{v}_x)_0 (\delta\tilde{v}_y)_0\right) \\ \Phi_y(\tilde{v}_x^* + \delta\tilde{v}_x, \tilde{v}_y^* + \delta\tilde{v}_y) &= \tilde{v}_y^* + m_{21}^* \tilde{v}_x^* + m_{22}^* \tilde{v}_y^* + O\left((\delta\tilde{v}_x)_0^2, (\delta\tilde{v}_y)_0^2, (\delta\tilde{v}_x)_0 (\delta\tilde{v}_y)_0\right)\end{aligned}\quad (A1)$$

The monodromy matrix m_{ij}^* therefore relates to each other the deviation $\delta\tilde{\mathbf{v}}$ from the location of the periodic orbit after one iteration of the Poincaré map to the initial deviation $\delta\tilde{\mathbf{v}}_0$ in the limit $|\delta\tilde{\mathbf{v}}| \rightarrow 0$:

$$\begin{pmatrix} \delta\tilde{v}_x \\ \delta\tilde{v}_y \end{pmatrix} = \begin{pmatrix} m_{11}^* & m_{12}^* \\ m_{21}^* & m_{22}^* \end{pmatrix} \begin{pmatrix} (\delta\tilde{v}_x)_0 \\ (\delta\tilde{v}_y)_0 \end{pmatrix} + O(\delta\tilde{v}^2)\quad (A2)$$

Expanding the Poincaré map (15) in $\delta\tilde{\mathbf{v}}$, we obtain :

$$\begin{aligned}\Phi_x(\tilde{v}_x^* + \delta\tilde{v}_x, \tilde{v}_y^* + \delta\tilde{v}_y) &= \tilde{v}_x^* \\ &+ \delta T \left(\frac{\sin \theta \omega_c T^*}{\beta} \cos(\omega_c T^*) - \left(\tilde{v}_x^* - \frac{2 \sin \theta}{\beta} \right) \sin(\omega_c T^*) \right) \\ &+ (\delta\tilde{v}_x)_0 \left(\cos(\omega_c T^*) - \frac{\sin \theta \beta \tilde{v}_x^*}{\omega_c T^*} \sin(\omega_c T^*) \right) \\ &- (\delta\tilde{v}_y)_0 \cos \theta \sin(\omega_c T^*) \\ &+ O\left((\delta\tilde{v}_x)_0^2, (\delta\tilde{v}_y)_0^2, (\delta\tilde{v}_x)_0 (\delta\tilde{v}_y)_0\right)\end{aligned}\quad (A3)$$

$$\begin{aligned}\Phi_y(\tilde{v}_x^* + \delta\tilde{v}_x, \tilde{v}_y^* + \delta\tilde{v}_y) &= \tilde{v}_y^* \\ &+ \delta T \cos \theta \left(\left(\tilde{v}_x^* - \frac{2 \sin \theta}{\beta} \right) \cos(\omega_c T^*) + \sin \theta \sqrt{1 - (\tilde{v}_x^*)^2} \sin(\omega_c T^*) \right. \\ &\quad \left. - \frac{2 \sin \theta}{\beta} \right) \\ &+ (\delta\tilde{v}_x)_0 \cos \theta \left(\sin(\omega_c T^*) - \frac{\tilde{v}_x^* \sin \theta}{\sqrt{1 - (\tilde{v}_x^*)^2}} (1 - \cos(\omega_c T^*)) \right) \\ &+ (\delta\tilde{v}_y)_0 (\cos^2 \theta \cos(\omega_c T^*) + \sin^2 \theta) \\ &+ O\left((\delta\tilde{v}_x)_0^2, (\delta\tilde{v}_y)_0^2, (\delta\tilde{v}_x)_0 (\delta\tilde{v}_y)_0\right)\end{aligned}\quad (A4)$$

where the parameter δT is the different between the time interval to the next collision of the electron with the barrier $T(\beta, \theta; \tilde{v})$ and the period of the single-bounce periodic orbit T^* :

$$T(\beta, \theta; \tilde{v}) = T^*(\beta, \theta) + \delta T\quad (A5)$$

To obtain the linearization of the Poincaré map in terms of the velocity deviations, we therefore need to calculate the expansion of δT up to linear order in $(\delta \tilde{v}_x)_0$ and $(\delta \tilde{v}_y)_0$. This result can be obtained from the equation (17), which relates the scaled in-plane components of the velocity of the electron (\tilde{v}_x, \tilde{v}_y at the point of collision with the barrier to the time interval T to the next collision. Substituting the expression (A5) into the equation (17), we obtain :

$$\begin{aligned} \delta T = & -\frac{\sin \theta (1 - \cos(\omega_c T^*)) + \beta \tilde{v}_x^* \left(\cos^2 \theta + \sin^2 \theta \frac{\sin(\omega_c T^*)}{\omega_c T^*} \right)}{\frac{\omega_c T^*}{\beta} (\cos^2 \theta - \sin^2 \theta \cos(\omega_c T^*)) + \sin \theta \sin(\omega_c T^*) \left(\tilde{v}_x^* + \frac{2 \sin \theta}{\beta} \right)} (\delta \tilde{v}_x)_0 \\ & + \sin \theta \cos \theta \frac{\omega_c T^* - \sin(\omega_c T)}{\frac{\omega_c T^*}{\beta} (\cos^2 \theta - \sin^2 \theta \cos(\omega_c T^*)) + \sin \theta \sin(\omega_c T^*) \left(\tilde{v}_x^* + \frac{2 \sin \theta}{\beta} \right)} (\delta \tilde{v}_y)_0 \\ & + O\left((\delta \tilde{v}_x)_0^2, (\delta \tilde{v}_y)_0^2, (\delta \tilde{v}_x)_0 (\delta \tilde{v}_y)_0\right) \end{aligned} \quad (\text{A6})$$

Substituting (A6) into (A3), (A4) and using the expression (38) for the scaled velocity for the one-bounce periodic orbit, we obtain the following result for the components of the monodromy matrix :

$$\begin{aligned} m_{11}^* &= \sin^2 \theta + \cos^2 \theta \cos(\omega_c T^*) - 2 \sin^2 \theta \cos^2 \theta \left(1 - \frac{\omega_c T^*}{\tan(\omega_c T^*)} \right) \left(1 - \frac{\sin(\omega_c T^*)}{\omega_c T^*} \right) \\ m_{12}^* &= -\cos \theta (\sin^2 \theta \omega_c T^* + \cos^2 \theta \sin(\omega_c T^*)) \\ m_{21}^* &= \cos \theta \sin(\omega_c T^*) + \frac{4 \sin^2 \theta \cos \theta}{\omega_c T^*} \left(1 - \frac{\frac{\omega_c T^*}{2}}{\tan(\frac{\omega_c T^*}{2})} \right) \\ &\quad \times \left(1 - \cos(\omega_c T^*) - \left(1 - \frac{\frac{\omega_c T^*}{2}}{\tan(\frac{\omega_c T^*}{2})} \right) \left(\cos^2 \theta + \sin^2 \theta \frac{\sin(\omega_c T^*)}{\omega_c T^*} \right) \right) \\ m_{22}^* &= m_{11}^* \end{aligned} \quad (\text{A7})$$

and the trace of the monodromy matrix is therefore given by

$$\text{tr}(M^*) = 2m_{11}^* \quad (\text{A8})$$

For the analysis of the stability of the single-bounce periodic orbits it is convenient to represent the expression for $\text{tr}(M^*)$ as a sum of -2 (which is the critical value of the trace of the monodromy matrix, when a periodic orbit bifurcates and loses stability), and some additional, depending on the tilt angle θ and other parameters, term. This can be achieved by a trivial rearrangement of terms giving

$$\begin{aligned} \text{tr}(M^*) &= -2 + 4 \cos^4(\theta) (\tan^2(\theta) + (\omega_c T^*/2) \cot(\omega_c T^*/2)) \\ &\quad \times (\tan^2(\theta) + \sin(\omega_c T^*)/(\omega_c T^*)) \end{aligned} \quad (\text{A9})$$

which is exactly the equation (44).

APPENDIX B: PERIOD-DOUBLING BIFURCATIONS OF SINGLE-BOUNCE ORBITS AND THE SCALING OF THE POINCARÉ MAP

In this appendix we consider the evolution of the single-bounce orbits $(1)^{+(k)}$, which appear in tangent bifurcations together with the unstable orbits $(1)^{-(k)}$. As follows from the expression (44) for the trace of the monodromy matrix and Eq. (40), immediately after the tangent bifurcation all $(1)^{+(k)}$ orbits are stable ($-2 < \text{tr}(M) \leq 2$ - see Fig. 7).

At $\beta = \beta_{b1}^{(k)}$, where

$$\beta_{b1}^{(k)} = \mathcal{F}(\sin \theta, \iota_k(-\tan^2 \theta)) \quad (\text{B1})$$

the function \mathcal{F} is defined in (42) and $\iota_k(a)$ is the k -th positive root of the equation

$$\frac{\iota}{\tan \iota} = a, \quad (\text{B2})$$

the trace of the corresponding monodromy matrix reaches the value -2 , and the orbit $(1)^{+(k)}$ goes unstable via a period-doubling bifurcation. At that moment a new stable two-bounce periodic orbit with the period exactly twice the period of $(1)^{+(k)}$ is born in the neighborhood.

However, although *all* one-bounce periodic orbits $(1)^{+(k)}$ ($k = 0, \dots, \infty$) show the period-doubling bifurcation at $\beta = \beta_k^{\text{b1}}$, the further evolution of the $(1)^{+(k)}$ periodic orbits depends on θ and k and is qualitatively different for $\theta < \theta_k^\dagger$ and $\theta \geq \theta_k^\dagger$, where

$$\theta_k^\dagger = \arctan \left(\sqrt{-\sin(\xi_k)/\xi_k} \right) \quad (\text{B3})$$

and ξ_k is the $(k+1)$ -th positive root of the equation $\tan(\xi) = \xi$.

Note, that since critical angle θ_k^\dagger is a monotonically decreasing function of k for a fixed value of the tilt angle θ the inequality $\theta < \theta_k^\dagger$ is equivalent to the condition $k < k_{\min}(\theta)$, where the integer $k_{\min}(\theta)$ is the smallest integer value of k , for which the inequality $\theta_k^\dagger < \theta$ still holds. $k_{\min}(\theta)$ is a decreasing function of θ , it diverges as $\text{integer}(1/\theta)$ at $\theta \rightarrow 0$, and $k_{\min}(\theta) = 0$ for $\theta > \theta_0$. The regime $\theta < \theta_k^\dagger$ corresponds to $k \leq k_{\min}(\theta)$, and the regime $\theta > \theta_k^\dagger$ is achieved for $k \geq k_{\min}(\theta)$ (so that for arbitrary θ above at sufficiently high β the system is in the regime $\theta > \theta_k^\dagger$).

First, we consider the case $k < k_{\min}$ (which is non-generic in a sense that it corresponds to a *finite* part of an *infinite* sequence $k = 0, \dots, \infty$). At $\beta = \beta_{\text{b2}}^{(k)}$, where

$$\beta_{\text{b2}}^{(k)} = \mathcal{F}(\sin \theta, \wp(-\tan^2 \theta)) \quad (\text{B4})$$

and $\wp_n(a)$ is the n -th positive root of the equation

$$\frac{\sin \wp}{\wp} = a, \quad (\text{B5})$$

the trace of the monodromy matrix of the one-bounce periodic orbit $(1)^{(k)}$ again passes through the value -2 (see Fig. 7). At this point, the orbit $(1)^{+(k)}$ restabilizes via a period-doubling bifurcation. In this bifurcation, the period-1 orbit $(1)^{(k)}$ can either “emit” an unstable two-bounce orbit or absorb a stable two-bounce orbit. A detailed description of this behavior will be given in section IIIB, where we analyze the properties of the two-bounce orbits.

As follows from the equations (43) and (B1), for a fixed tilt angle θ the intervals of stability of the single bounce orbits $(1, 0)_T^{+k}$ at large k scale as $1/k$. If we introduce an effective “local” parameter β_ℓ such that

$$\beta_\ell = k(\beta - \pi(2k+1)) \quad (\text{B6})$$

then in the limit $k \gg 1$ the values of this local parameter corresponding to the bifurcations of the single-bounce orbits do not depend on k . This property gives us a hint about the existence of a universal limiting behavior of the Poincaré map in the regime $k \gg 1$. Also, using Eqs. (B1), (B4) together with Eq. (40), one can show that for $k \gg 1$ the “nontrivial” part of the evolution of the single-bounce orbit $(1)^{(k)+}$ takes place in the vicinity of the origin of the surface of section, so that the “universality” of the behavior of the Poincaré map is expected to show up for $\tilde{v} \ll 1$.

Introducing the rescaled velocity

$$\mathbf{v}_\ell = \left(\frac{\tilde{v}}{k}, \frac{\tilde{v}}{k^2} \right) \quad (\text{B7})$$

and substituting the expressions of β and $\tilde{\mathbf{v}}$ in terms of the local variables β_ℓ and \mathbf{v}_ℓ into the exact Poincaré map (15), in the leading order in $1/k$ we obtain the following mapping :

$$(\mathbf{v}_\ell)_{n+1} = \Phi_\ell((\mathbf{v}_\ell)_n; \beta_\ell) \quad (\text{B8})$$

where

$$\begin{aligned} (\Phi_\ell)_x &= a_{00} + a_{10}(v_\ell)_x + a_{10}(v_\ell)_x + a_{20}(v_\ell)_x^2 + a_{01}(v_\ell)_y + O\left(\frac{1}{k}\right) \\ (\Phi_\ell)_y &= b_{00} + b_{10}(v_\ell)_x + b_{10}(v_\ell)_x + b_{20}(v_\ell)_x^2 + b_{30}(v_\ell)_x^3 + b_{40}(v_\ell)_x^4 \\ &\quad + b_{01}(v_\ell)_y + b_{02}(v_\ell)_y^2 + b_{11}(v_\ell)_x(v_\ell)_y + b_{21}(v_\ell)_x^2(v_\ell)_y + O\left(\frac{1}{k}\right) \end{aligned} \quad (\text{B9})$$

and

$$\begin{aligned}
a_{00} &= -\cos^2 \theta \sin \theta \left(\beta_\ell + \frac{2}{\pi} \right) \\
a_{10} &= -\cos^2 2\theta \\
a_{20} &= \pi \cos^2 \theta \sin \theta \\
a_{01} &= -2\pi \sin^2 \theta \cos \theta \\
b_{00} &= \sin 2\theta \frac{1 - \cos^4 \theta}{2\pi} - \frac{\sin 2\theta \cos^2 \theta}{\pi^2} - \beta_\ell^2 \frac{2 \sin 2\theta \cos^2 \theta}{4} \\
b_{10} &= \frac{2}{\pi} \cos \theta \sin^2 \theta (3 - 2 \sin^2 \theta) - \beta_\ell \cos 2\theta \cos^3 \theta \\
b_{20} &= \sin 2\theta \left(\cos^4 \theta - \sin^2 \theta + \frac{1}{2} \right) \\
b_{30} &= \pi \cos^3 \theta \cos 2\theta \\
b_{40} &= \frac{\pi^2 \cos^4 \theta \sin 2\theta}{4} \\
b_{01} &= -\cos 2\theta - \frac{\pi \beta_\ell}{2} \sin^2 2\theta \cos^2 \theta \\
b_{02} &= -\frac{\pi^2}{4} \sin^3 2\theta \\
b_{11} &= -\frac{\pi}{2} \sin 4\theta \cos \theta \\
b_{21} &= \frac{\pi^2}{2} \sin^2 2\theta \cos^2 \theta
\end{aligned}$$

In Fig. 33 we compare the Poincaré surfaces of section of the mapping (B8) with Poincaré Surfaces of section of the exact map (15) for different values of index k . An excellent agreement is found even for relatively small values of the index.

APPENDIX C: THE MONODROMY MATRIX FOR A MANY - BOUNCE ORBIT IN SBM

To obtain the monodromy matrix for the period-one orbits, we essentially used the non-mixing property of the single-bounce periodic orbits. Therefore, it may seem, that an analytical expression for the trace of the monodromy matrix may be obtained only for the simplest non-mixing orbits. However, it is not the case in the tilted well. The non-mixing property of a periodic orbit substantially simplifies the calculation of the corresponding monodromy matrix, but it is not necessary to get an analytical description of the stability, as it will be shown in the present Appendix.

Consider a general (mixing) periodic orbit with n collisions with the barrier per period. Let $\tilde{\mathbf{v}}_k \equiv ((\tilde{v}_x)_k, (\tilde{v}_y)_k, (\tilde{v}_z)_k)$ and t_k be the scaled velocity immediately *after* the k -th collision and the time interval from k -th to $(k+1)$ -th collision respectively. Once the values of $\tilde{\mathbf{v}}_k$ and t_k are known, one can linearize the Poincaré map near the point $((\tilde{v}_x)_k, (\tilde{v}_y)_k)$:

$$\begin{aligned}
(\delta \tilde{v}_x)_{k+1} &= (M_k)_{11} (\delta \tilde{v}_x)_k + (M_k)_{12} (\delta \tilde{v}_y)_k \\
(\delta \tilde{v}_y)_{k+1} &= (M_k)_{21} (\delta \tilde{v}_x)_k + (M_k)_{22} (\delta \tilde{v}_y)_k
\end{aligned} \tag{C1}$$

where $\delta \tilde{\mathbf{v}}_k$ and $\delta \tilde{\mathbf{v}}_{k+1}$ are the deviations of the velocity from $\tilde{\mathbf{v}}_k$ and from $\tilde{\mathbf{v}}_{k+1}$ respectively, and the matrix M_k is defined as follows

$$M_k = \begin{pmatrix} \left. \frac{\partial \Phi_x(\tilde{v}_x, \tilde{v}_y)}{\partial \tilde{v}_x} \right|_{\tilde{\mathbf{v}}=\tilde{\mathbf{v}}_k} & \left. \frac{\partial \Phi_x(\tilde{v}_x, \tilde{v}_y)}{\partial \tilde{v}_y} \right|_{\tilde{\mathbf{v}}=\tilde{\mathbf{v}}_k} \\ \left. \frac{\partial \Phi_y(\tilde{v}_x, \tilde{v}_y)}{\partial \tilde{v}_x} \right|_{\tilde{\mathbf{v}}=\tilde{\mathbf{v}}_k} & \left. \frac{\partial \Phi_y(\tilde{v}_x, \tilde{v}_y)}{\partial \tilde{v}_y} \right|_{\tilde{\mathbf{v}}=\tilde{\mathbf{v}}_k} \end{pmatrix} \tag{C2}$$

Using the definition of the functions Φ_x, Φ_y (15), we obtain the following expressions for the components of the matrix M_k :

$$\begin{aligned}
(M_k)_{11} &= \cos(\omega_c t_k) - \frac{(\tilde{v}_x)_k \sin \theta \sin(\omega_c t_k)}{(\tilde{v}_z)_k} + \kappa_{1t} \kappa_{t1} \\
(M_k)_{12} &= -\cos \theta \sin(\omega_c t_k) - \frac{(\tilde{v}_y)_k \sin \theta \sin(\omega_c t_k)}{(\tilde{v}_z)_k} + \kappa_{1t} \kappa_{t2} \\
(M_k)_{21} &= \cos \theta \sin(\omega_c t_k) - \frac{(\tilde{v}_y)_k \sin \theta \cos \theta (1 - \cos(\omega_c t_k))}{(\tilde{v}_z)_k} + \kappa_{2t} \kappa_{t1} \\
(M_k)_{22} &= \cos^2 \theta \cos(\omega_c t_k) + \sin^2 \theta - \frac{(\tilde{v}_y)_k \sin \theta \cos \theta (1 - \cos(\omega_c t_k))}{(\tilde{v}_z)_k} + \kappa_{2t} \kappa_{t2}
\end{aligned} \tag{C3}$$

where

$$\begin{aligned}
\kappa_{1t} &= (\tilde{v}_z)_k \sin \theta \cos(\omega_c t_k) - \frac{2 \sin \theta \sin(\omega_c t_k)}{\beta} \\
&\quad - (\tilde{v}_x)_k \sin(\omega_c t_k) - (\tilde{v}_y)_k \cos \theta \cos(\omega_c t_k) \\
\kappa_{2t} &= (\tilde{v}_z)_k \sin \theta \cos \theta \sin(\omega_c t_k) - \frac{2 \sin \theta \cos \theta (1 - \cos(\omega_c t_k))}{\beta} \\
&\quad + (\tilde{v}_z)_k \cos \theta \cos(\omega_c t_k) - (\tilde{v}_y)_k \cos^2 \theta \sin(\omega_c t_k) \\
\kappa_{t1} &= - \left(\sin \theta (1 - \cos(\omega_c t_k)) + \frac{(\tilde{v}_x)_k (\cos^2 \theta + \sin^2 \theta \sin(\omega_c t_k))}{(\tilde{v}_z)_k} \right) \zeta_k^{-1} \\
\kappa_{t2} &= \left(\sin \theta \cos \theta (t_k - \sin(\omega_c t_k)) - \frac{(\tilde{v}_y)_k (\cos^2 \theta + \sin^2 \theta \sin(\omega_c t_k))}{(\tilde{v}_z)_k} \right) \zeta_k^{-1} \\
\zeta_k &= \sin \theta \sin(\omega_c t_k) \left((\tilde{v}_x)_k + \frac{2 \sin \theta}{\beta} \right) + \frac{\omega_c t_k (\cos^2 \theta - \sin^2 \theta \cos(\omega_c t_k))}{\beta}
\end{aligned}$$

The matrix M_k relates the deviations of the velocity from the periodic orbit after two successive iterations of the Poincaré map, and is therefore directly connected to the monodromy matrix. The monodromy matrix of a period- n orbit relates the velocity deviation after the first collision to the velocity deviation after the n -th collision. Therefore, the monodromy matrix can be obtained as :

$$M = \Pi_{k=1}^n M_k \tag{C4}$$

The equations (C4) and (C3) give the analytical expressions for the components of the monodromy matrix in terms of the properties of the periodic orbit and are the final results of this Appendix.

APPENDIX D: PERIODS OF NON-MIXING TWO-BOUNCE ORBITS

As in the case of single bounce orbits, the derivation of the periods of the two-bounce periodic orbits is most easily performed in the “drifting” coordinate system (x'', y'', z'') , which was defined in (37). In this coordinate system, the electron moves under the action of electric and magnetic fields, which are *both* parallel to the z'' axis : $\mathbf{E} = E \cos \theta \hat{z}''$, $\mathbf{B} = B \hat{z}''$. An immediate consequence of this fact is, that in this coordinate system the kinetic energy of the electron at the point of collision depends on the corresponding value of z'' :

$$\left. \frac{m^* v^2}{2} \right|_{z''_1} - \left. \frac{m^* v^2}{2} \right|_{z''_2} = -eE \cos \theta (z''_1 - z''_2) \tag{D1}$$

Projected onto the plane (x'', y'') , a two-bounce periodic orbit forms a repeating pattern of two arcs of two different circles, as shown in fig. 34. Each “kink” in the projection of the trajectory corresponds to a collision with the barrier, when the direction of the electron velocity abruptly changes. The radius of each circle is related to the value of the cyclotron velocity : $R_c = v_c / \omega_c$. If the periodic orbit is non-mixing, then there is no energy exchange between cyclotron and longitudinal motion. In this case the cyclotron velocity remains unchanged and the circles have equal radii - see fig. 34(b).

Another consequence of the non-mixing property is that all the successive collisions of the electron with the barrier are separated by equal time intervals, so that the trajectory of the electron is symmetric under mirror reflection

around any vertical (i.e. parallel to the y'') axis, passing through any of the collision points. If it were not true, then the collisions would necessarily have to change the *absolute value* of the y'' components of the velocity. Since the x'' component of the velocity of the electron remains intact at collisions, this will introduce a nonzero energy exchange between cyclotron and longitudinal motion, which contradicts the non-mixing property of the periodic orbit.

At the point of a “non-mixing” collision the electron has zero y component of the velocity. In the drift(ing) coordinate system this condition is equivalent to the following relation :

$$v_{y''} = -v_{z''} \tan \theta \quad (D2)$$

If this is the case, then the collision only reverses *sign* of the velocity in the (y'', z'') plane, leaving the x'' component unchanged:

$$\begin{aligned} v_{x''}^+ &= v_{x''}^- \\ v_{y''}^+ &= -v_{y''}^- \\ v_{z''}^+ &= -v_{z''}^- \end{aligned} \quad (D3)$$

where \mathbf{v}^- and \mathbf{v}^+ are the velocities of the electron immediately before and immediately after the collision respectively.

Let \mathbf{v}_1 and \mathbf{v}_2 be the velocities of the electron, corresponding to two successful (non-mixing) collisions with the barrier (fig. 34b). As follows from (D3) and (12),

$$v_{z''2}^+ = - \left(v_{z''1}^+ - \frac{eE \cos \theta T}{2m^*} \right) \quad (D4)$$

where T is the period of the orbit, equal to twice the time interval between successful collisions. Due to the conservation of the cyclotron energy the equation (D1) reduces to :

$$v_{z''2}^{+2} - v_{z''1}^{+2} = - \frac{2eE \cos \theta}{m^*} (z''_2 - z''_1) \quad (D5)$$

Using (D4), we can rewrite the equation (D5) as

$$v_{z''2}^+ - v_{z''1}^+ = \frac{4}{T} (z''_2 - z''_1) \quad (D6)$$

If α is the phase of the cyclotron rotation immediately after the first collision (at the point (x''_1, y''_1, z''_1) - see fig. 34b), then

$$\begin{aligned} v_{x''1}^+ &= v_c \cos \alpha \\ v_{y''2}^+ &= v_c \cos (\alpha + \omega_c T/2) \end{aligned} \quad (D7)$$

and

$$\begin{aligned} v_{y''1}^+ &= v_c \sin \alpha \\ v_{y''2}^+ &= -v_c \sin (\alpha + \omega_c T/2) \end{aligned} \quad (D8)$$

Substituting (D8) into (D2), we obtain

$$\begin{aligned} v_{z''1}^+ &= -v_c \sin \alpha \tan \theta \\ v_{z''2}^+ &= v_c \sin (\alpha + \omega_c T/2) \tan \theta \end{aligned} \quad (D9)$$

The distance $z''_2 - z''_1$ can be obtained as :

$$z''_2 - z''_1 = (y''_2 - y''_1) \tan \theta \quad (D10)$$

where

$$y''_2 - y''_1 = (x''_2 - x''_1) \tan \left(\pi - \alpha - \frac{\omega_c T}{4} \right) = 2 \frac{v_c}{\omega_c} \sin \frac{\omega_c T}{4} \sin \left(\alpha + \frac{\omega_c T}{4} \right) \quad (D11)$$

Substituting (D9) - (D11) into (D6), we finally obtain :

$$\frac{\omega_c T}{4} \cot \frac{\omega_c T}{4} = -\tan^2 \theta \quad (D12)$$

The k -th positive root of this equation gives the value of the period of the $(2)^{+(k)}$ orbit.

APPENDIX E: THE MONODROMY MATRIX FOR A TWO-BOUNCE NON-MIXING ORBIT

The trace of the corresponding monodromy matrix for a (non-mixing) two bounce orbit can be obtained using the general expressions developed in the Appendix C. For the period-2 orbits the monodromy matrix can be represented as

$$M = M_1 M_2 \quad (\text{E1})$$

where the matrix M_k ($k = 1, 2$) relates the velocity deviations from the periodic orbit at two successive collisions and can be calculated using the relations (C2). As the input information for these machinery one needs the values of the velocity of the electron immediately after each collision with the barrier ($\tilde{\mathbf{v}}_1$ and $\tilde{\mathbf{v}}_2$) and the time intervals between successive collisions (t_1 and t_2).

For the period-2 non-mixing orbits, as we have shown in Appendix D, all the collisions are separated by equal time intervals, so that :

$$t_1 = t_2 = \frac{T}{2} \quad (\text{E2})$$

To obtain the velocity at the point of collision, we can use the energy conservation condition :

$$\varepsilon = \frac{m^*}{2} \left((v_{x''} + v_d)^2 + v_{y''}^2 + v_{z''}^2 \right) \quad (\text{E3})$$

Substituting the expressions for the velocity components at the point of collision (D7), (D8) and (D9) into (E3) and using (D4), we obtain :

$$\left(\frac{\beta \cos^2 \theta}{2 \sin \theta} \right)^2 = \left(1 + \sin^2 \theta \tan^2 \left(\frac{\omega_c T}{4} \right) \right) (1 + \sin^2 \theta \tan^2 \phi) \quad (\text{E4})$$

where we introduced a new angle ϕ , which is defined as

$$\phi = \pi - \alpha - \frac{\omega_c T}{4} \quad (\text{E5})$$

It is more convenient to use ϕ rather than α . In addition to a clear geometrical interpretation of the angle ϕ (see fig. 34b), when the non-mixing two-bounce orbit is born in a period-doubling bifurcation of the period - 1 orbit and is indistinguishable from its second repetition, the value of ϕ is *exactly* equal to zero, which makes ϕ a convenient variable.

Using the equation (E4), we obtain :

$$\tan \phi = \pm \frac{1}{\tan^2 \theta} \sqrt{\frac{\left(\frac{\beta}{2} \right)^2 - \left(\frac{\omega_c T}{4} \right)^2 - \frac{\tan^2 \theta}{\cos^2 \theta}}{1 + \sin^2 \theta \tan^2 \left(\frac{\omega_c T}{4} \right)}} \quad (\text{E6})$$

where the two different solutions correspond to the values of $\tan \phi$ at the two nonequivalent points of collision.

As follows from (E6), a particular period-two non-mixing orbit $(2)^{+k}$ exists only above the critical value of β given by :

$$\beta_{c_2} = \sqrt{\left(\frac{\omega_c T}{2} \right)^2 + \left(\frac{\tan \theta}{\cos \theta} \right)^2} \quad (\text{E7})$$

which is *exactly* equal to the value of $\beta = \beta_{b1}$, corresponding to the first period-doubling bifurcation of the single-bounce orbit $(1)^{+k}$, as expected.

For the velocity components at the points of collision in the non-tilted "stationary" system of coordinates (x, y, z) we therefore obtain:

$$\begin{aligned} (\tilde{v}_x)_{1,2} &= -\frac{2 \sin \theta}{\beta} \left(\frac{1}{\cos^2 \theta} \pm \tan(\omega_c T/2) \sqrt{\frac{\left(\frac{\beta}{2} \right)^2 - \left(\frac{\omega_c T}{4} \right)^2 - \left(\frac{\tan \theta}{\cos \theta} \right)^2}{1 + \sin^2 \theta \tan^2 \left(\frac{\omega_c T}{4} \right)}} \right) \\ (\tilde{v}_y)_{1,2} &= 0 \end{aligned} \quad (\text{E8})$$

The relations (E8) and (50) together with (E1) and (C2) provide the complete information we need for the stability analysis. Substituting (E8) and (50) into (C2), we obtain the matrices M_1 and M_2 . Substituting these expressions into (E1), one can obtain the monodromy matrix M .

APPENDIX F: PERIODS OF THE TYPE-1 MIXING TWO-BOUNCE ORBITS

Projected onto the plane (x'', y'') of the drift(ing) frame of reference, a self-retracing mixing period-2 orbit forms a repeating pattern of two portions of circles of *different* radii, with “kinks” at the points of collision with *exactly* same values of y'' - see fig. 35(b).

Since the x'' component of the velocity is unchanged at collisions, we obtain :

$$v_{c1} \cos\left(\frac{\omega_c t_1}{2}\right) = v_{c2} \cos\left(\frac{\omega_c t_2}{2}\right) \quad (\text{F1})$$

where v_c and t are the cyclotron velocity and the time interval between collisions respectively.

The periodicity of the orbit requires, that the distance traveled by the electron in the drift frame of reference after two successive collisions

$$\delta x''_2 = \frac{2v_{c1}}{\omega_c} \sin\left(\frac{\omega_c t_1}{2}\right) + \frac{2v_{c2}}{\omega_c} \sin\left(\frac{\omega_c t_2}{2}\right)$$

is equal to the displacement of this coordinate system

$$\delta x''_d = v_d (t_1 + t_2)$$

which yields

$$v_{c1} \sin\left(\frac{\omega_c t_1}{2}\right) + v_{c2} \sin\left(\frac{\omega_c t_1}{2}\right) = v_d \omega_c (t_1 + t_2) \quad (\text{F2})$$

Using (F1) together with (F2), we obtain :

$$\begin{aligned} v_{c1} &= v_d \frac{\frac{\omega_c T}{2}}{\sin\left(\frac{\omega_c T}{2}\right)} \cos\left(\frac{\omega_c t_2}{2}\right) \\ v_{c2} &= v_d \frac{\frac{\omega_c T}{2}}{\sin\left(\frac{\omega_c T}{2}\right)} \cos\left(\frac{\omega_c t_1}{2}\right) \end{aligned} \quad (\text{F3})$$

where $T \equiv t_1 + t_2$ is the period of the orbit. The “in-plane” components of the electron velocity $v_{x''}$, $v_{x'}$ and $v_{y'} \equiv v_{y''}$ are therefore given by :

$$\begin{aligned} v_{x''} &= v_d \frac{\frac{\omega_c T}{2}}{\sin\left(\frac{\omega_c T}{2}\right)} \cos\left(\frac{\omega_c t_1}{2}\right) \cos\left(\frac{\omega_c t_2}{2}\right) \\ v_{x'} &= v_d \left(1 + \frac{\frac{\omega_c T}{2}}{\sin\left(\frac{\omega_c T}{2}\right)} \cos\left(\frac{\omega_c t_1}{2}\right) \cos\left(\frac{\omega_c t_2}{2}\right) \right) \\ v_{y''_{1,2}} \equiv v_{y'_{1,2}} &= v_d \frac{\frac{\omega_c T}{2}}{\sin\left(\frac{\omega_c T}{2}\right)} \cos\left(\frac{\omega_c t_{2,1}}{2}\right) \sin\left(\frac{\omega_c t_{1,2}}{2}\right) \end{aligned} \quad (\text{F4})$$

Since the y'' coordinate is the same at each bounce, the longitudinal energy immediately after one collision is equal to the longitudinal energy immediately before the next collision, and the longitudinal velocities $v_{z'_{1,2}}^+ \equiv v_{z''_{1,2}}^+$ immediately after two successive collisions the time intervals t_1 and t_2 between successive collisions must satisfy the relations

$$v_{z'_{1,2}} = \frac{eE \cos \theta t_{1,2}}{2m^*} \quad (\text{F5})$$

Substituting (F4) and (F5) into (13) and using the conservation of the total energy

$$\varepsilon = \frac{m^*}{2} (v_{x'}^2 + v_{y'}^2 + v_{z'}^2)$$

we obtain :

$$\begin{cases} \frac{\sin\left(\frac{\omega_c T}{2}\right)}{\frac{\omega_c T}{2}} = -\tan^2 \theta \frac{\sin\left(\frac{\omega_c \delta T}{2}\right)}{\frac{\omega_c \delta T}{2}} \\ \left(\frac{\beta}{2}\right)^2 = \sin^2 \theta \left(1 - \frac{\frac{\omega_c T}{2} \left(\cos\left(\frac{\omega_c T}{2}\right) + \cos\left(\frac{\omega_c \delta T}{2}\right)\right)}{2 \sin\left(\frac{\omega_c T}{2}\right)}\right)^2 + \left(\frac{\omega_c T}{4}\right)^2 + \cot^2 \theta \left(\frac{\omega_c \delta T}{4}\right)^2 \end{cases} \quad (\text{F6})$$

where $\delta T \equiv |t_2 - t_1|$. This system of two equations defines the periods of all of the type-1 mixing period-2 orbits as functions of β and the tilt angle.

APPENDIX G: DOUBLE BARRIER MODEL : PERIODS OF (1, 1) ORBITS

In this appendix we derive the equation (59). We perform the derivation “drifting” coordinate system (x'', y'', z'') , which was defined in (37). In this coordinate system, the electron moves under the action of electric and magnetic fields, which are *both* parallel to the z'' axis : $\mathbf{E} = E \cos \theta \hat{z}'', \mathbf{B} = B \hat{z}''$. Since the (1, 1) orbit is non-mixing, the cyclotron velocity v_c is conserved and the cyclotron radius $R_c \equiv v_c / \omega_c$ is the same for each part of the trajectory. Therefore, the (x'', y'') projection of the (1, 1) orbit produces a pattern of two arcs of two different circles with *equal* radii and it looks exactly like the (x'', y'') projection of a two-bounce non-mixing orbit (2)⁻ in the single-barrier model (see fig. 34). However, the “kink” at (x_2'', y_2'') is due to collision at the *emitter* barrier (Fig. 34 b), so that the periods of the (1, 1) orbits are different from the ones of (2)⁻.

In the drifting coordinate system the kinetic energy of the electron at the point of collision depends on the corresponding value of z'' , so that (cf. (D1)):

$$\frac{m^* v_2^2}{2} - \frac{m^* v_1^2}{2} = -eE \cos \theta \left(\frac{d}{\cos \theta} + (y''_2 - y''_1) \right) \quad (\text{G1})$$

As for the non-mixing two-bounce orbits (2)⁻ in the single barrier model, the successive collisions of the (1, 1) with different barriers are separated by equal time intervals, so that the trajectory of the electron is symmetric under mirror reflection around any vertical (i.e. parallel to the y'') axis, passing through any of the collision points.

At the point of a “non-mixing” collision with both the emitter and the collector barriers the electron has zero y component of the velocity, therefore at each collision of the (1, 1) orbits the corresponding y'' and z'' components of the electron velocity are related to each other by (D2), while the velocity immediately before the collision \mathbf{v}^- and the velocity immediately after the collision \mathbf{v}^+ satisfy the relations (D3).

Let \mathbf{v}_1 and \mathbf{v}_2 be the velocities of the electron, corresponding to two successful (non-mixing) collisions with the collector and emitter barrier respectively. As follows from (12),

$$v_{z''2}^- = \left(v_{z''1}^+ - \frac{eE \cos \theta T}{2m^*} \right) \quad (\text{G2})$$

where T is the period of the orbit, equal to twice the time interval between successful collisions. Substituting (G2) into (G1) and using the conservation of the cyclotron velocity, we obtain :

$$v_{z''1}^+ + v_{z''2}^- = \frac{4}{T} \left(\frac{d}{\cos \theta} + (y''_2 - y''_1) \tan \theta \right) \quad (\text{G3})$$

If α is the phase of the cyclotron rotation immediately after the collision with the collector wall (at the point (x''_1, y''_1, z''_1) - see Fig. 34b), then

$$\begin{aligned} v_{x''1}^+ &= v_c \cos \alpha \\ v_{y''1}^+ &= v_c \sin \alpha \\ v_{x''2}^- &= v_c \cos (\alpha + \omega_c T / 2) \\ v_{y''2}^- &= v_c \sin (\alpha + \omega_c T / 2) \end{aligned} \quad (\text{G4})$$

and (see (D2)) we obtain

$$\begin{aligned} v_{z''1}^+ &= -v_c \sin \alpha \cot \theta \\ v_{z''2}^- &= -v_c \sin (\alpha + \omega_c T / 2) \cot \theta \end{aligned} \quad (\text{G5})$$

The distance $y''_2 - y''_1$ can be obtained as (see Fig. 34b and cf. (D11)) :

$$y''_2 - y''_1 = 2 \frac{v_c}{\omega_c} \sin \frac{\omega_c T}{4} \sin \left(\alpha + \frac{\omega_c T}{4} \right) \quad (\text{G6})$$

Substituting (G5) and (G6) into (G3), we obtain :

$$v_c \sin \left(\alpha + \frac{\omega_c T}{4} \right) \cos \left(\frac{\omega_c T}{4} \right) = - \frac{d\omega_c \tan \theta}{2 \cos \theta} \frac{\cot \left(\frac{\omega_c T}{4} \right)}{\tan^2 \theta + \frac{\omega_c T}{4} \cot (\omega_c T)} \quad (\text{G7})$$

The periodicity of the orbit requires, that the distance traveled by the electron in the drift frame of reference between two successive collisions with the collector barrier $x''_2 - x''_1$ (see Fig. 34b) is equal to the displacement of this coordinate system $v_d T$, which yields

$$v_c \cos \left(\alpha + \frac{\omega_c T}{4} \right) \sin \left(\frac{\omega_c T}{4} \right) = v_d \frac{\omega_c T}{4} \quad (\text{G8})$$

Using Eqs. (G7) and (G8), one can easily obtain

$$\begin{aligned} v_{y',1}^+ &= v_c \sin \alpha = -v_d \frac{\omega_c T}{4} - \frac{d\omega_c \tan \theta}{2 \cos \theta} \frac{\cot \left(\frac{\omega_c T}{4} \right)}{\tan^2 \theta + \frac{\omega_c T}{4} \cot \left(\frac{\omega_c T}{4} \right)} \\ v_{x',1}^+ &= -v_d + v_c \sin \alpha = -v_d \left(1 - \frac{\omega_c T}{4} \cot \left(\frac{\omega_c T}{4} \right) \right) - \frac{d\omega_c \tan \theta}{2 \cos \theta} \frac{1}{\tan^2 \theta + \frac{\omega_c T}{4} \cot \left(\frac{\omega_c T}{4} \right)} \end{aligned} \quad (\text{G9})$$

Substituting (G9) into the equation for energy conservation

$$v_{x'}^2 + v_{y'}^2 + v_{z'}^2 = 1$$

and using (D2), we finally obtain :

$$\beta^2 = \left(\frac{\omega_c T}{2} \right)^2 \left(1 + \frac{\beta^2}{\gamma (\omega_c T)^2} \frac{1 - f(\omega_c T)}{1 - \cos^2 \theta f(\omega_c T)} \right)^2 + 4 \sin^2 \theta f^2(\omega_c T) \left(1 + \frac{\beta^2}{16 \gamma f(\omega_c T) (1 - \cos^2 \theta f(\omega_c T))} \right)^2 \quad (\text{G10})$$

which is exactly the Eq. (59). To obtain the period of the period-1 orbits from this equation, one has solve it together with the condition

$$(\tilde{v}_e)_z^- = \frac{2 \cos \theta}{\beta} \frac{\omega_c T}{4} + \frac{\beta \cos \theta}{2 \gamma \omega_c T} \frac{1 - f(\omega_c T)}{1 - \cos^2 \theta f(\omega_c T)} > 0 \quad (\text{G11})$$

which ensures that v_z just before the collision with the emitter is positive and allows to select the physically meaningful roots.

APPENDIX H: THE MONODROMY MATRIX FOR A GENERAL PERIODIC ORBIT IN THE DBM

In this Appendix we consider the monodromy (stability) matrix for a general orbit in the double-barrier model. As in our stability analysis for the periodic orbits in the SBM, the velocity at each collision with the barriers and the time interval between successive collisions for the periodic orbit are considered already known.

By definition, the monodromy matrix is the linearization of the Poincaré map around the periodic orbits. It is straightforward to show, that since the evolution of the electron velocity *between* successive collisions is exactly the same in both SBM and DBM, and any collision only reverses the sign of z -component of the velocity, the monodromy matrix will still be given by Eqs. (C4) and (C3), where the index k now labels all successive collisions of the electron (with *both* emitter and collector barriers).

Note, that the components of the matrices M_k contain terms proportional to $1/(\tilde{v}_z)$. Therefore, if at any of the collisions with the emitter barrier the z component of the velocity goes to zero (as it happens in a cusp bifurcation), the components of the matrix M_k diverge, which leads to the divergence of the trace of the monodromy matrix. An additional consequence of this behaviour is that by continuity any orbit with sufficiently small v_z at at least one of the collisions of the emitter barrier per period *must* be unstable.

- ¹ W. R. S. Garton and F. S. Tomkins, *Astrophys. J.* **158**, 839 (1969).
- ² A. Holle et al., *Phys. Rev. Lett.* **61**, 161 (1988).
- ³ M.C.Gutzwiller *Chaos in Classical and Quantum Mechanics* (Springer-Verlag, New York, 1990)
- ⁴ M.L. Du and J. B. Delos, *Phys. Rev. Lett.* **58**, 1731 (1987); *Phys. Rev. A* **38**, 1896 (1988); *Phys. Rev. A* **38**, 1913 (1988).
- ⁵ R. A. Jalabert, H. U. Baranger and A. D. Stone, *Phys. Rev. Lett.* **65**, 2442 (1990).
- ⁶ C. M. Marcus, A. J. Rimberg, R. M. Westervelt, P. F. Hopkins and A. C. Gossard, *Phys. Rev. Lett.* **69**, 506 (1992).
- ⁷ D. Weiss, K. Richter, A. Menschig, R. Bergmann, H. Schweizer, K. von Klitzing, and G. Weimann, *Phys. Rev. Lett.*, **70**, 4118 (1993).
- ⁸ G. Hackenbroich, F. von Oppen, *Europhysics-Letters*, **29**, 151 (1995); *Zeitschrift fur Physik B (Condensed-Matter)*, **97**, 157 (1995); *Annalen der Physik*, **5**, 696 (1996);
- ⁹ T. M. Fromhold, L. Eaves, F. W. Sheard, M. L. Leadbeater, T. J. Foster, and P. C. Main, *Phys. Rev. Lett.*, **72**, 2608 (1994); A. Fogarty, T. M. Fromhold, L. Eaves, F. W. Sheard, M. Henini, T. J. Foster, P. C. Main, and G. Hill, *Superlattices and Microstructures*, **15**, 287 (1994); T. M. Fromhold, L. Eaves, F. W. Sheard, T. J. Foster, M. L. Leadbeater, P. C. Main, *Physica B*, **201**, 367 (1994); T. M. Fromhold, M. L. Leadbeater, L. Eaves, T. J. Foster, F. W. Sheard, P. C. Main, P. J. McDonnell, and A. Fogarty, *Semiconductor Science and Technology*, **9**, 488 (1994); T. M. Fromhold, M. L. Leadbeater, L. Eaves, T. J. Foster, P. C. Main, F. W. Sheard, *Surface Science*, **305**, 511 (1994)
- ¹⁰ P. B. Wilkinson, T. M. Fromhold, L. Eaves, F. W. Sheard, N. Miura, and T. Takamasu, *Nature*, **380**, 608 (1996); *Surface-Science*, **361 - 362**, 696 (1996); T. M. Fromhold, P. B. Wilkinson, F. W. Sheard, L. Eaves, J. Miao, and G. Edwards, *Phys. Rev. Lett.*, **75**, 1142 (1995).
- ¹¹ G. Muller, G. S. Boebinger, H. Mathur, L. N. Pfeiffer, and K. W. West, *Phys. Rev. Lett.*, **75**, 2875 (1995); G. S. Boebinger, G. Muller, H. Mathur, L. N. Pfeiffer, K. N. West, *Surface Science*, **361 - 362**, 742 (1996).
- ¹² Actually we shall see that the current experimental system, which we describe by the double-barrier model introduced below, is not a standard KAM system due to a discontinuity in its classical mechanics which is important for the periodic orbit theory and is addressed in detail in the text.
- ¹³ E. Narimanov and A. D. Stone, next paper.
- ¹⁴ D.L.Shepelyansky and A.D.Stone, *Phys. Rev. Lett.* **74**, 2098 (1995)
- ¹⁵ J. M. Greene, R. S. MacKay, F. Vivaldi, M. J. Feigenbaum, *Physica* **3D**, 468 (1981).
- ¹⁶ B.V.Chirikov, *Phys. Rep.* **52**, 263 (1979).
- ¹⁷ T. M. Fromhold, P. B. Wilkinson, F. W. Sheard and L. Eaves, Comment on "Precursors and Transitions to Chaos in a Quantum Well in a Tilted Magnetic Field" by G. Muller *et al*, to be published in *Phys. Rev. Lett.*
- ¹⁸ T. M. Fromhold, A. Fogarty, L. Eaves, F. W. Sheard, M. Henini, T. J. Foster, P. C. Main, and G. Hill, *Phys. Rev. B*, **51**, 18029 (1995)
- ¹⁹ T.S.Monteiro *et al.*, *Phys. Rev. E* **53**, 3369 (1996).
- ²⁰ T. S. Monteiro, and D. Delande, submitted to *Phys. Rev. Lett.*
- ²¹ A.J.Lichtenberg and M.A.Lieberman *Regular and Chaotic dynamics* (Springer-Verlag, New York, 1994)
- ²² L.Reichl *The Transition to Chaos in Conservative Classical Systems : Quantum Manifestations* (Springer-Verlag, New York, 1992).
- ²³ F. Haake *Quantum Signatures of Chaos* (Springer-Verlag 1991)
- ²⁴ The kicked - top map in the standard form in variables $(X_n, Y_n, Z_n; \alpha, \lambda)^{23}$ is identical to the approximate SBM mapping, when $X_n \equiv (\tilde{v}_{x'})_n, Y_n \equiv (\tilde{v}_{y'})_n, Z_n \equiv (\tilde{v}_{z'})_n, \alpha \equiv 2\theta, \lambda \equiv \frac{\beta}{\cos \theta}$
- ²⁵ With a slightly different doping profile the bottom of the well could be raised above the emitter state at zero bias allowing an experimental study of the pure DBM.
- ²⁶ L. A. Bunimovich, *Func. Anal. Appl.* **8**, 254 (1974).
- ²⁷ J.-M. Mao and J. B. Delos, *Phys. Rev. A* **45**, 1746 (1992)
- ²⁸ K. R. Meyer, *Trans. Am. Math. Soc.* **149**, 95 (170).
- ²⁹ R. DeVogelaere, in *Contributions to the Theory of Nonlinear Oscillations*, Vol. IV, edited by S. Lefschetz (Princeton University Press, 1958); R. S. MacKay, in *Long Time Prediction in Dynamics*, edited by W. Horton, L. E. Reichl, and V. Szebehely (J. Wiley and Sons, New York, 1983)
- ³⁰ The unperturbed system ($\theta = 0$) represents the limiting behavior of the tilted well only if the chaos parameter $K \sim \beta\theta \rightarrow 0$. The parameter β_{b3} , corresponding to the value of β at the appearance of the $(2)_s^{+k}$ orbit, diverges at $\theta \rightarrow 0$, which resolves what seems to be a contradiction.
- ³¹ . The following simple qualitative argument can illustrate the origin of this property. When the total energy is just a little above the potential drop between the barriers eV ($\gamma - 1 \ll 1$), then the electron returns to the collector barrier with very small kinetic energy. Therefore, the energy exchange between cyclotron and longitudinal degrees of freedom at the emitter wall, if takes place, results in a substantially smaller energy transfer between cyclotron and longitudinal degrees of freedom, than the energy exchange at the collector barrier for a similar angle of incidence. Therefore, it is intuitively clear, that the energy exchange at the emitter barrier alone can not compensate for the energy exchange at the collector wall, and for the period-1 emitter orbits are expected to be non-mixing.
- ³² A nonzero y component of the velocity at the point of collision necessarily leads to a nonzero energy exchange between cyclotron and longitudinal motion at the emitter wall, while for the $(0, 2)^+$ orbit (which at the cups bifurcation is degenerate

with an emitter orbit) the cyclotron velocity must not be changed between successive collisions with the collector barrier.

³³ G. S. Boebinger, E. E. Narimanov, and A. D. Stone, Reply to the Comment on “Precursors and Transitions to Chaos in a Quantum Well in a Tilted Magnetic Field” by G. Muller *et al*, to be published in Phys. Rev. Lett.

³⁴ E. J. Heller, Phys. Rev. Lett **53**, 1515 - 1518 (1984).

³⁵ E. B. Bogomolny, Physica D **31**, 169 - 189 (1988).

³⁶ M. V. Berry, Proc. roy. Soc. Lond. A **423**, 219 - 231 (1989).

TABLE I. Period-1 and period-2 orbits in the SBM

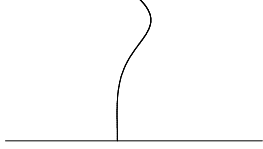
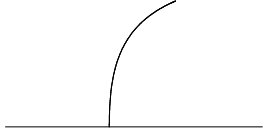
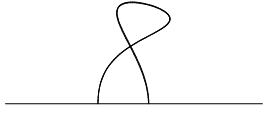
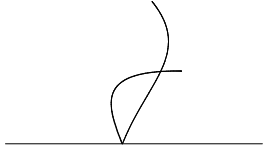
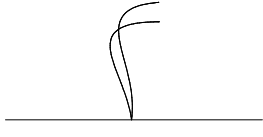
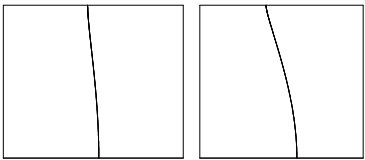
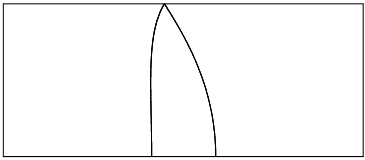
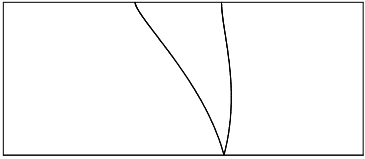
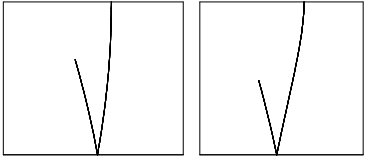
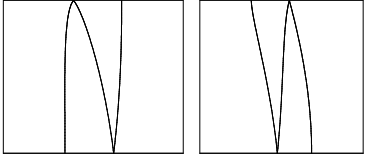
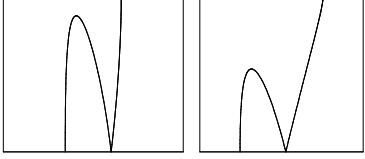
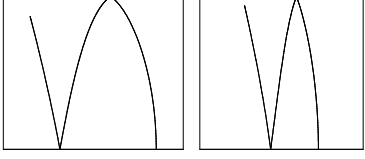
orbit	y-z projection	origin	initial stability
$(1)^+$		TB with $(1)^-$	stable
$(1)^-$		TB with $(1)^+$	unstable
$(2)^-$		PDB of $(1)^+$	stable
$(2)^+$		IPDB of $(1)^+$	unstable
$(2)^*$		PDB of $(1)^+$	stable

TABLE II. Relevant periodic orbits in the DBM

orbit	y-z projection	"birth" \leftrightarrow "death"
$(1,1)^\pm$		CB \leftrightarrow TB
$(2,2)^-$		CB \leftrightarrow PDB
$(2,2)^{+0}$		CB \leftrightarrow PDB
$(1,2)^\pm$		CB \leftrightarrow TB
$(3,3)^\pm$		CB \leftrightarrow TB
$(1,3)^\pm$		CB \leftrightarrow TB
$(2,3)^\pm$		CB \leftrightarrow TB

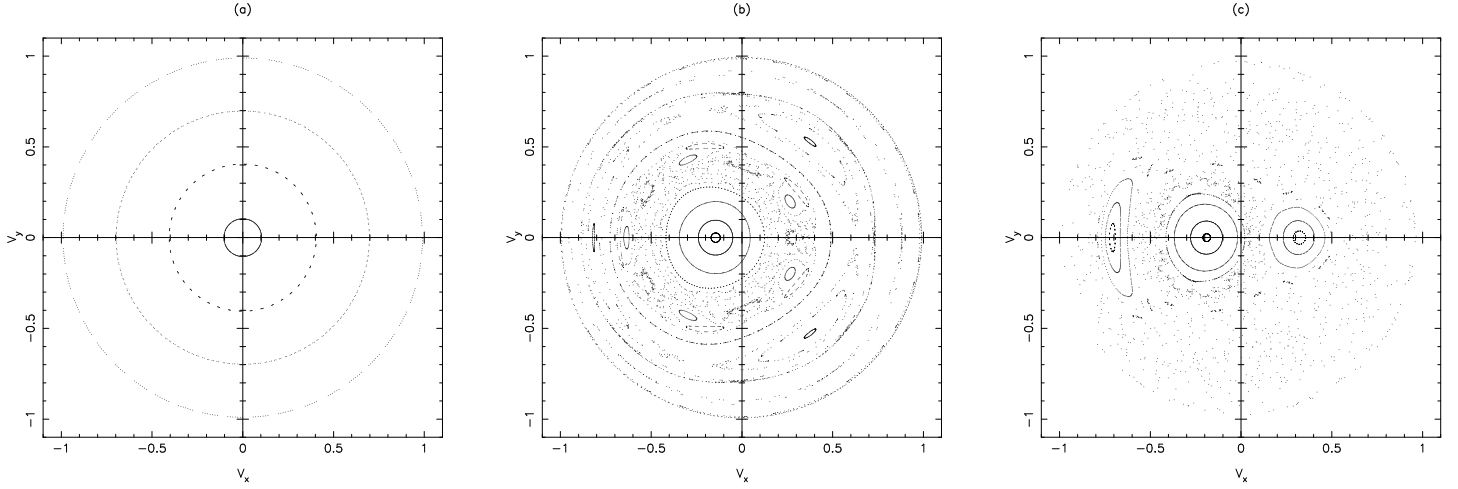


FIG. 1. Three Poincaré surfaces of section for experimentally relevant $\gamma = 1.17$ at : (a) $\theta = 0^\circ$, $\beta = 2$, (b) $\theta = 20^\circ$, $\beta = 3.2$, (c) $\theta = 20^\circ$, $\beta = 4$.

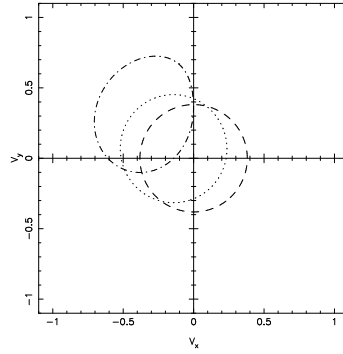


FIG. 2. The critical boundary, separating initial conditions such that the electron will reach the emitter barrier before the next collision with the collector wall (region enclosed by the critical boundary) from those when the electron returns to the collector wall without striking the emitter barrier (the region outside the critical boundary). $\gamma = 1.17$, and (a) $\theta = 0^\circ$ (dashed line), (b) $\theta = 15^\circ$, $\beta = 3$. (dotted line), (c) $\theta = 30^\circ$, $\beta = 5$ (dashed-dotted line).

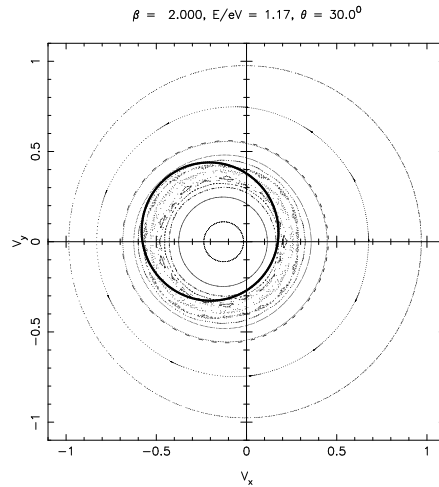


FIG. 3. The Poincaré surface of section for $\gamma = 1.17$, and $\beta = 2$, $\theta = 30^\circ$. The chaotic region near the critical boundary (thick solid line) is the “chaotic halo”, created by the nonanalyticity of the map.

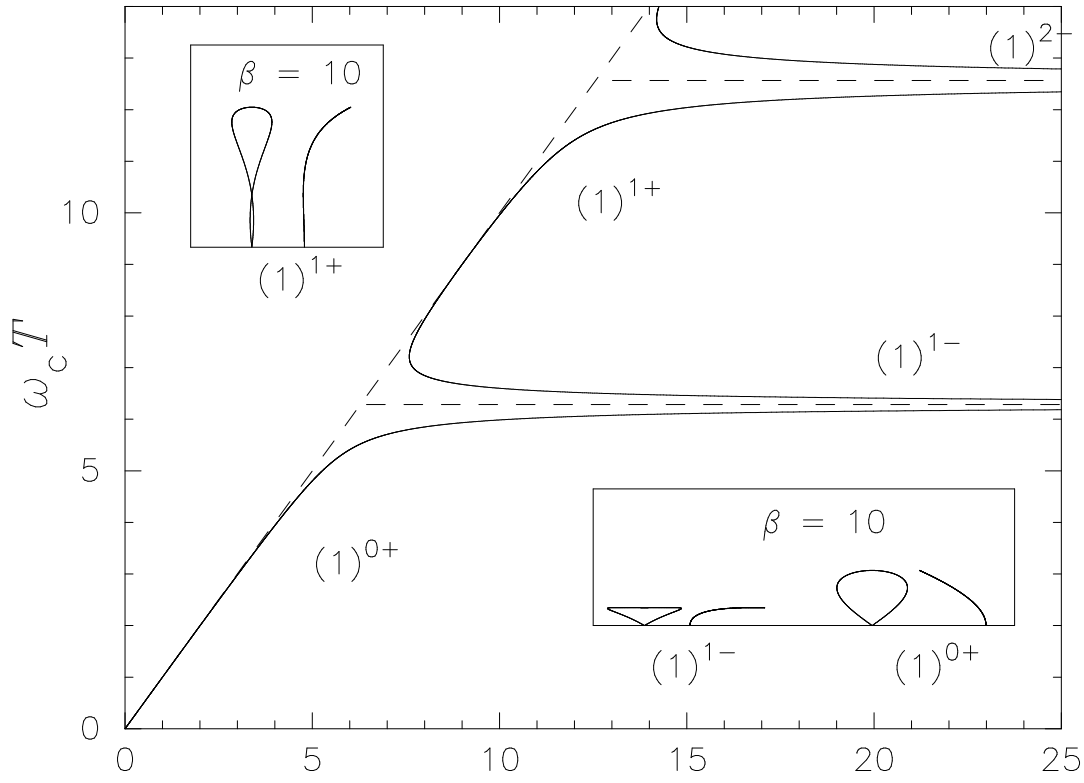


FIG. 4. Periods of one-bounce orbits as functions of β for the tilt angle $\theta = 11^\circ$. The dashed lines corresponds to the periods of one bounce orbits at zero tilt angle. The insets show the $y-z$ projections of the three existing one-bounce orbits at $\beta = 10$.

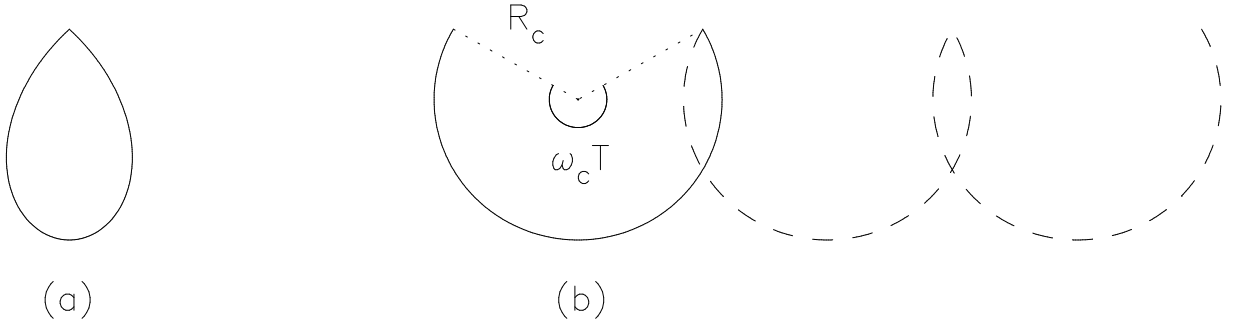


FIG. 5. A single-bounce orbit projected onto the (x', y') plane (a) and (x'', y'') plane of the “drifting” frame of reference (b).

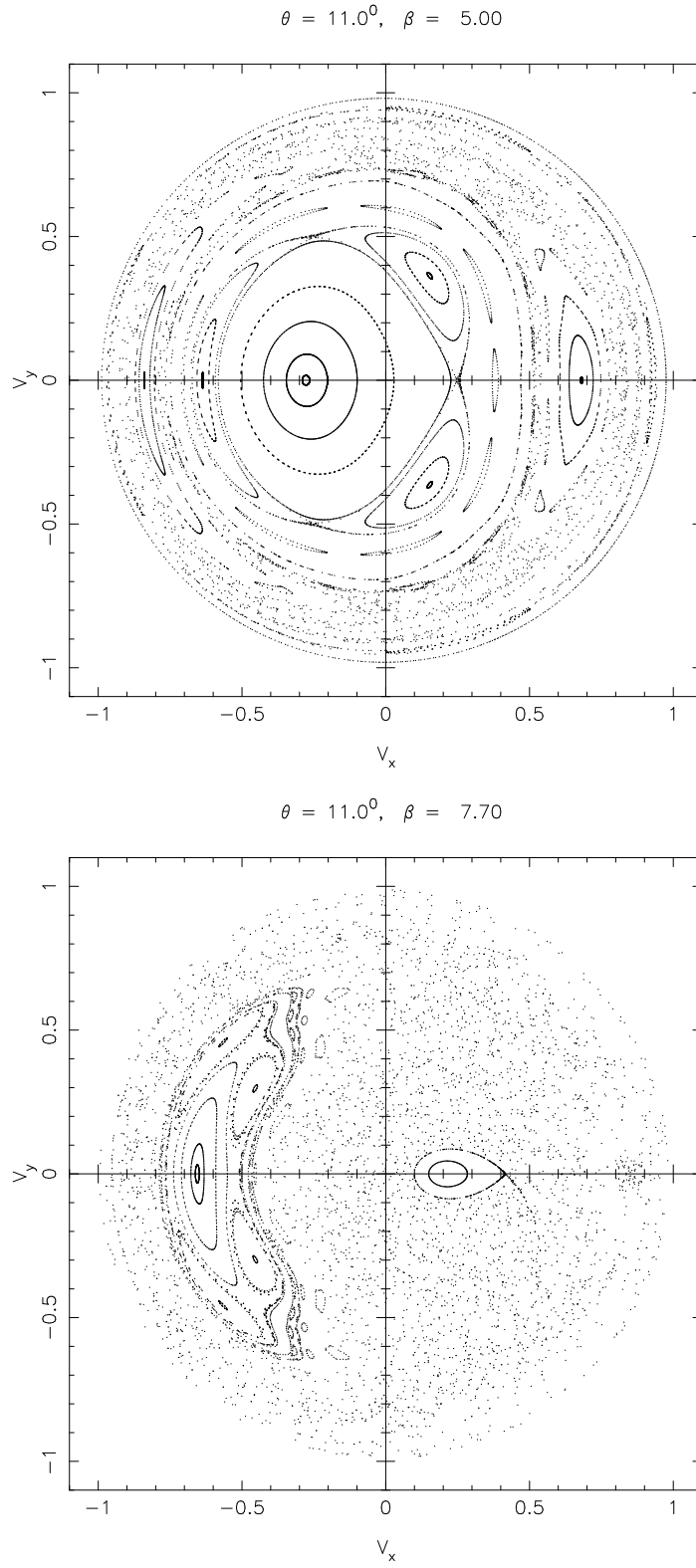


FIG. 6. Poincaré surface of section for the single-barrier model for $\theta = 11^\circ$ and (a) $\beta = 5$ (as in the unperturbed system, the single-bounce orbit $((1)^{+(0)})$ is still surrounded by a large stable island, but has nonzero x -component of the total velocity at the collision with the collector barrier), and (b) $\beta = 7.7$ (the $(1)^{+0}$ orbit is still stable, but moved to the periphery of the surface of section; a tangent bifurcation has just produced two new single-bounce orbits : stable $(1)^{+(1)}$ near the origin, which now takes the role of the TO, and unstable $(1)^{-(1)}$, which produces an elongated flow pattern near the stable island of $(1)^{+(1)}$).

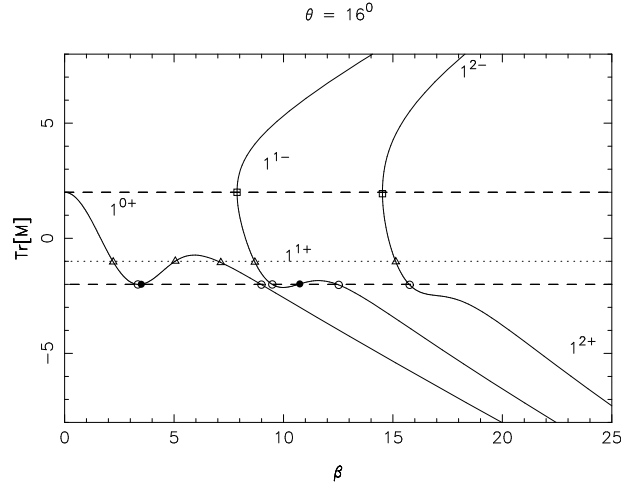


FIG. 7. Trace of the monodromy matrix for single-bounce orbits $(1)^{(0)+}$, $(1)^{(1)+}$, $(1)^{(1)-}$, $(1)^{(2)+}$, $(1)^{(2)-}$ for $\theta = 16^\circ$. The dotted line represents the condition for the 1 : 3 resonance, the dashed lines show the boundaries of the stability region $\text{Tr}[M] \leq 2$. Open circles show the locations of the direct PDBs, the solid circles correspond to inverse PDBs, open triangles represent 1 : 3 resonances, squares represent tangent bifurcations.

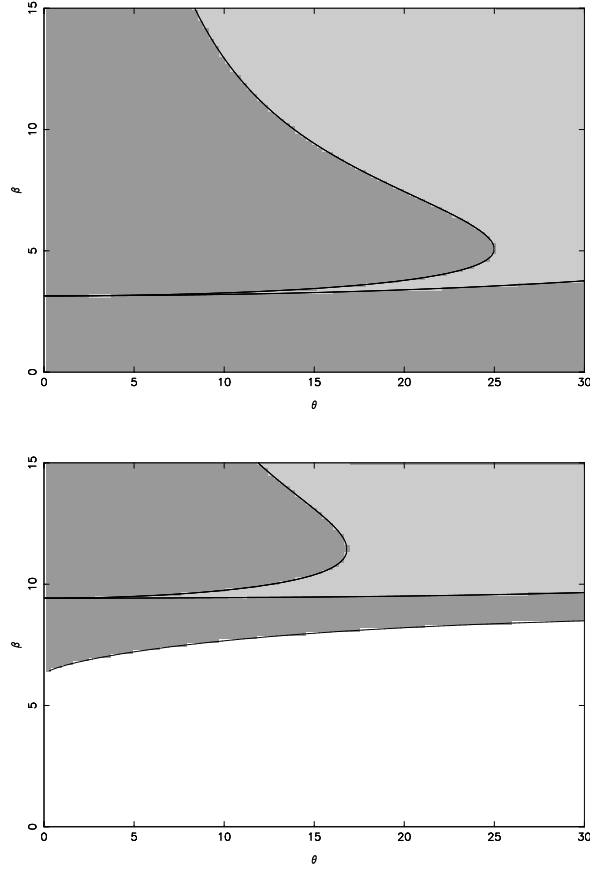


FIG. 8. Regions of existence (shaded areas) of one-bounce orbits $(1)^{(0)+}$ (a) and $(1)^{(1)+}$ (b) in the (θ, β) plane. Dark and light shading correspond to stable and unstable regions respectively.

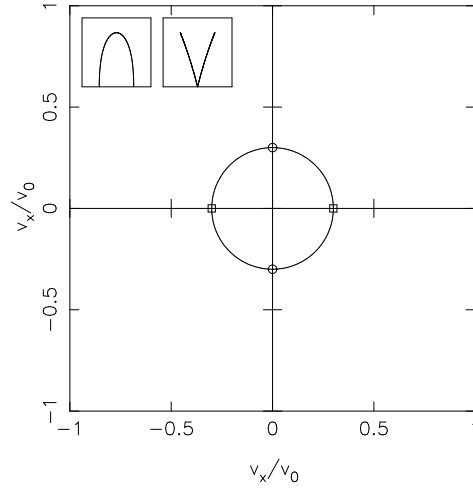


FIG. 9. Torus of two-bounce orbits in the Surface of Section. Marked are the only “self-retracing” (in the $y - z$ plane) two-bounce orbits : (a) the orbit with $v_y = 0$ at collisions, which evolves into the non-mixing two-bounce orbit $(2)^-$, and (b) the orbit with $v_x = 0$ at collisions - which becomes the self-retracing mixing orbit $(2)^+$. Insets show the $y - z$ projections of these orbits.

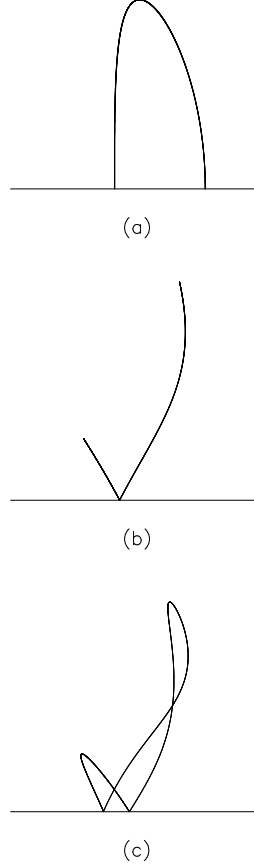


FIG. 10. Examples of the different types of period-2 orbits, projected onto (x, z) and (y, z) planes : a non-mixing orbit (a), a self-retracing mixing orbit (b) and a non-self-retracing mixing orbit (c).

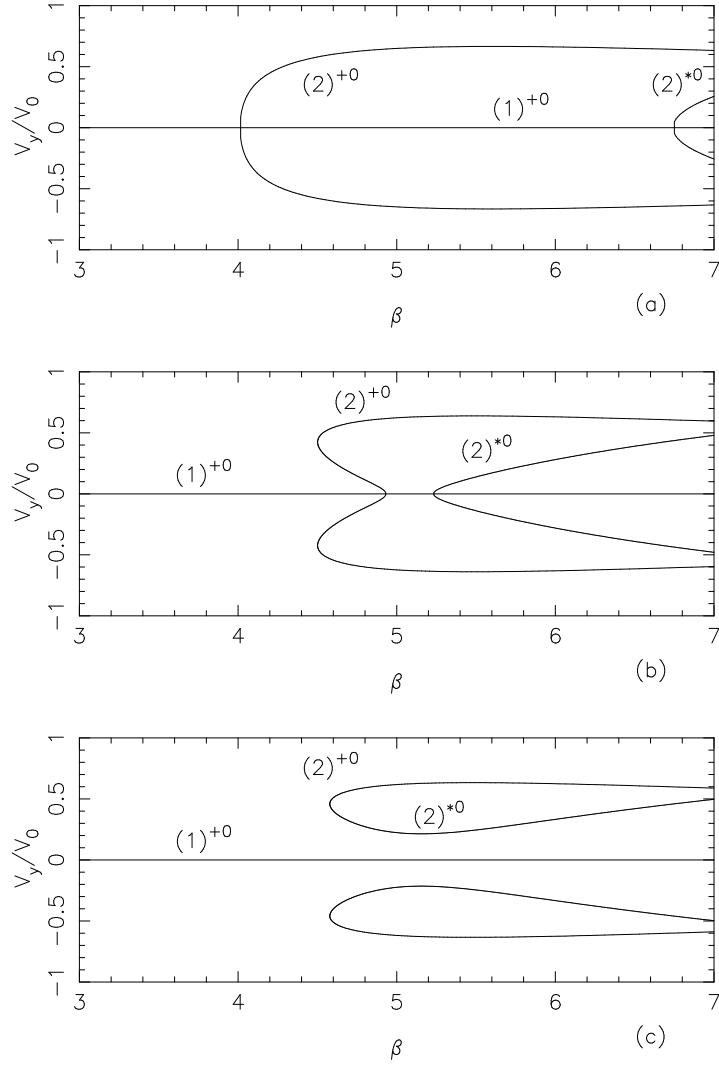


FIG. 11. Bifurcation diagrams in the coordinates (β, \tilde{v}_y) for the period-2 mixing orbits, related to the bifurcations of the single - bounce orbits. The two branches with non-zero \tilde{v}_y correspond to the two-bounce mixing orbits $(2)^{+(0)}$ and $(2)^{*(0)}$, while the horizontal line represents the single-bounce orbit $(1)^{+(0)}$. The non-mixing period-2 orbit $(2)^{-(0)}$ has $v_y = 0$ at each of the points of collision and cannot be seen in this diagram. For a small tilt angle the period-2 orbits are born in period-doubling bifurcations - see panel (a). When $\theta > \theta_k$ the mixing period-2 orbits are born in a tangent bifurcation - see panel (c). The transformation from the two types of behavior cannot happen in a single step. If it were possible, then at the critical angle *two* new mixing two-bounce orbits were created at the location of the single-bounce orbit, which can *not* happen in a generic conservative 2D system. The alternative is provided by the following two-step process. First, at some critical angle $\theta_k^0 < \theta_k$ the behavior of the first to appear mixing orbit $(2)^{-(k)}$ is changed, as is shown in the bifurcation diagram at the panel (b). When $\theta_k^0 < \theta < \theta_k$, the unstable orbit $(2)^{+(k)}$ appears in a tangent bifurcation with a new self-retracing mixing stable period-2 orbit, which is soon to be absorbed by the single-bounce orbit in an *inverted* period-doubling bifurcation, while the qualitative behavior of the stable $(2)^{*(k)}$ orbit remains unchanged. As the tilt angle is increased, the interval of stability of the single-bounce orbit shrinks, while the interval of existence of the auxiliary mixing orbit increases. At the critical tilt angle the inverted and standard period-doubling bifurcations merge and annihilate each other, so that at greater values of the tilt angle the mixing period-2 orbit are no longer directly related to the single-bounce orbit - see panel (c).

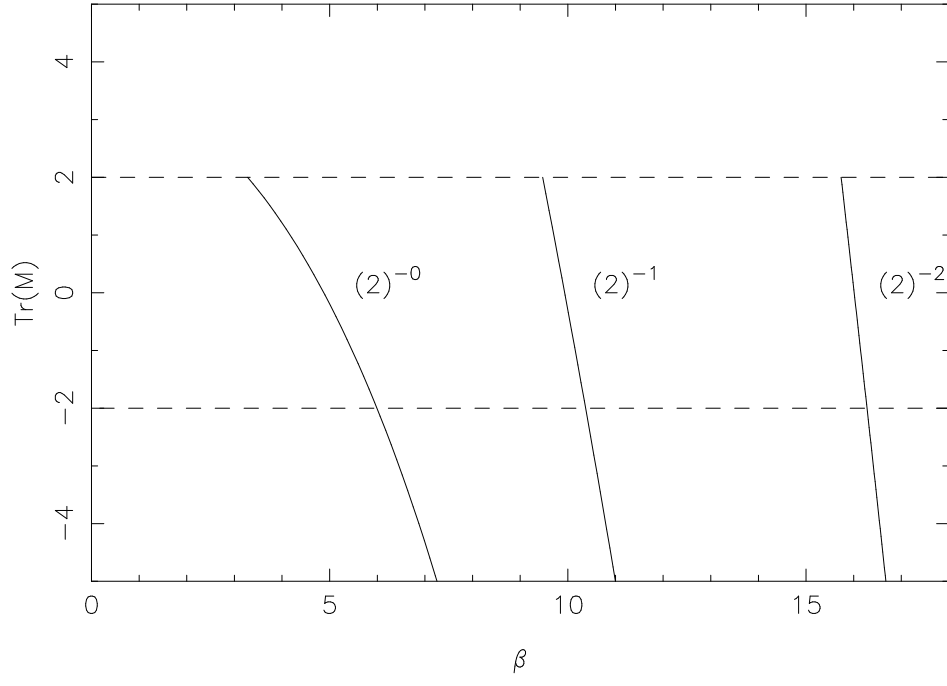


FIG. 12. Trace of monodromy matrix as a function of β for different non-mixing two-bounce periodic orbits : $(2)^{+0}$, $(2)^{+1}$, $(2)^{+2}$ for $\theta = 15^\circ$.

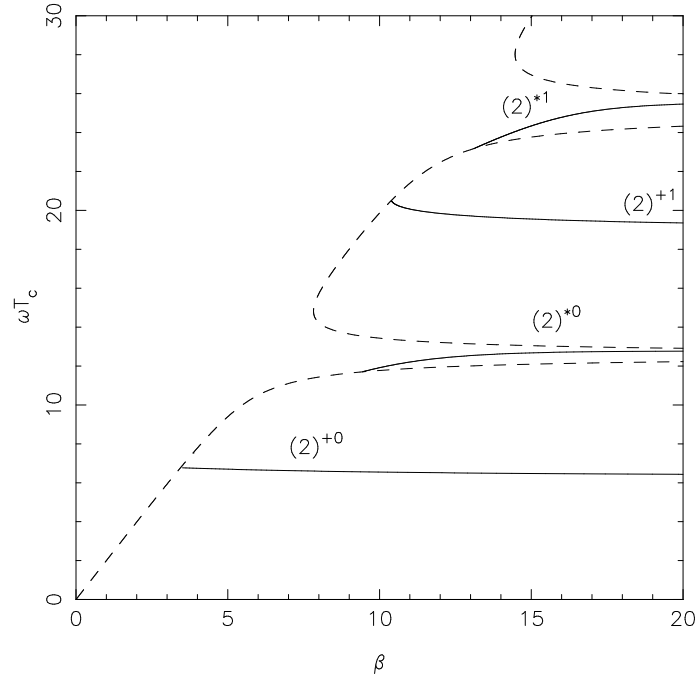


FIG. 13. Periods of the self-retracing mixing two-bounce orbits $(2)^{+(0)}$, $(2)^{*(0)}$, $(2)^{+(1)}$, and $(2)^{*(1)}$, related to the bifurcations of the single-bounce periodic orbits as functions of β . The tilt angle is $\theta = 15^\circ$. The dashed lines show the (scaled) time intervals of two repetitions of single-bounce orbits (i.e. twice the period of single-bounce orbits).

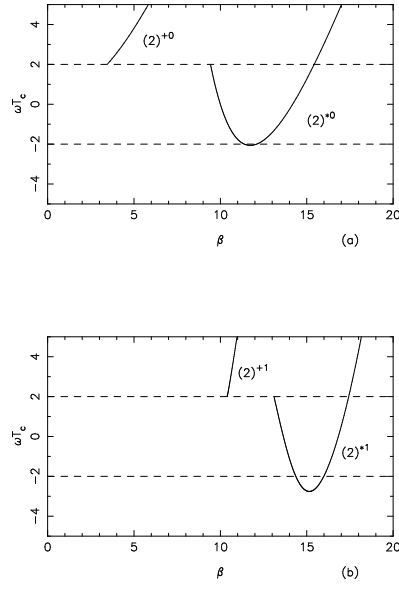


FIG. 14. Trace of the monodromy matrix as a function of β for mixing two-bounce orbits (a) $(2)^{+(0)}$ and $(2)^{*(0)}$, $(2)^{+(1)}$ and $(2)^{*(1)}$. The tilt angle is $\theta = 15^\circ$.

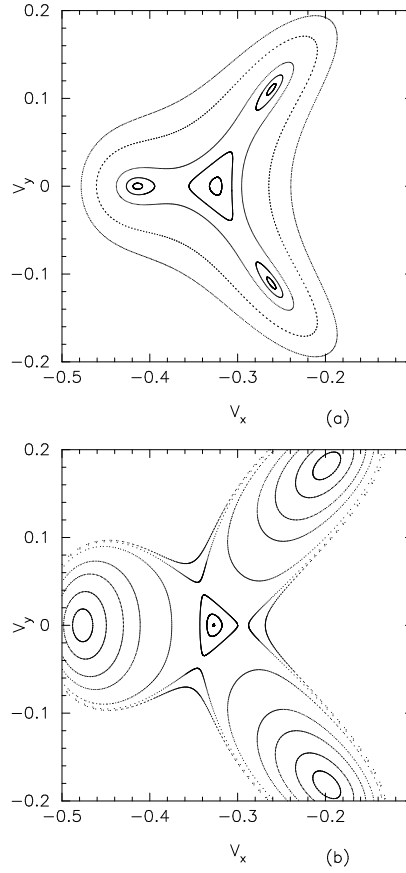


FIG. 15. Surface of Section near the one-bounce periodic orbit $(1)^{+(0)}$ close to its $1:3$ resonance and the corresponding touch-and-go bifurcation of the orbits $(3)_1^{(1)}$: (a) just before and (b) soon after the touch-and-go bifurcation.

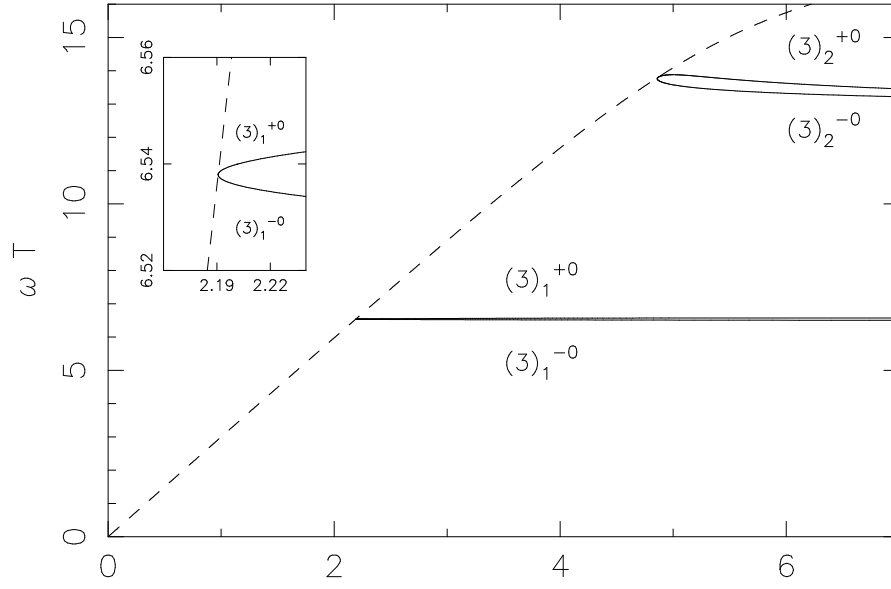


FIG. 16. The periods of the three-bounce orbits $(3)_1^{\pm 0}$ and $(3)_2^{\pm 0}$ vs. β for tilt angle for $\theta = 11^\circ$ (solid lines). The dashed line represents the period of single-bounce orbit $(1)^{+(0)}$, multiplied by 3.

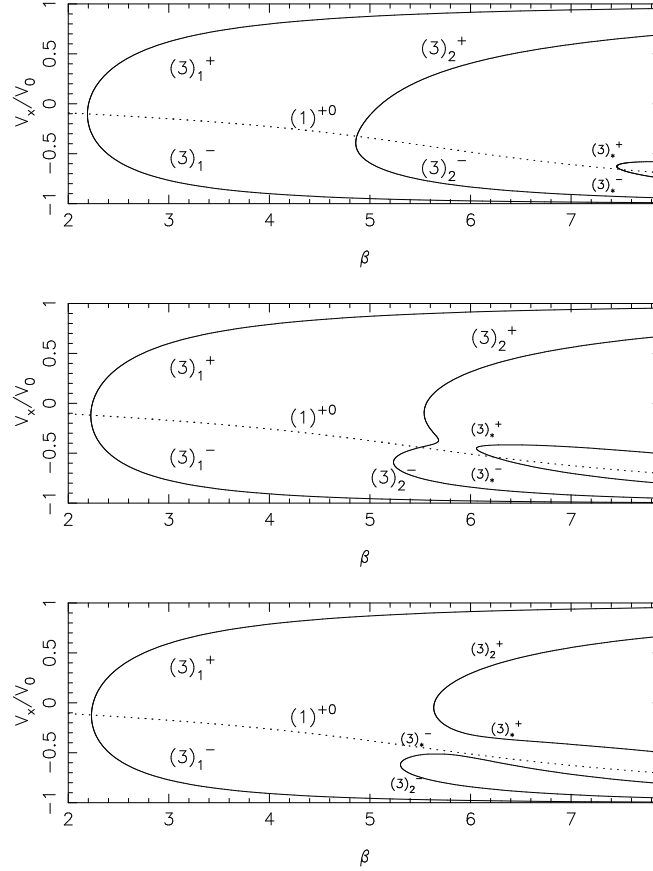


FIG. 17. The bifurcation diagrams of the self-retracing three-bounce orbits in three different regimes (see text). The vertical axis represents the x component of the scaled velocity of the electron at the point of collision with $\tilde{v}_y = 0$. The dotted line represents the single-bounce orbit. Note the exchange of partners bifurcation between (b) and (c).

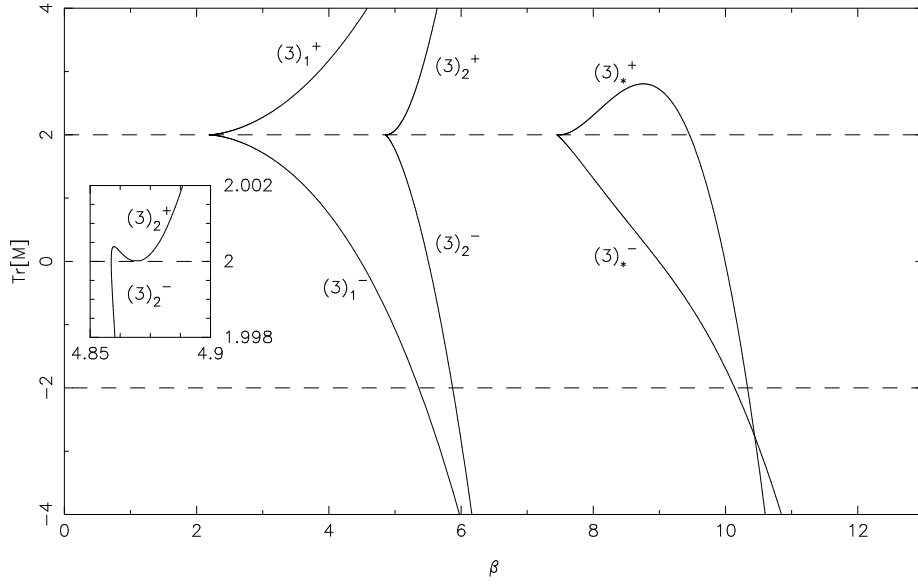


FIG. 18. Trace of the monodromy matrix as a function of β for self-retracing three-bounce orbits. The inset shows the behavior of $\text{Tr}[M]$ near the “touch-and-go” bifurcation.

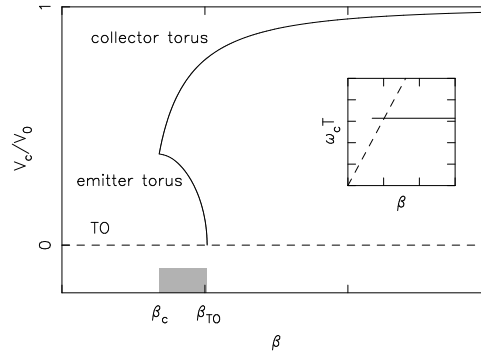


FIG. 19. The scaled cyclotron velocity for the resonant tori ($n = 1$, $k = 1$) as function of β at zero tilt angle; $\gamma = 1.2$, number of cyclotron rotations per period $m = 1$. The horizontal line $\tilde{v}_c = 0$ corresponds to the traversing orbit.

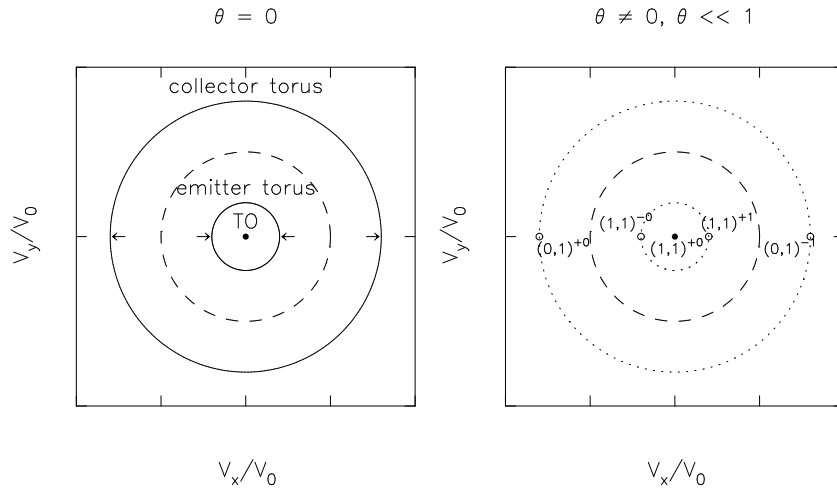
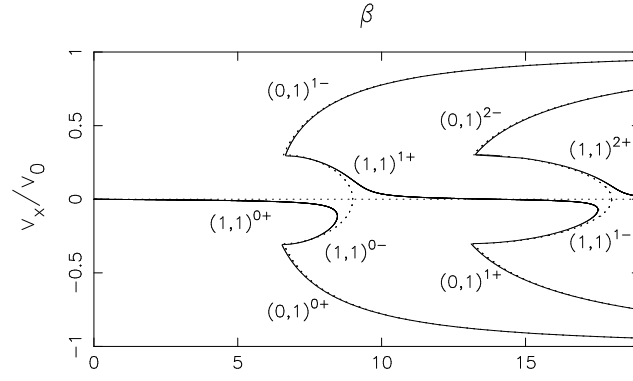
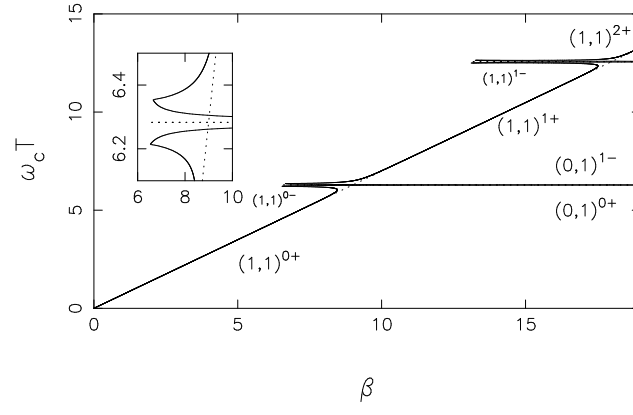
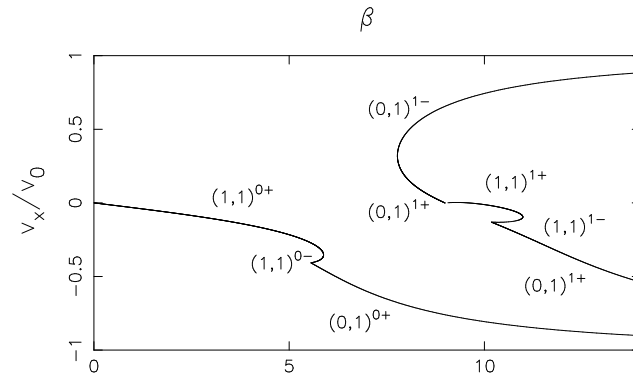
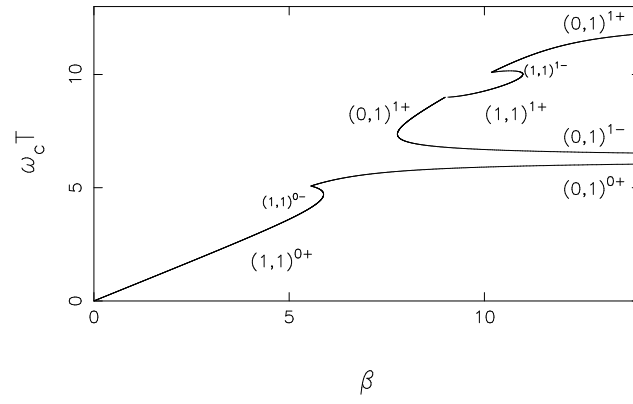


FIG. 20. A schematic representation of (a) the two resonant tori of the period-1 orbits at $\theta = 0^\circ$ and (b) the surviving orbits at $\theta \ll 1$.

(a)



(b)



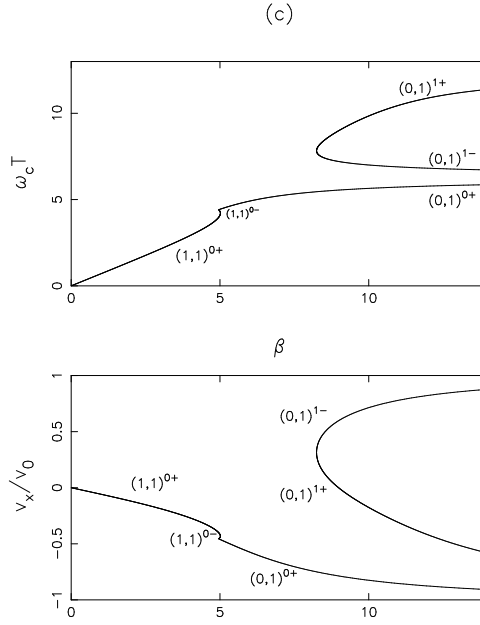


FIG. 21. The scaled period $\omega_c T$ as function of β and the corresponding bifurcation diagrams for the period-1 orbits in the double-barrier model at zero tilt angle. The tilt angle (a) $\theta = 0.5^\circ$, (b) 11° , (c) 20° . $\gamma = 1.17$. The vertical axis in the bifurcation diagrams represents the scaled cyclotron velocity \tilde{v}_c (a) or to the x component of the scaled velocity of the electron at the point of collision with the collector barrier.

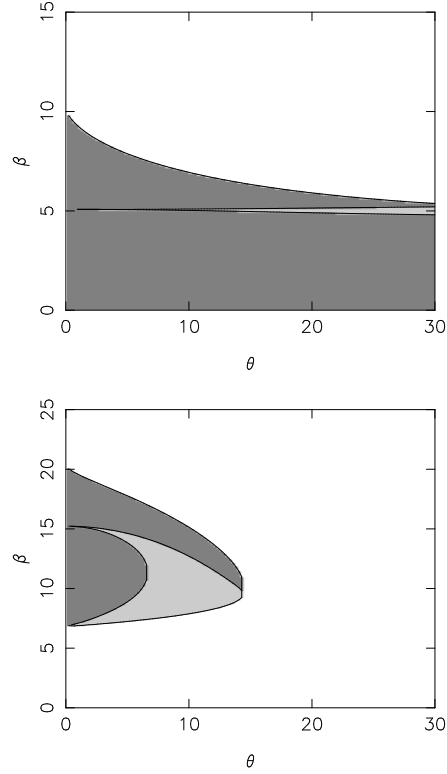


FIG. 22. The intervals of existence of the period-1 “emitter” orbits shown as shaded areas in the (θ, β) plane for (a) $(1,1)^{(0)-}$, (b) $(1,1)^{(0)+}$, (c) $(1,1)^{(1)-}$, (d) $(1,1)^{(1)+}$. Dark and light shading represent existing stable and unstable periodic orbits respectively.

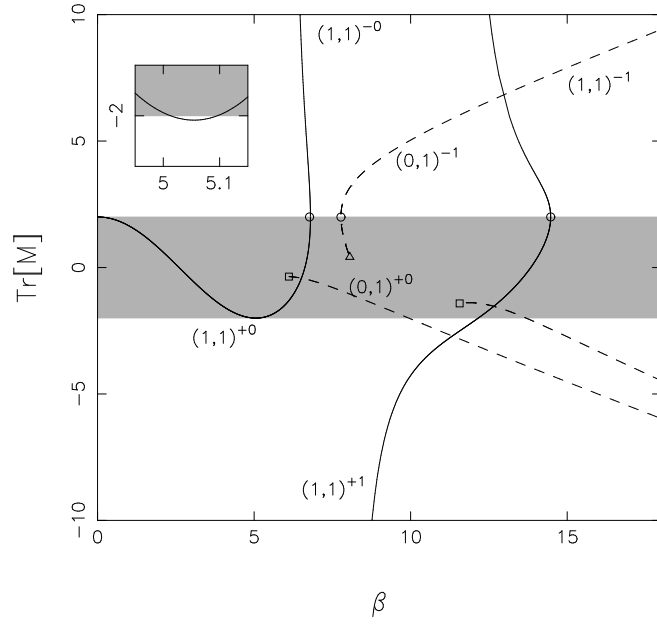


FIG. 23. Trace of monodromy matrix of the period-1 orbits of the first two intervals at $\theta = 11^\circ$, $\gamma = 1.17$. The tangent bifurcations, cusp bifurcations and connectivity transitions are labeled by open circles, open squares and open triangles respectively. Shaded area corresponds to the stable region.

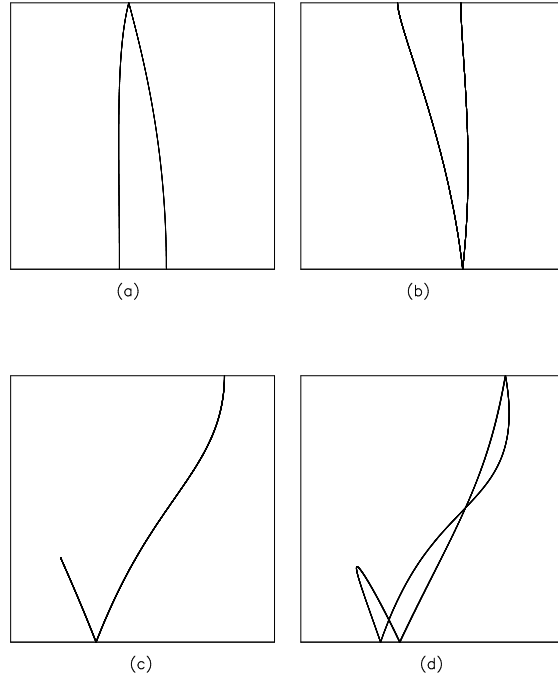


FIG. 24. Examples of the different types of period-2 orbits in the DBM, projected onto (y, z) planes : (a) a $(2, 2)^-$ orbit, (b) a $(2, 2)^+$ orbit, (c) a self-retracing $(1, 2)$ orbit, (d) a non-self-retracing $(1, 2)$ orbit. .

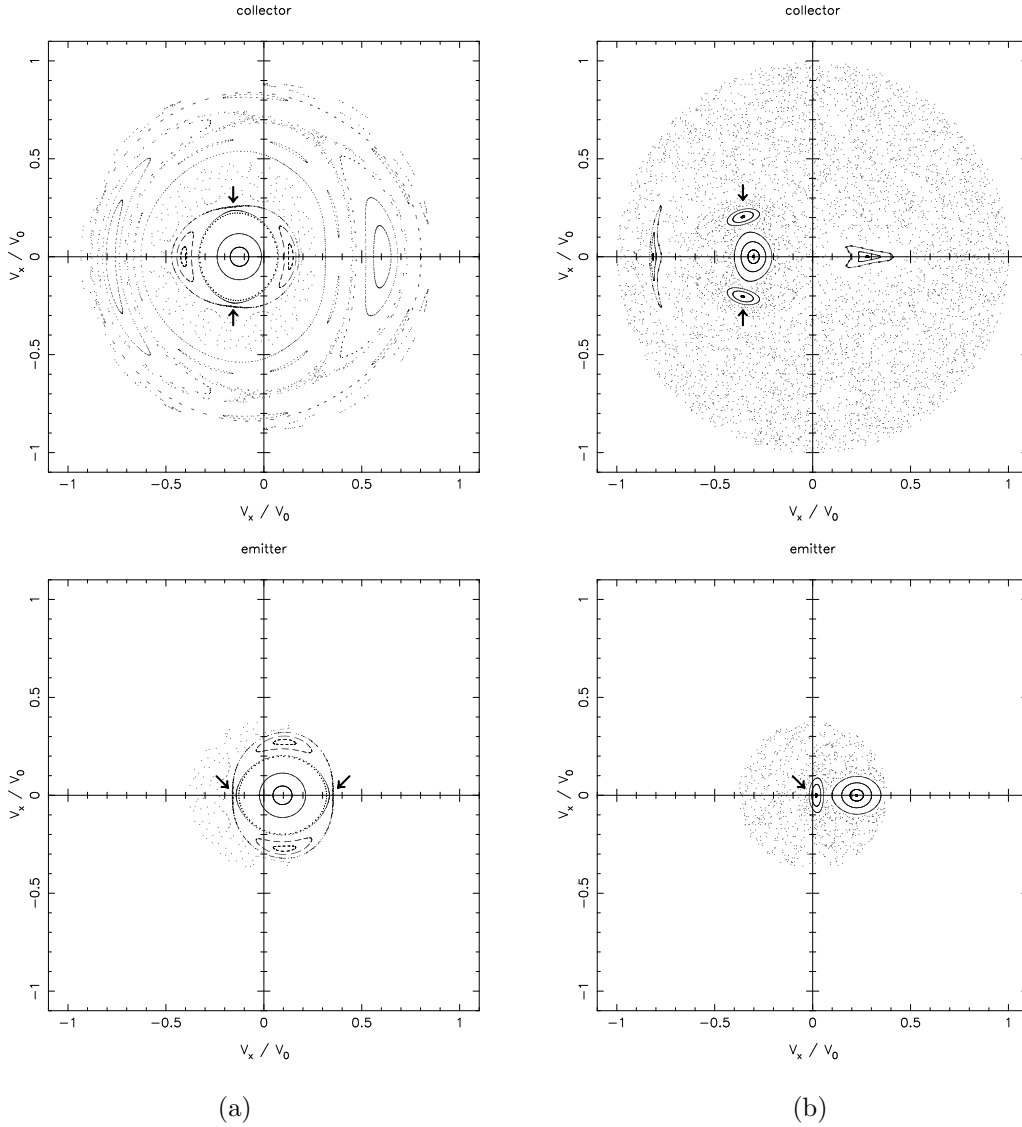


FIG. 25. Surfaces of section, showing the fixed points of $(2, 2)^-$, $(0, 2)^-$, $(2, 2)^+$ and $(1, 2)$ orbits for $\beta = 4.5$, $\gamma = 1.17$ and the tilt angle $\theta =$ (a) 11° , (b) 28° . The top and bottom panels correspond to the surfaces of section at the collector and the emitter barriers respectively. **a** : one can clearly see one big stable island of the period-1 orbit $(1, 1)^+$, and stable islands of the $(2, 2)^-$ and $(0, 2)^-$ orbits. The stable islands of the $(0, 2)^-$ orbit lie at the $\tilde{v}_x \equiv v_x/v_0$ axis at the periphery of the collector surface of section, they are absent at the emitter SOS. This $(2, 2)^-$ orbit produces two islands centered on the \tilde{v}_x axis at the collector barrier and two islands at the emitter barrier. To show the $(0, 2)^-$ and $(2, 2)^-$ orbits in a single bifurcation diagram it is therefore natural to represent these orbits by their values of the x component of the scaled velocity at the collector barrier. The fixed points of the generally unstable orbit $(2, 2)^+$ are not so easy to see by an (untrained) eye and pointed out by the arrows. Both fixed points of $(2, 2)^+$ have zero \tilde{v}_y at the emitter barrier and nonzero \tilde{v}_y at the collector barrier. Note, that at the collector barrier the $(2, 2)^+$ orbit has the same values of the x component of the scaled velocity (since $\tilde{v}_x \sim y$ and the $(2, 2)^+$ orbit strikes the collector wall at the same point). Therefore, this value is a convenient representation for the $(2, 2)^+$ orbits in the bifurcation diagrams. **b** : one can see a relatively large stable island of the $(1, 1)^+$ orbit, two islands of the Ω orbit (in collector barrier SOS only) and stable islands of the ν orbit (two islands at the collector barrier surface of section and one island at the emitter barrier SOS). Just as for the $(2, 2)^+$ and $(0, 2)^+$ orbits, the fixed points of the $(1, 2)$ orbits at the emitter wall have exactly the same values of \tilde{v}_x , which can therefore be used as their representation in the bifurcation diagrams. .

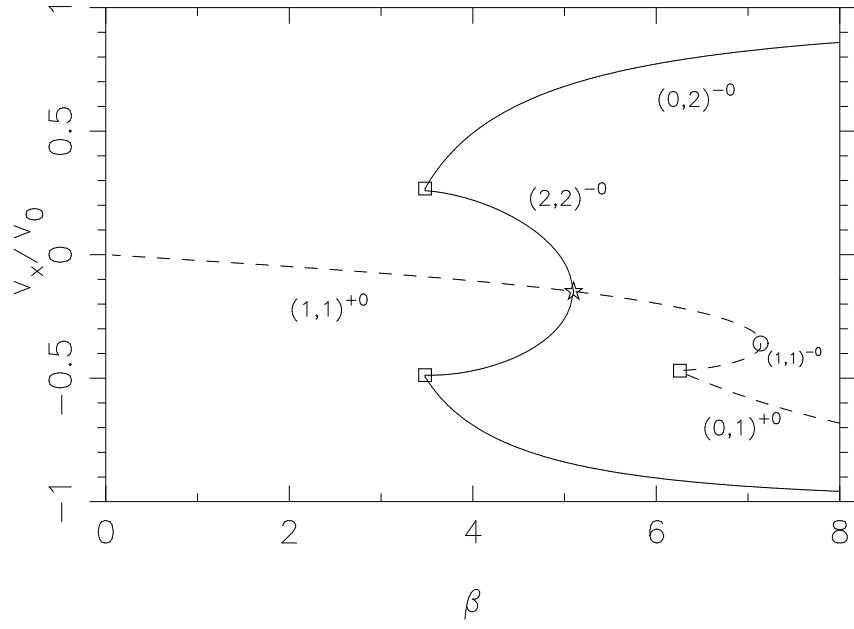


FIG. 26. The bifurcation diagram of the $(2,2)^-$ and $(0,2)^-$ orbits in the DBM. The vertical axis represents x component of the scaled velocity of the electron at the point of collision with the collector barrier (see also Fig. 25a). The tilt angle $\theta = 15^\circ$, and $\gamma = 1.17$.

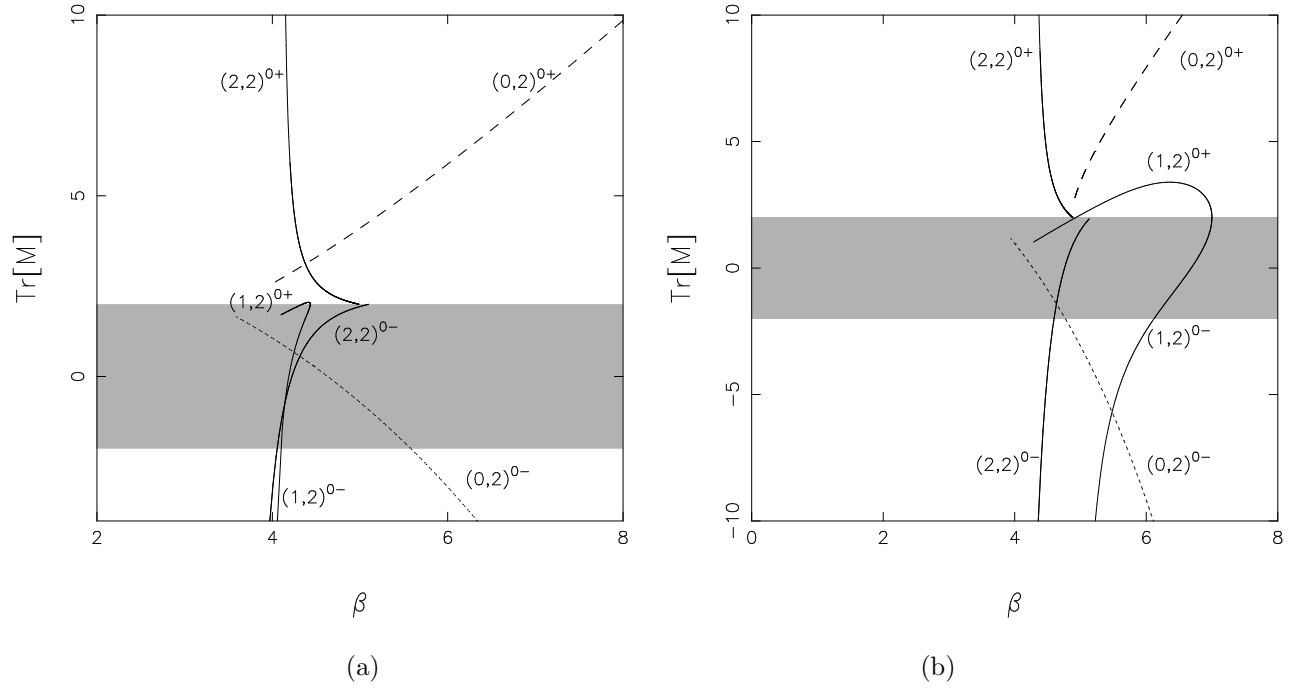


FIG. 27. The trace of monodromy matrix for different period-2 orbits of the first interval at (a) $\theta = 17^\circ$ and (b) $\theta = 28^\circ$.

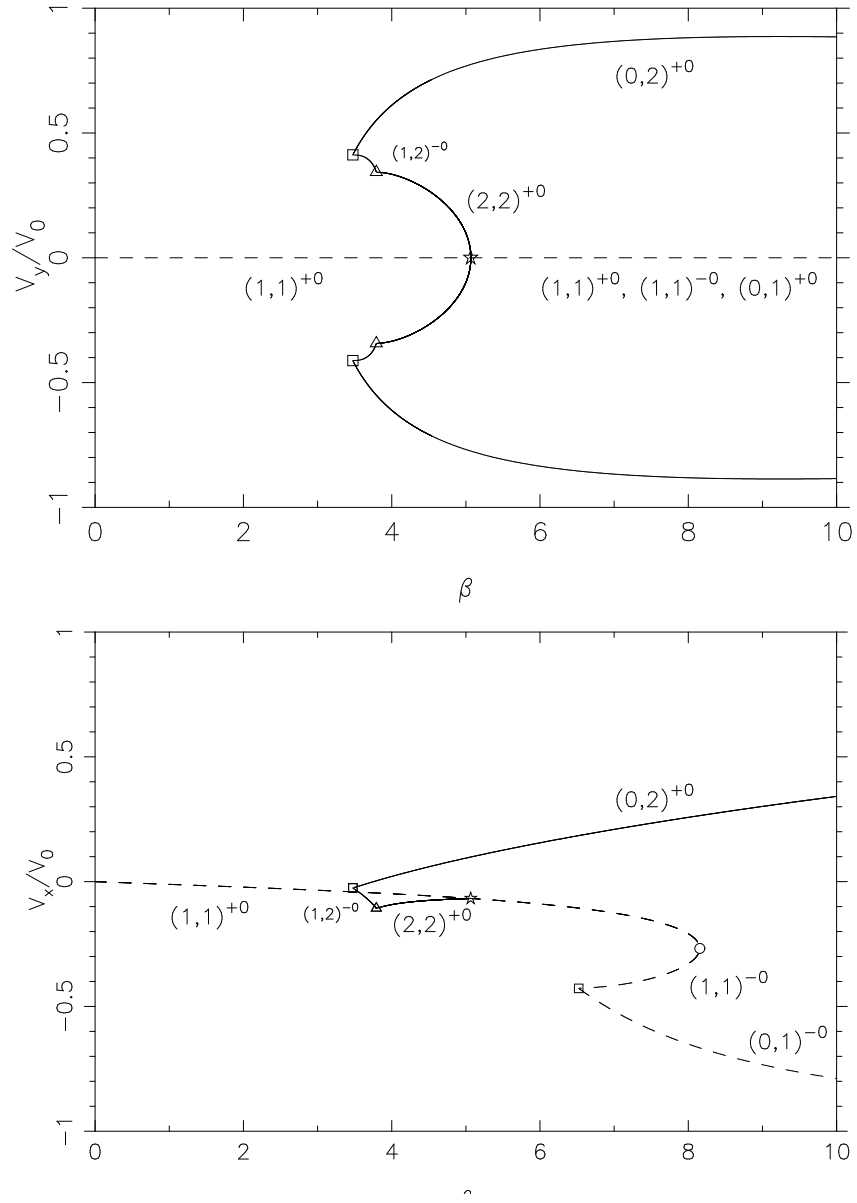
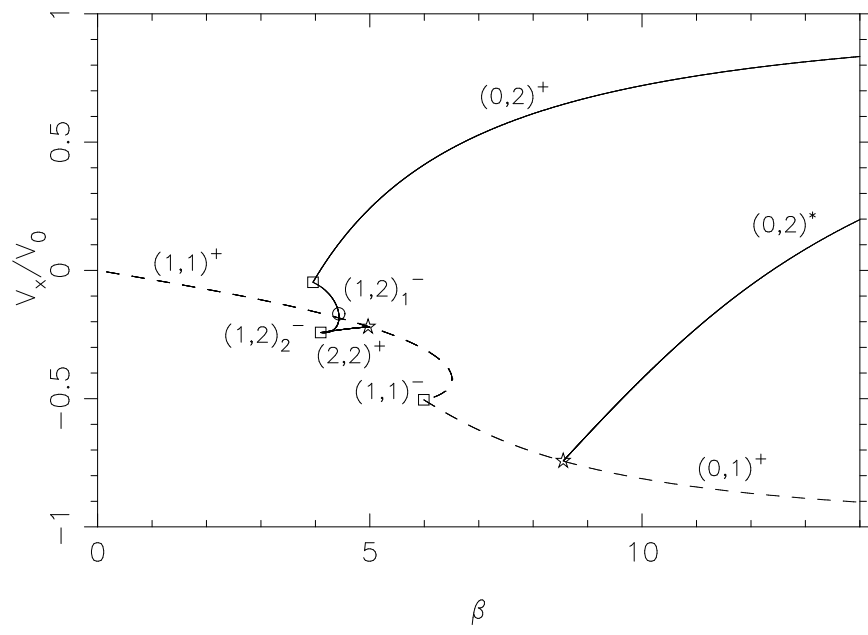
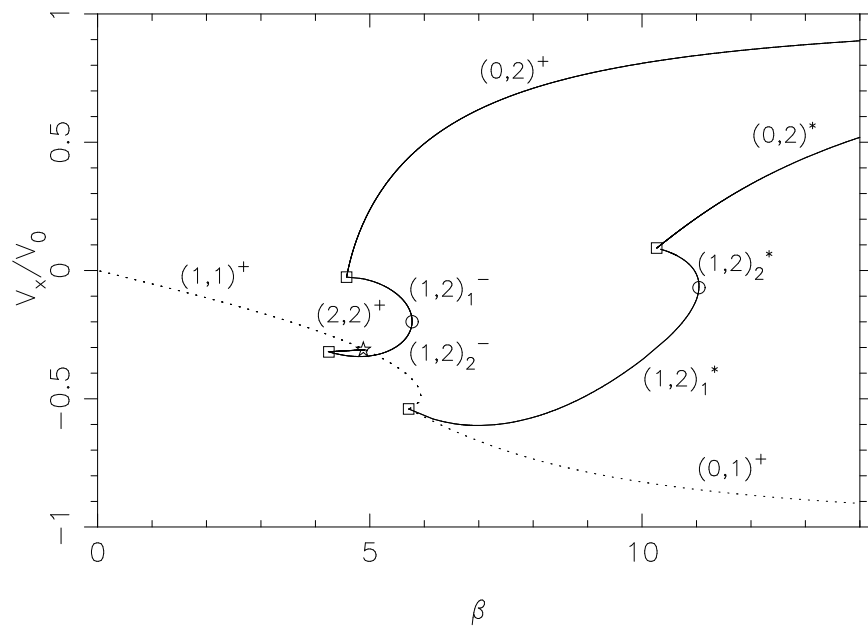


FIG. 28. The bifurcation diagram of the $(2,2)^+$, $(1,2)$ and $(0,2)^-$ orbits in the DBM in “regime one”. The vertical axis represents y (top panel) and x (bottom panels) components of the scaled velocity of the electron at the point of collision with the collector barrier (see Fig. 25b) ; $\gamma = 1.17$; the tilt angle $\theta = 5^\circ$.



(a)



(b)

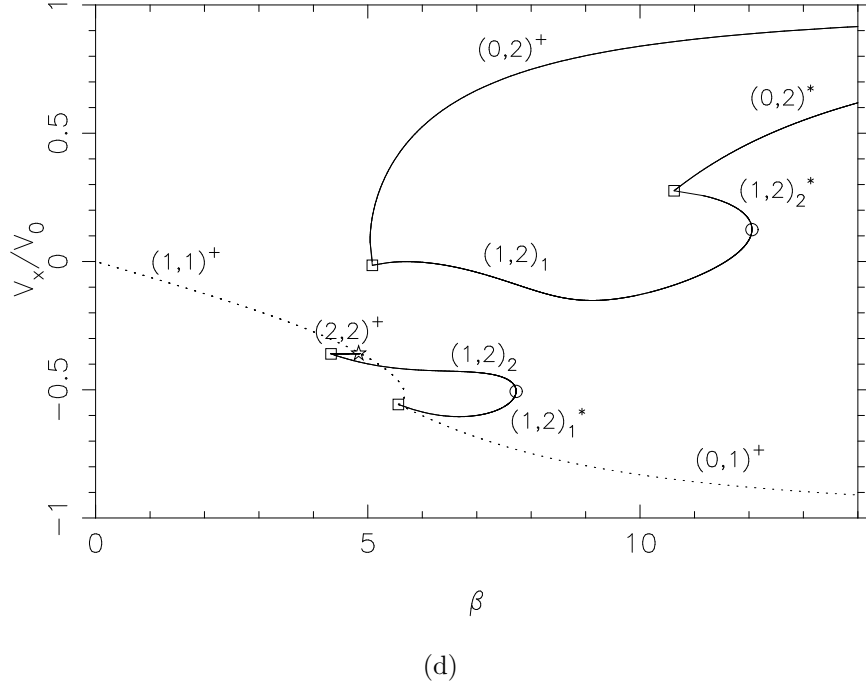
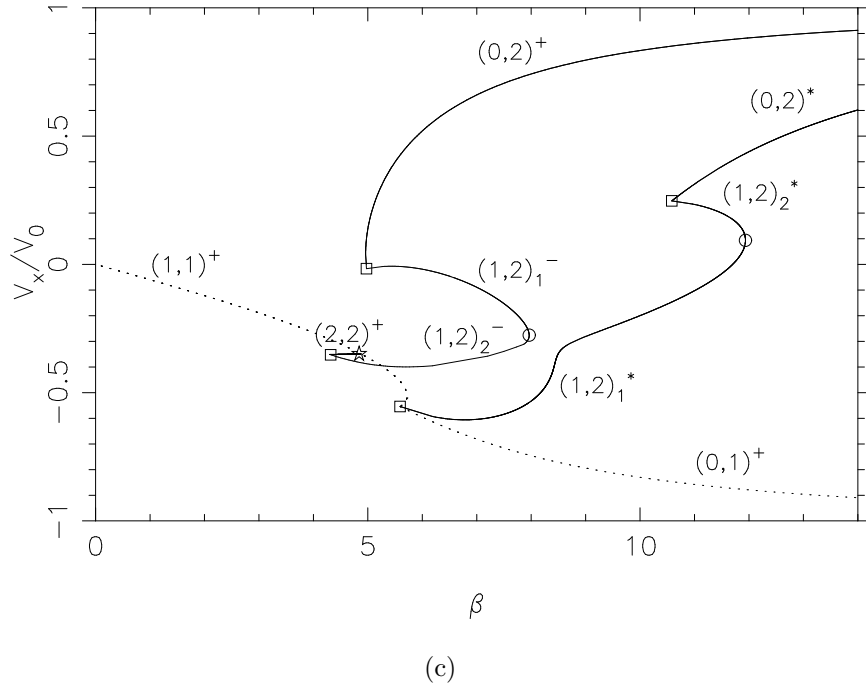
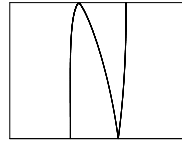
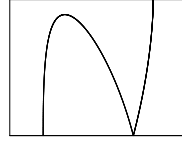


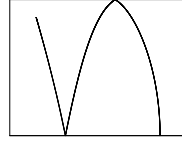
FIG. 29. The bifurcation diagram of the $(2,2)^+$, $(1,2)$ and $(0,2)^-$ orbits in the DBM in $(\beta, v_x/v_0)$ coordinates (see Fig. 25b) in regimes (a) two, (b),(c) three, and (c) four; $\gamma = 1.17$; the tilt angle $\theta =$ (a) 20° , (b) 27° , (c) 29° , and (d) 30° .



(a)



(b)



(c)

FIG. 30. Examples of the different types of period-3 orbits in the DBM, projected onto (y, z) planes : a $(3, 3)^-$ orbit (a), a $(1, 3)^+$ orbit (b), a $(2, 3)$ orbit (c).

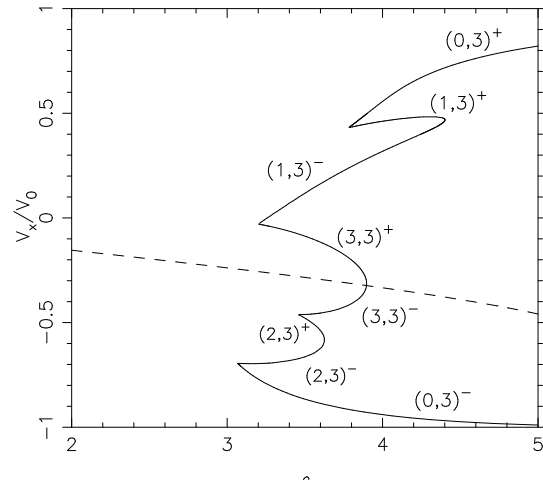
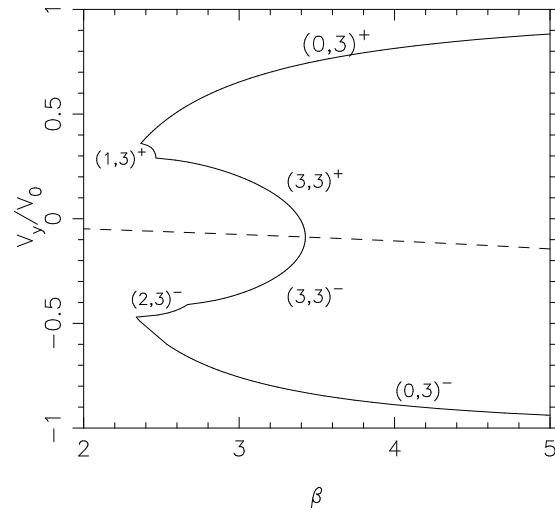


FIG. 31. The bifurcation diagrams of the period-3 orbits in the DBM, at $\gamma = 1.17$, $\theta =$ (a) 11° , (b) 38° .

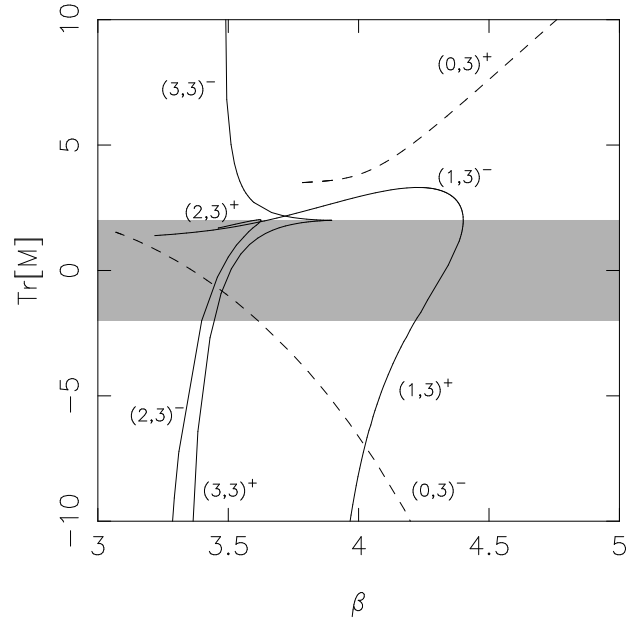


FIG. 32. The trace of monodromy matrix for different period-3 orbits related to the first 1 : 3 resonance of the traversing orbit $(1, 1)^{+(0)}$ at $\theta = 17^\circ$.

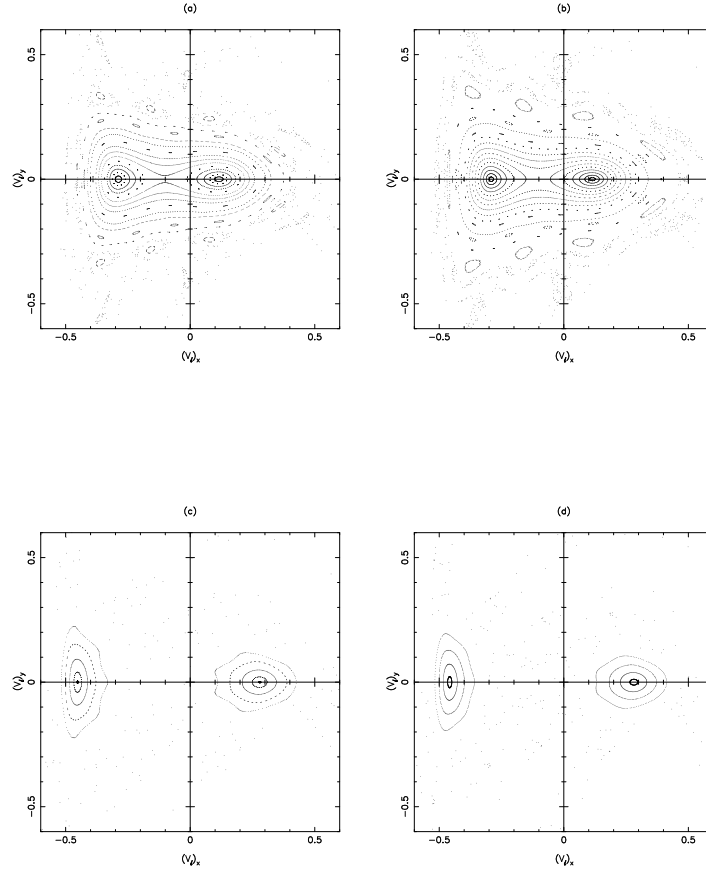


FIG. 33. Comparison of the SOS for the limiting mapping (B8) (b,d) with the ones of the exact Poincaré map (a,c). The tilt angle $\theta = 15^\circ$, $\beta_{\text{local}} = 0.2$ (a,b) and 0.5 (c,d). The SOS of the exact map is obtained for $k = 20$.

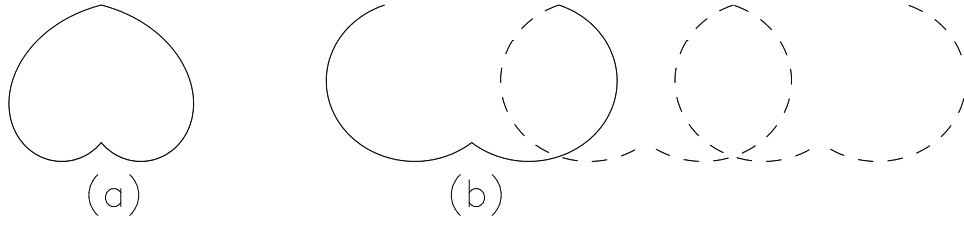


FIG. 34. A non-mixing two-bounce orbit, projected onto the (x', y') plane of the laboratory system of coordinates (a) and onto (x'', y'') plane of the "drifting" frame of reference.

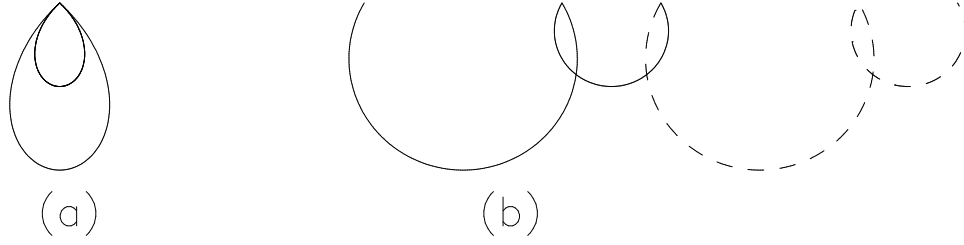


FIG. 35. A mixing self-retracing two-bounce orbit, projected onto the (x', y') plane of the laboratory system of coordinates (a) and onto (x'', y'') plane of the "drifting" frame of reference.